DIPLOMARBEIT

Entanglement-Based Quantum Communication over Long-Distance Free-Space Links

Ausgeführt am

Institut für Quantenoptik und Quanteninformation
Österreichische Akademie der Wissenschaften
Boltzmanngasse 3
1090 Wien

unter der Anleitung von O.Univ.Prof. Dr.phil. Anton Zeilinger

durch

Thomas Herbst

Preface

This diploma thesis was carried out at the Institute for Quantum Optics and Quantum Information (IQOQI) of the Austrian Academy of Sciences in Vienna. During my studies at the Vienna University of Technology I attended the seminars on quantum mechanics held at the IQOQI, which already sparked my interest in the groups working there. When I had to decide on the topic of my diploma thesis I took a closer look at the institute, especially the Free-Space group which immediately attracted my attention. After I have talked to the group members and Prof. Anton Zeilinger I got the opportunity to carry out my diploma thesis on "Entanglement-Based Quantum Communication over Long-Distance Free-Space Links".

The goal of my thesis was to support the optimization of a source for polarization-entangled photons, to design a precast and mobile free-space detection module for entanglement verification and to develop a software for easy and quick analysis of the measurement data.
The first chapter gives a short introduction to the motivation for free-space experiments, to entanglement-based quantum communication protocols and a review of previous entanglement-based free-space experiments.
In the second chapter the quantum channel and the detection concept of the 144km inter island free-space campaign between the Canary Islands La Palma and Tenerife is explained.
The third chapter describes the polarization-entangled photon source and its optimization, as well as the detection module.
Chapters four and five deal with the measurement, analysis and results of the 144km inter-island free-space experiment.
The last chapter provides a conclusions of the performed experiment and an outlook on upcoming free-space experiments.

Contents

1 Introduction

1.1 Motivation

Quantum communication [1] uses the laws of quantum physics to encode and decode information and hence provides much more efficient ways of communication than are classically possible. Additionally employing quantum entanglement offers access to a new domain of communication protocols, such as quantum dense coding, quantum teleportation or quantum key distribution (QKD). This makes it worthwhile to establish a global quantum communication network, aiming at the distribution and manipulation of quantum entanglement on a global scale.

At present, photonic schemes are the only suitable ones for long-distance quantum communication. Utilization of telecom fibers would seem a self-evident option, as there already exists a fully developed infrastructure almost all over the world. Yet the major problem with optical fibers is the maximal transmission distance, which is limited to the order of 100km [2; 3]. This problem could be overcome in principle by subdividing long distances in smaller ones and employing quantum repeaters [4] between these sections. However, the use of quantum repeaters does not seem to be implemented in the near future and therefore other transmission schemes are needed.

The most promising scenario is free-space quantum communication using satellites [5]. As the atmosphere's absorbtion coefficient is quite low in certain wavelength ranges, optical free-space links allow for larger link distances than possible with fibers. Moreover, the almost non-birefringent behavior of the atmosphere at optical wavelengths ensures for polarization preservation in contrast to optical fibers, where polarization rotation is another big issue. Link distances in terrestrial free-space schemes are limited due to the attenuation in the atmosphere which strongly depends on weather conditions and aerosols [6] and ultimately because of the Earth's curvature. Therefore it is inescapable to use satellites for further link expansion. The relocation of quantum communication to space would additionally allow for testing quantum mechanics over distances not achievable on the ground [7] and offer access to new applications such as quantum clock

synchronization, quantum positioning [8] and quantum astronomy [9].

Several feasibility studies show that current technology is capable of implementing satellite-based quantum communication [5; 10; 11]. A recently submitted proposal for a transceiver attached to the European Columbus module of the International Space Station (ISS) claims the implementation of a polarization-entangled photon source, a weak pulse decoy-state source and single-photon detection modules. The payload specified in reference [12] will then allow for QKD and entanglement verification over distances beyond 1000km and therefore overcome terrestrial dimensions by far. One of the three main satellite-based scenarios is the faint laser decoy-state QKD which was successfully tested in a long-distance free-space experiment between the Canary Islands of La Palma and Tenerife, Spain [13]. The second scenario applies a single-link entanglement-based QKD protocol and was also successfully tested on the Canary test link [14]. This thesis deals with the experimental emulation of the third scenario, where two entangled photons are transmitted to different receiver stations.

1.2 Entanglement-based Quantum Communication

1.2.1 The Qubit

The qubit is the quantum mechanical analog of the classical bit, which can be realized by any two-state quantum system. In contrast to the classical bit, which can carry either value "0" or "1", the states $|0\rangle$ and $|1\rangle$ of the qubit can exist in a superposition state

$$|\Psi\rangle = \alpha\,|0\rangle + \beta\,|1\rangle \;\text{ with } |\alpha|^2 + |\beta|^2 = 1. \tag{1.1}$$

This does not mean that the value of the qubit is somewhere between "0" or "1", but if one measures the qubit, the outcome of the measurement will be "0" with probability $|\alpha|^2$ and "1" with probability $|\beta|^2$.

For a better visualization the qubit can be represented on a unity sphere called Bloch sphere (see figure 1.1) in the form

$$|\Psi\rangle = \cos\left(\frac{\theta}{2}\right)|0\rangle + e^{i\Phi}\sin\left(\frac{\theta}{2}\right)|1\rangle\,, \tag{1.2}$$

with the azimuth and zenith angles Φ and θ respectively.

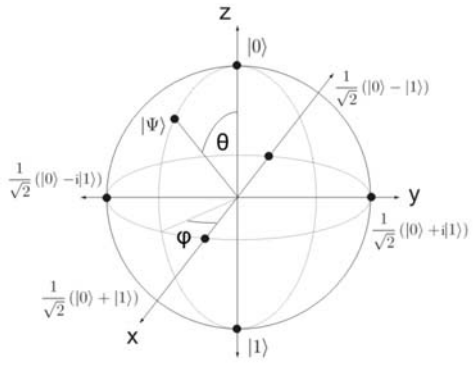

Figure 1.1: The representation of a general qubit (see equation 1.2) on the Bloch sphere.

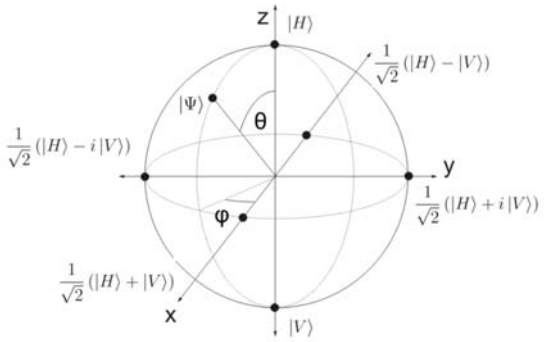

Figure 1.2: The representation of the polarization-encoded qubit (see equation 1.3) on the Poincaré sphere.

The Polarization-Encoded Qubit

As any two-state quantum system can serve as a qubit, the orthogonal polarization states $|H\rangle$ for horizontal and $|V\rangle$ for vertical polarization can build the basis for photonic qubits

$$|\Psi\rangle = \cos\left(\frac{\theta}{2}\right)|H\rangle + e^{i\Phi}\sin\left(\frac{\theta}{2}\right)|V\rangle\,. \tag{1.3}$$

This polarization-encoded qubit again can be represented on a unity sphere now called Poincaré sphere (see figure 1.2).

Entangled Qubits

In 1935 E. Schrödinger introduced the word *Verschränkung* [15] which was translated into the English word *Entanglement*. An entangled state is a superposition state of a composite two-qubit system of the form

$$|\Psi\rangle_{12} = \frac{1}{\sqrt{2}}(|H\rangle_1|V\rangle_2 + e^{i\phi}|V\rangle_1|H\rangle_2), \tag{1.4}$$

where the subscripts 1 and 2 denote the respective qubit and ϕ is the phase. Such a state has the interesting property that one cannot know in advance the outcome of the measurement on one qubit, but once one of the qubits is measured, the other one will immediately be determined with opposite outcome. As this is presumed to be true for arbitrary distances, it is called quantum non-locality.

Entanglement is a vital resource for new efficient communication protocols such as quantum dense coding, quantum teleportation or quantum key distribution. Especially the four maximally entangled Bell states

$$|\Psi^+\rangle_{12} = \frac{1}{\sqrt{2}}(|H\rangle_1|V\rangle_2 + |V\rangle_1|H\rangle_2) \tag{1.5}$$

$$|\Psi^-\rangle_{12} = \frac{1}{\sqrt{2}}(|H\rangle_1|V\rangle_2 - |V\rangle_1|H\rangle_2) \tag{1.6}$$

$$|\Phi^+\rangle_{12} = \frac{1}{\sqrt{2}}(|H\rangle_1|H\rangle_2 + |V\rangle_1|V\rangle_2) \tag{1.7}$$

$$|\Phi^-\rangle_{12} = \frac{1}{\sqrt{2}}(|H\rangle_1|H\rangle_2 - |V\rangle_1|V\rangle_2), \tag{1.8}$$

which form a complete orthogonal basis, play a key role in the following entanglement-based quantum-communication schemes. It has to be mentioned that sources of entangled pairs are also often called EPR-sources, related to A. Einstein, B. Podolsky and N. Rosen who published a paper in 1935 [16] where they presented a *Gedankenexperiment* on entangled particles.

1.2.2 Quantum-Key-Distribution Protocol

Quantum key distribution (QKD) is the most enhanced quantum communication protocol so far, due to the direct link to practical applications. The European Union (EU) for instance funds the SECOQC project aiming at the "Development of a Global Network for Secure Communication based on Quantum Cryptography". In this section the most common QKD protocols are presented. An overview over a broad range of schemes is found in the references [1; 17; 18]. It has to be mentioned that the main characters of all QKD schemes are Alice and Bob, who want to communicate secretly, and an eavesdropper called Eve.

BB84 protocol

In 1984 C. H. Bennett and G. Brassard presented the BB84 protocol [19] which is based on single photons encoded in the $|H/V\rangle$ and $|\pm 45°\rangle$ polarization bases. Alice prepares the photons completely random in one of the four states $|H\rangle$, $|V\rangle$, $|45°\rangle$, $|-45°\rangle$ and sends them to Bob. Bob randomly chooses the measurement basis for the transmitted photons and subsequently detects the photons in one of the two analyzer outputs. Later on Alice and Bob publicly communicate in which bases they prepared and measured each photon. If the same basis was chosen, then the outcome of Bob's measurement matches the state prepared by Alice thus contributing to the so called sifted key. This key is generated by assigning the logical bit values "0" to $|V\rangle$ and $|-45°\rangle$ and "1" to $|H\rangle$

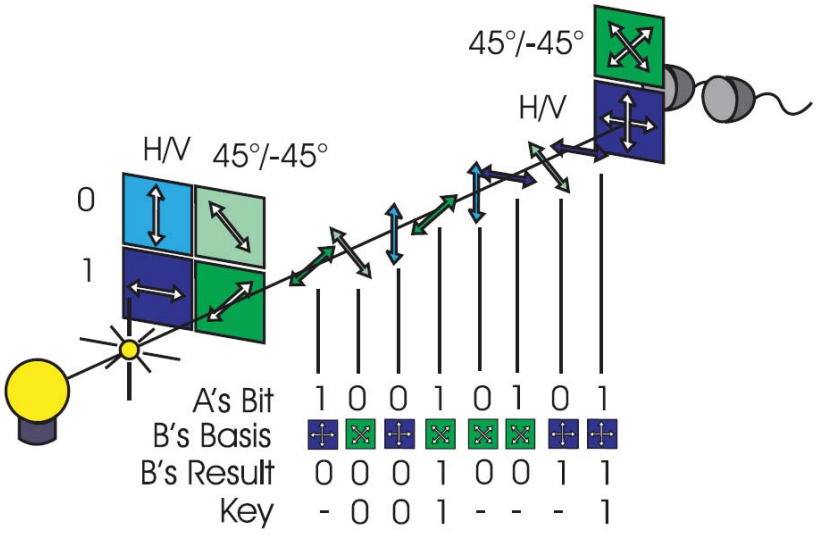

Figure 1.3: The scheme of the BB84 QKD protocol.

and $|45°\rangle$ (see figure 1.3). In principle, the no-cloning theorem [20] ensures the security of the protocol as every attack of an eavesdropper Eve would disturb the observed state and be recognized by Alice and Bob. Yet, imperfect single-photon sources such as faint lasers may send more than one photon per pulse and therefore open a backdoor for an eavesdropper. In this case a beam splitter would allow Eve to measure one photon of the pulse without disturbing the rest, hence without being revealed. Such a photon-number-splitting attack can be defeated with a decoy-state method proposed by W. Y. Hwang [21].

Modified BB84 protocol

The modified BB84 protocol is based on the distribution of polarization-entangled photons in the $|\Psi^-\rangle$ state to Alice and Bob. Both measure their photon intrinsically random in either the $|H/V\rangle$ or $|\pm 45°\rangle$ polarization basis. Publicly comparing the arrival times of the photons and the chosen measurement bases, allows Alice and Bob to extract the sifted key. In the case they measure a photon pair in the same basis, they know for sure that their results have to be completely anti correlated.

In the experiment reported by A. Poppe et al. [22] a secure quantum key was distributed between the headquarters of Bank-Austria Creditanstalt (Alice) and the Vienna City Hall (Bob). One photon of a polarization-entangled pair was sent to Bob and the other one measured locally. The intrinsically random choice of the measurement bases at Alice and Bob was realized with a 50/50 beam splitter either transmitting the photons in the $\pm 45°$ analyzer or reflecting them in the H/V analyzer (see figure 1.4).

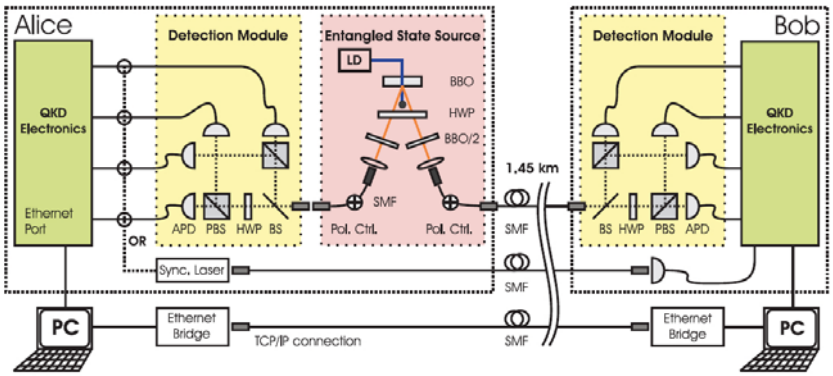

Figure 1.4: The scheme of the bank experiment in Vienna, Austria [22]. The entangled photon pairs were distributed between Alice (at the headquarters of Bank-Austria Creditanstalt) and Bob (at the Vienna City Hall).

Ekert protocol

The entanglement-based QKD scheme proposed by A. Ekert [23] in 1991 is similar to the modified BB84 protocol, yet the polarization directions in which Alice and Bob randomly analyze their photons are (0°,22.5°,45°) and (22.5°,45°,67.5°) respectively. In this scheme the outcomes of measurements in the same direction contribute to the secure key, whereas correlations in non-parallel measurement directions are used to calculate the S-value of the CHSH form [24] of Bell's inequality [25] (see chapter 2.2). As quantum mechanics violates this inequality, an eavesdropper would decrease the violation due to the introduced disturbance and be revealed.

Modified Ekert protocol

A modification of the Ekert protocol is based on Wigner's inequality [27] which needs only two randomly chosen analyzer settings (-30°,0°) and (0°,30°) for Alice and Bob respectively. Again, measurement outcomes in the same direction (i.e. both measure along the 0° axes) are used for the generation of the key, whereas the security check is performed with the non-parallel analyzer combinations. The violation of Wigner's inequality proves the absence of an eavesdropper as every interception attempt of Eve would disturb the entangled quantum state and decline the violation.
The modified Ekert protocol as well as the modified BB84 protocol were successfully implemented in the QKD experiment published by T. Jennewein et al. [26]. In this experiment the entangled photons were sent to Alice and Bob via 500m of optical fibers each, yet the distance between the receivers was 360m. Two electro-optic modulators set the random analyzer directions, and the orthogonal (bit 0) or parallel (bit 1) detection outcomes were stored together with the analyzer settings and time stamps for subsequent security checks and key sifting (see figure 1.5).

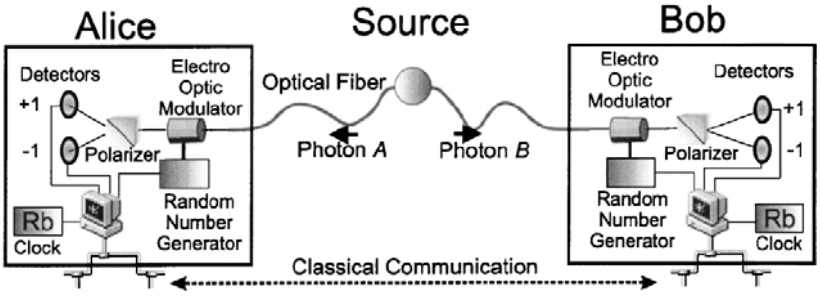

Figure 1.5: The scheme of the QKD experiment based on the modified Ekert and BB84 protocols [26]. The entangled photons were sent to Alice and Bob, who were separated by 360m.

1.2.3 Advanced Protocols

More advanced entanglement-based protocols such as quantum dense coding or quantum teleportation may be realized in future free-space experiments. Both schemes are based on two-photon interference in a Bell state analyzer which is why we performed a preliminary test of the feasibility of two-photon interference over a long-distance free-space link (see chapter 6).

Quantum Dense Coding

Quantum dense coding is a protocol to transmit two bits of information by the manipulation of only one photon of an entangled pair, thus manipulation of only one bit of information. Hence the term "dense coding" phrases the increased capacity of the quantum-communication channel.

C. H. Bennett and S. J. Wiesner [28] theoretically proposed this scheme, which is based on two entangled two-state systems, i.e. the horizontal $|H\rangle$ and vertical $|V\rangle$ polarization state of a photon in our case. The four classical combinations of the polarization states for photon pairs are HH, HV, VH and VV, which can be used to encode 2 bits of information under manipulation of both photons.

In contrast, quantum mechanics and its inherent superposition principle allows us to switch to another basis, the four maximally entangled Bell states $|\Psi^+\rangle, |\Psi^-\rangle, |\Phi^+\rangle$ and $|\Phi^-\rangle$ (see equations 1.5 - 1.8). These four states again form an ensemble capable of carrying 2 bits of information with the difference that now it is sufficient to manipulate only one photon, thus one bit of information, to set any of the four encoding states.

Suppose a polarization-entangled photon source distributes entangled photon pairs in the $|\Psi^+\rangle$ state to Alice and Bob. Bob can perform four different unitary transformations on his photon by the use of a half-wave ($\lambda/2$) and a quarter-wave ($\lambda/4$) plate:

1. Identity operation $|\Psi^+\rangle \rightarrow |\Psi^+\rangle$ $(\theta_{\frac{\lambda}{2}} = 0,\ \theta_{\frac{\lambda}{4}} = 0)$
2. Polarization rotation $|\Psi^+\rangle \rightarrow |\Phi^+\rangle$ $(\theta_{\frac{\lambda}{2}} = \frac{\pi}{4},\ \theta_{\frac{\lambda}{4}} = 0)$
3. Polarization-dependent phase shift $|\Psi^+\rangle \rightarrow |\Psi^-\rangle$ $(\theta_{\frac{\lambda}{2}} = 0,\ \theta_{\frac{\lambda}{4}} = \frac{\pi}{2})$
4. Rotation and phase shift together $|\Psi^+\rangle \rightarrow |\Phi^-\rangle$ $(\theta_{\frac{\lambda}{2}} = \frac{\pi}{4},\ \theta_{\frac{\lambda}{4}} = \frac{\pi}{2})$

So he is able to set any of the four Bell states by the manipulation of only one photon, thus encode 2 bits of information by the manipulation of only one bit. Alice subsequently

State from Bob	Alice's coincidences
$\|\Psi^+\rangle$	coinc. between D_H and D_V or $D_{H'}$ and $D_{V'}$
$\|\Psi^-\rangle$	coinc. between D_H and $D_{V'}$ or $D_{H'}$ and D_V
$\|\Phi^+\rangle$	2 photons in either D_H, D_V, $D_{H'}$ or $D_{V'}$
$\|\Phi^-\rangle$	2 photons in either D_H, D_V, $D_{H'}$ or $D_{V'}$

Table 1.1: The coincidence combinations in Alice's Bell-state analyzer for the different states from Bob. Alice can not distinguish between $|\Phi^+\rangle$ and $|\Phi^-\rangle$ because both photons end up in the same detector.

measures the state from Bob with a Bell-state analyzer and reads the encoded information.

The experimental realization of the quantum dense-coding protocol was reported by K. Mattle et al. [29] with the setup shown in figure 1.6. Due to coincidence detection (i.e. the registration of simultaneous detector "clicks"), Alice can distinguish between $|\Psi^+\rangle$, $|\Psi^-\rangle$ and the $|\Phi^\pm\rangle$ states but not between $|\Phi^+\rangle$ and $|\Phi^-\rangle$ (see table 1.1). Therefore three different outcomes can be distinguished which enables one to encode the desired message in trits. In the experiment, the ASCII codes 75, 77 and 179 for "KM°" were sent in only 15 trits (see figure 1.7), whereas the classical analog would require 24 bits.

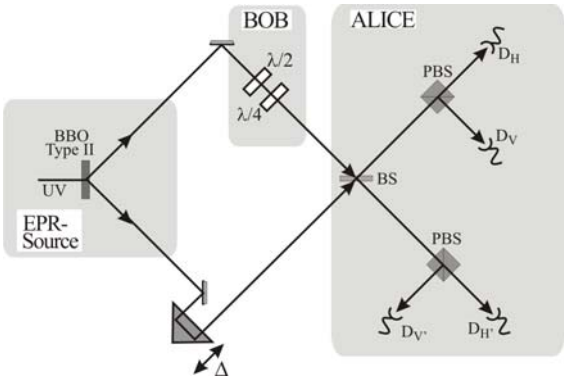

Figure 1.6: The experimental setup for quantum dense coding [29].

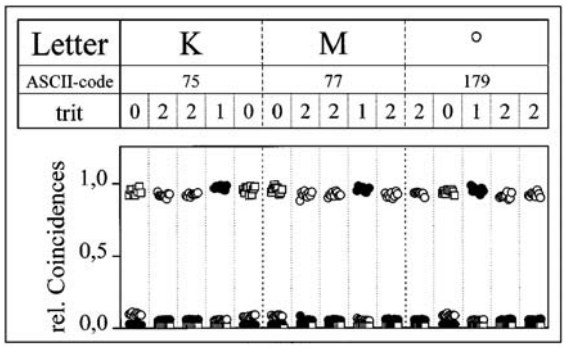

Figure 1.7: The ASCII codes 75, 77 and 179 for "KM°" were encoded in 15 trits with "0" $\equiv |\Phi^-\rangle \mathrel{\widehat{=}} \square$, "1" $\equiv |\Psi^+\rangle \mathrel{\widehat{=}} \bullet$ and "2" $\equiv |\Psi^-\rangle \mathrel{\widehat{=}} \circ$ [29].

Quantum Teleportation

The quantum teleportation protocoll proposed by C. H. Bennett et al. [30] offers the possibility to transfer the state of one qubit onto another qubit of an entangled pair (see figure 1.8). At the same time the original state is destroyed thus obeying the no-cloning theorem [20], which says that it is impossible to make an exact copy of a qubit without disturbing the original one.

Let us assume we want to teleport a polarization-encoded qubit 1

$$|\Psi\rangle_1 = \alpha\,|H\rangle_1 + \beta\,|V\rangle_1 \;\text{ with } |\alpha|^2 + |\beta|^2 = 1. \tag{1.9}$$

To do so we need an ancillary pair of entangled qubits 2 and 3 prepared in the Bell state

$$\left|\Psi^-\right\rangle_{23} = \frac{1}{\sqrt{2}}(|H\rangle_2\,|V\rangle_3 - |V\rangle_2\,|H\rangle_3). \tag{1.10}$$

The joint quantum state of all three qubits can be expressed in the basis of the four maximally entangled Bell states (see equations 1.5 - 1.8)

$$\begin{aligned}|\Psi\rangle_{123} = |\Psi\rangle_1 \otimes \left|\Psi^-\right\rangle_{23} = \frac{1}{2}[&\left|\Psi^-\right\rangle_{12}(-\alpha\,|H\rangle_3 - \beta\,|V\rangle_3)\\ &+\left|\Psi^+\right\rangle_{12}(-\alpha\,|H\rangle_3 + \beta\,|V\rangle_3)\\ &+\left|\Phi^-\right\rangle_{12}(+\alpha\,|V\rangle_3 + \beta\,|H\rangle_3)\\ &+\left|\Phi^+\right\rangle_{12}(+\alpha\,|V\rangle_3 - \beta\,|H\rangle_3)].\end{aligned} \tag{1.11}$$

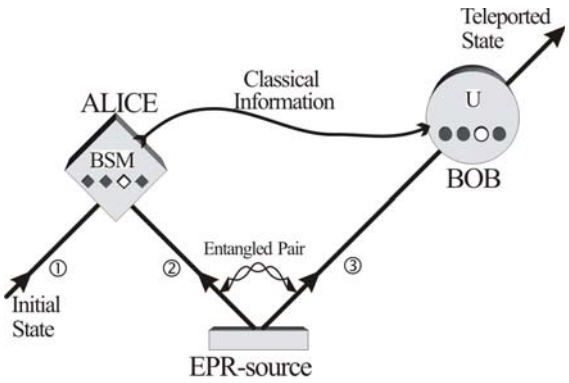

Figure 1.8: The quantum teleportation scheme [31].

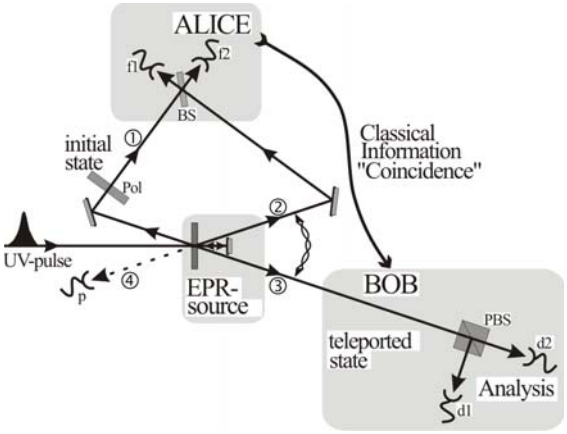

Figure 1.9: The setup of the quantum teleportation experiment in reference [31].

Therefore projecting qubits 1 and 2 onto one of the four Bell states, i.e. Alice performs a Bell-state measurement on them, will force Bob's third qubit in a state with a specific relation to the original state of qubit 1. Only if Alice's outcome is the $|\Psi^-\rangle_{12}$ state, Bob has a replica of the initial state with an irrelevant overall phase factor. In all other cases, Bob has to perform a specific unitary transformation on his state depending on the outcome of Alice's measurement. As every Bell state is measured with equal probability of $\frac{1}{4}$, the experiment reported by D. Bouwmeester et al. [31] only achieved exact teleportation in one quater of the cases, because Alice's analyzer just looked for a $|\Psi^-\rangle_{12}$ state (see figure 1.9 and compare with table 1.1 and the Bell-state analyzer in figure 1.6).

A more recent experiment was performed by R. Ursin et al. [32], where Alice was able to distinguish between a $|\Psi^-\rangle_{12}$ and a $|\Psi^+\rangle_{12}$ state. Alice's measurement outcome was actively fed forward to Bob which introduced a polarization dependent π-phase shift on his photon if Alice reported a $|\Psi^+\rangle_{12}$ state and otherwise did nothing (see figure 1.10).

Another interesting feature is the so called entanglement swapping [33], which is depicted in figure 1.11. If for instance qubit 1 itself is entangled with lets say qubit 4, then a Bell-state measurement on the qubits 1 and 2 will swap the entanglement onto qubits 3 and 4.

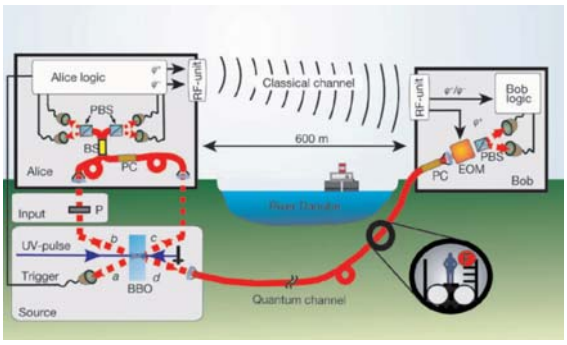

Figure 1.10: The setup of the quantum teleportation experiment across the Danube in Vienna, Austria [32].

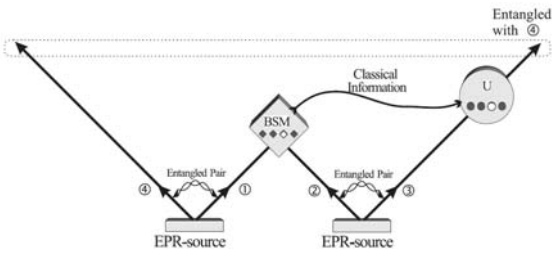

Figure 1.11: The entanglement swapping scheme [1].

1.3 Review of Entanglement-Based Free-Space Experiments

In the field of free-space quantum communication various groups have overcome distances from several kilometers [34–39] up to 144km [13] performing single-photon QKD with faint laser pulses.

The first free-space distribution of entangled photons was reported in 2003 by M. Aspelmeyer et al. [40] over a 600m "long-distance" free-space link. Two independent receiver stations were separated by 600m on the rooftops of two buildings at different sides of the Danube in Vienna, Austria, with no direct line of sight between them (see figure 1.12). The receiver stations called Alice and Bob were located approximately 500m and 150m apart from the entangled photon source respectively. A polarization-entangled photon source at the transmitter station produced ∼120,000 single photons per s in each arm and 20,000 polarization-entangled photon pairs per s in the $|\psi^-\rangle$ state. Alice and Bob measured ∼4000 singles per s and 15 coincidences per s resulting in a CHSH S-value of $S^{\mathrm{Exp}} = 2.41 \pm 0.10$ and a violation of the CHSH inequality by 4.1 standard deviations.

Entanglement-based BB84 QKD over a 1.5km free-space link was published by I. Marcikic et al. [41] of the National University of Singapore. Alice and Bob were situated on the rooftops of two buildings separated by 1.5km in the campus of the university. In contrast to the previous experiment, the polarization-entangled photon source and Alice

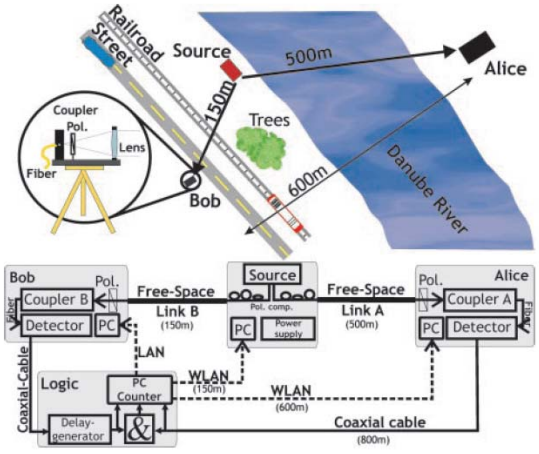

Figure 1.12: The scheme of the 600m free-space experiment in Vienna, Austria [40].

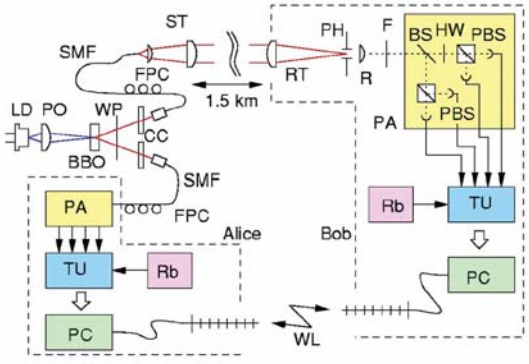

Figure 1.13: The scheme of the 1.5km free-space QKD experiment in Singapore [41].

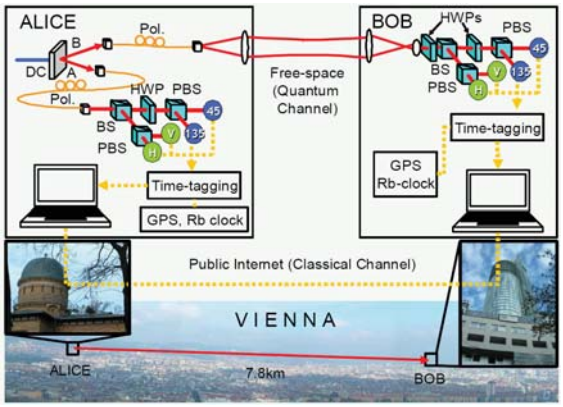

Figure 1.14: The scheme of the 7.8km free-space experiment in Vienna, Austria [42].

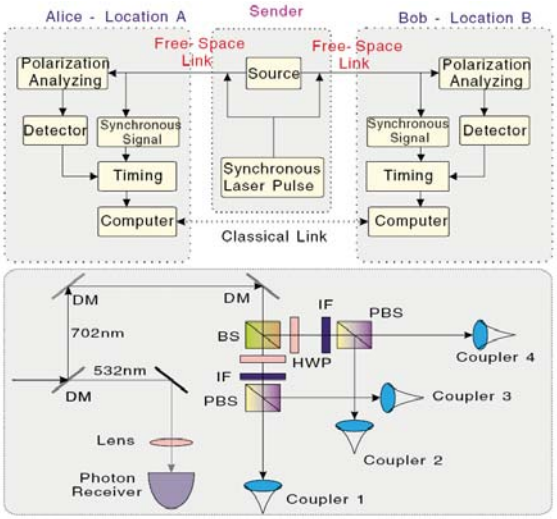

Figure 1.15: The scheme of the 13km free-space experiment in Hefei, China [43].

were located at the same place and only one photon of an entangled pair was sent to Bob (see figure 1.13). On average they generated a secure key of 630 bits per s during an uninterrupted 10h long-time measurement.

A similar scheme was performed by K.J. Resch et al. [42] one year earlier over a 7.8km link. The source and Alice were placed inside the Kuffner Sternwarte observatory and Bob was situated on the 46th story of the Millennium Tower, 7.8km apart (see figure 1.14). This was the first time that the horizontal link distance exceeded the vertical equivalent for shining through the whole atmosphere, thus an encouraging result for future satellite-based quantum communication. The observed S-value of $S^{\mathrm{Exp}} = 2.27 \pm 0.019$ violated the CHSH inequality by 14 standard deviations.

In the experiment reported by C.Z. Peng et al. [43] a further step was made by sending both photons of an entangled pair to two receivers separated by 10.5km and with no direct line of sight between each other. Alice and Bob were located on the west campus of the University of Science and Technology of China and Feixi in Hefei, China, respectively. The polarization-entangled photon source was situated on the summit of Dashu Mountain 7.7km away from Alice and 5.3km away from Bob. Whereas all other experiments so far labeled each detector count with a time stamp and performed cross correlation to find coincidences, this group used the method of laser pulse synchronization with a Q-switched 532nm laser (see figure 1.15). They observed an S-Value of $S^{\mathrm{Exp}} = 2.45 \pm 0.09$ and therefore violated the CHSH inequality by 5 standard deviations.

In an additional entanglement-based BB84 QKD experiment they retrieved an average secure-key distribution of 10 bits per s.

In 2007 the so far longest distance for entanglement-based free-space QKD was reported by R. Ursin et al. [14]. The 144km inter-island experiment was conducted between the Canary Islands La Palma and Tenerife at an elevation of 2400m above sea level. On the island of La Palma the polarization-entangled photon source and Alice as well as the transmitter telescope were located. With the European Space Agency's (ESA's) Optical Ground Station (OGS) acting as the receiver on Tenerife, this was the first reported implementation of space hardware to a free-space quantum-communication experiment so far (see figure 1.16). To reduce the link attenuation, an unidirectional closed-loop tracking system automatically controlled the pointing direction of the transmitter telescope. The polarization-entangled photon source yielded locally observed single-photon count rates of 10^6 per s in each output mode and 145,000 pairs per s, thus meeting the coincidence production rate required for space experiments for the first time. The obtained S-value $S^{\mathrm{Exp}} = 2.508 \pm 0.037$ violated the CHSH inequality by more than 13

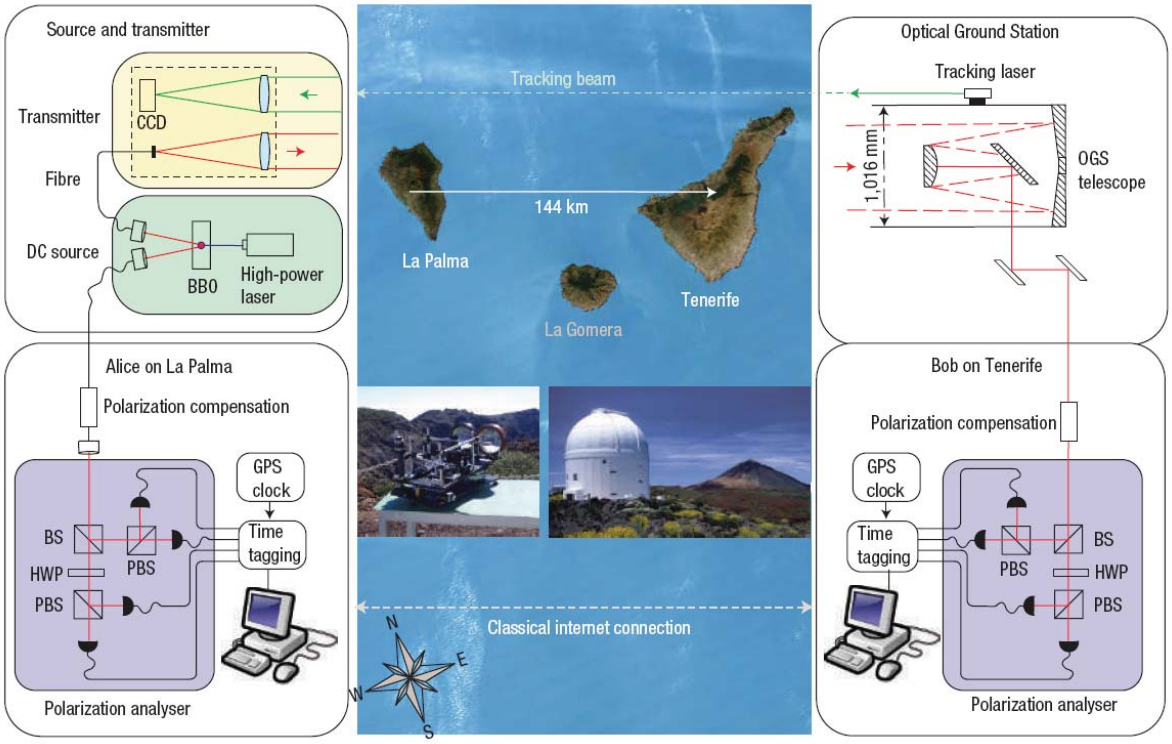

Figure 1.16: The scheme of the 144km free-space QKD experiment between the Canary Islands La Palma and Tenerife, Spain [14].

standard deviations and entanglement-based BB84 QKD resulted in a secure key of 2.37 bits per s.

The above mentioned 144km inter-island experiment paved the way for a subsequent experiment presented in this thesis. In contrast, a new highly efficient and very compact source enabled us to send both photons of an entangled pair over the 144km quantum channel, which now was actively locked by a bidirectional closed-loop tracking system.

2 The 144km Free-Space Bell-State Experiment

In the long-distance free-space experiment between the Canary islands La Palma and Tenerife, we successfully transmitted entangled photonic Bell states over a 144km free-space link with a link attenuation of 71.2dB. We violated the CHSH inequality [24] by more than 5 standard deviations σ and therefore verified the presence of entanglement between the photon pairs. In contrast to previous experiments, where only one photon of an entangled pair was sent to Tenerife and the partner photon was measured locally at La Palma [14], we showed that entangled photons endure a high loss transmission through 144km of turbulent atmosphere. Furthermore, with a flight time of $\sim$0.5ms, we report the longest lifetime of entangled photon states measured so far.

As the receiver telescope on Tenerife was originally built for laser communication with satellites, we utilized space equipment that meets the technical requirements for a low

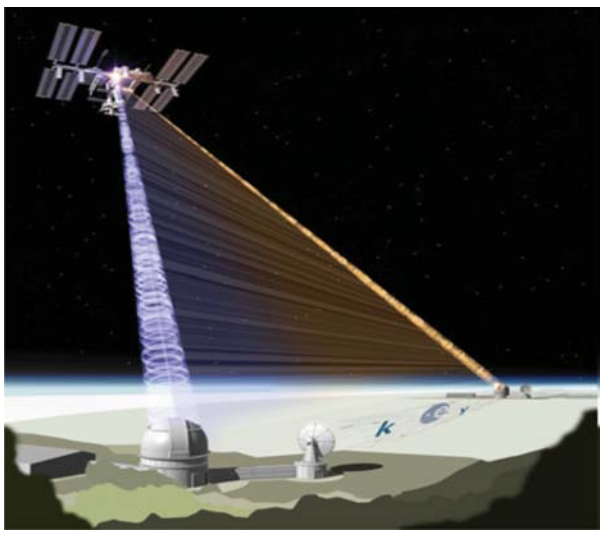

Figure 2.1: Outline of the proposed entangled-photon satellite-earth link. The project named Space-QUEST (QUantum Entanglement for Space experimenTs) is currently pursued together with the European Space Agency (ESA).

earth orbit (LEO) satellite down link. The successful transmission of both entangled photons showed the feasibility of a two link satellite-to-ground system (see figure 2.1) which may in future allow for quantum communication on a global scale.

2.1 Quantum Channel

The quantum-communication channel for the entangled photonic Bell states was established between a self designed refractor telescope on La Palma and the European Space Agency's (ESA's) Optical Ground Station (OGS) [44] on Tenerife.

2.1.1 Transmitter

On the island of La Palma, the Observatorio del Roque de los Muchachos is situated on the edge of the Caldera de Taburiente National Park. This site is located ∼2400m

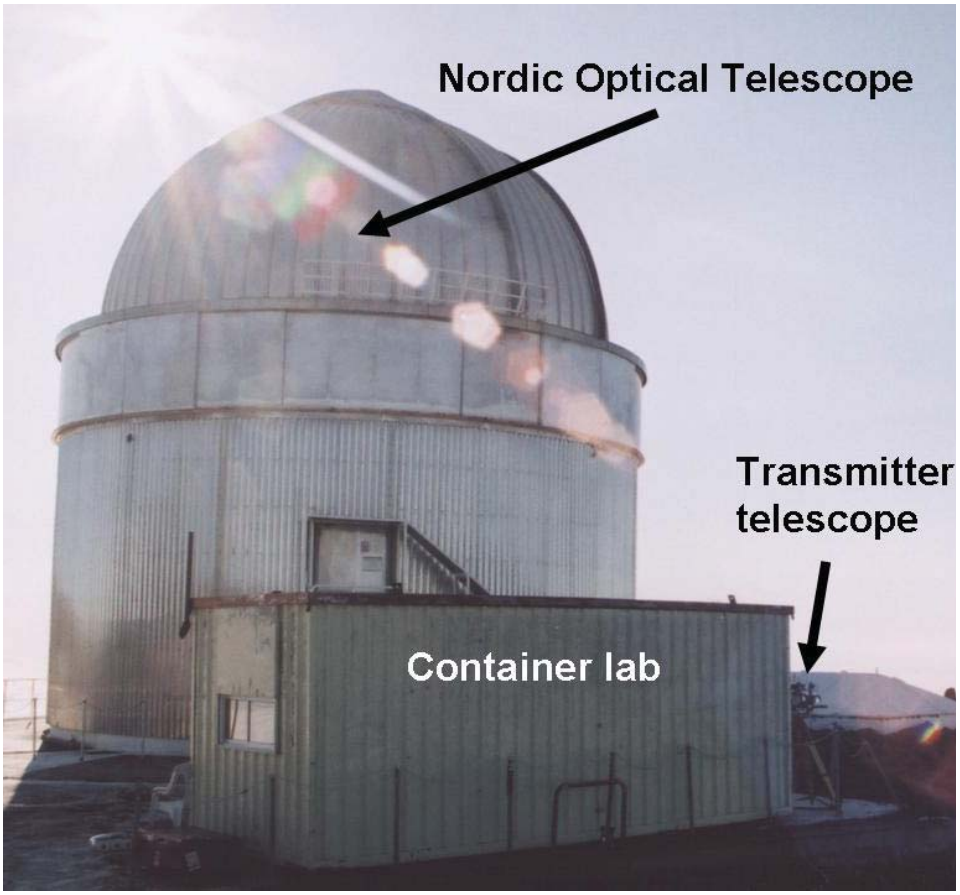

Figure 2.2: The container lab and transmitter telescope next to the Nordic Optical Telescope (NOT).

above sea level in the municipality of Garafía. It is home to the Nordic Optical Telescope (NOT) [45] amongst an extensive fleet of telescopes. Our transmitter telescope and a small container lab for the scientists and the equipment (see figure 2.2) was placed at the parking lot next to the NOT (Coordinates: 28°45'N 17°53'W 2382m).

Entangled Photon Source

With the optimized Sagnac source for polarization-entangled photons as described in chapter 3.1, we had a very compact and highly efficient cw-pumped source (see figure 2.3) in contrast to previous experiments [14] where a large and bulky picosecond-pulsed Nd:vanadate laser was used.

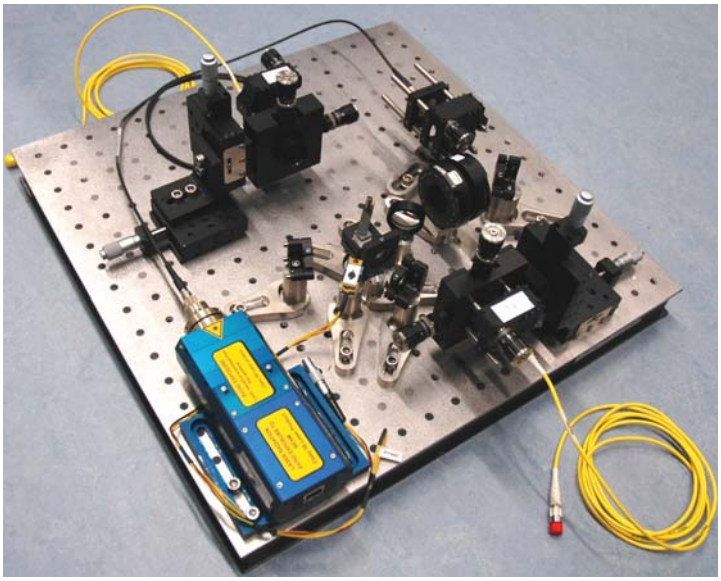

Figure 2.3: The experimental Sagnac setup to produce polarization-entangled photons.

In our source a 10mm long PPKTP crystal pumped by a 405nm laser diode produced maximally entangled photon pairs of 810nm wavelength and a bandwidth (FWHM) of 0.6nm. By changing the phase Φ in the state

$$|\Psi\rangle = \frac{1}{\sqrt{2}}(|HV\rangle + e^{i\Phi}\,|VH\rangle) \tag{2.1}$$

with a HWP and a QWP in the 405nm pump beam, we were able to switch between the Bell states

$$\left|\Psi^{+}\right\rangle = \frac{1}{\sqrt{2}}(|HV\rangle + |VH\rangle) \text{ and } \left|\Psi^{-}\right\rangle = \frac{1}{\sqrt{2}}(|HV\rangle - |VH\rangle). \tag{2.2}$$

About 10^6 photon pairs/s and $\sim 3.3 \times 10^6$ single photons/s of $\sim 10^7$ generated photon pairs/s were locally detected at a laser pump power of 20mW. The entangled photons were coupled into single-mode fibers and a 10m fiber delay line was introduced between the two output modes (see figure 2.4) so that the entangled photons traveled 10m one after the other and for better detection analysis. With a group velocity of $\sim \frac{2}{3}c$ in the fiber, this resulted in a time delay $\Delta t \approx 50$ns and thus in coincidence peaks ± 50ns around zero delay in the measured coincidence histograms. Manual polarization controllers (PCO)

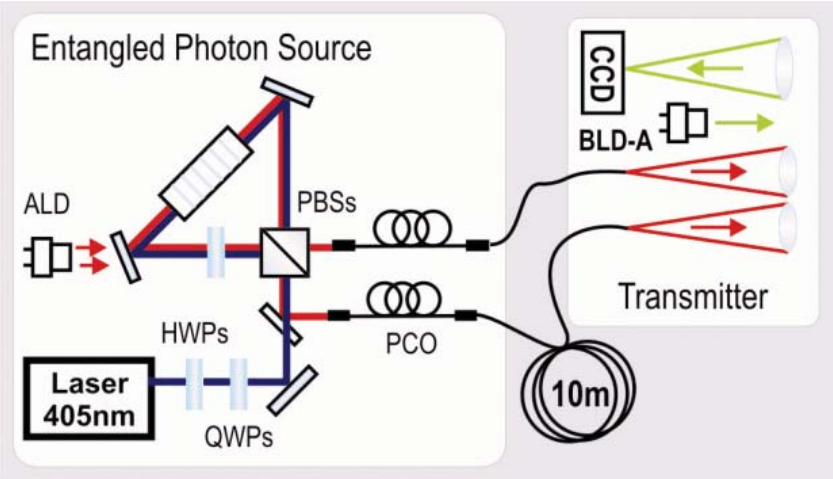

Figure 2.4: The experimental scheme of the transmitter on La Palma. Entangled photons generated by a Sagnac SPDC source (see chapter 3.1) were coupled into single-mode fibers equipped with manual polarization controllers (POC) for polarization compensation by the aid of an auxiliary laser diode (ALD). A 10m delay line was introduced in one output arm before both were connected to a pair of telescopes sending the photons through 144km of turbulent atmosphere to the receiver on Tenerife. A 532nm beacon laser diode (BLD-A) and the tracking CCD were used for bidirectional closed-loop tracking.

in each fiber were used for polarization compensation to establish a common polarization reference frame between the transmitter and receiver before the measurement was started.

Transmitter Telescope

The single-mode fibers from the source were connected to fiber adapters mounted on motor-controlled translation stages attached to a rotatable and tiltable telescope platform (see figure 2.5). Two *Lens-Optics* [1] f/4 achromatic best-form lenses with a focal

[1] LENS-Optics GmbH, Bürgermeister-Neumeyr-Straße 7, 85391 Allershausen, Deutschland; www.lens-optics.de

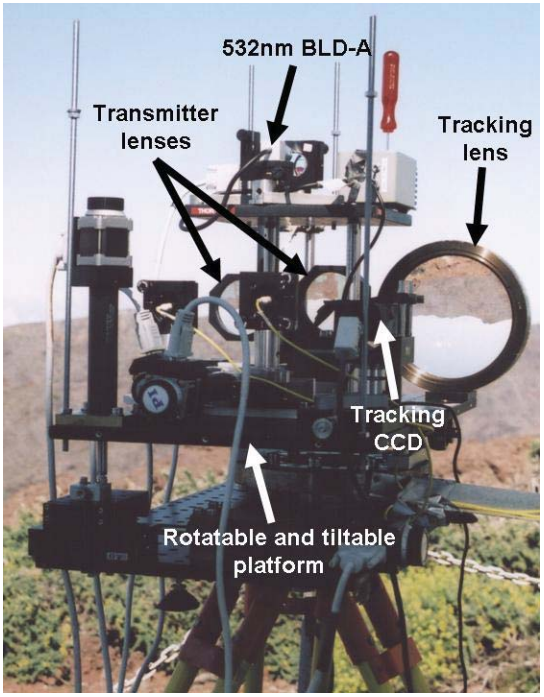

Figure 2.5: The transmitter on La Palma consisted of a motor-driven rotatable and tiltable platform with two transmitter lenses for the quantum channel, a 532nm beacon laser diode and a tracking CCD on it. The tracking lens focussed the 532nm laser light from Tenerife on the tracking CCD so the platform was actively locked to the OGS.

length of f=280mm focussed the light out of bare fiber on the OGS. With a specified theoretical spot size of 40cm at a distance of 8km the beam diameter at the OGS was about 10m, caused by fast beam wander and beam spreading due to diffraction and scattering in the turbulent atmosphere. Slowly varying atmospheric influences were compensated employing bidirectional closed-loop tracking of both telescopes on each other [13]. Therefore a 532nm beacon laser diode (see BLD-A in figure 2.4 and figure 2.5) was mounted on the telescope platform and aligned to point at the OGS on Tenerife. With a CCD camera and the provided tracking software at the receiver telescope, we were able to actively track the reflector telescope on the green spot from La Palma. Vice versa another 532nm beacon laser diode (see BLD-B in figure 2.8) was attached to the OGS and adjusted to point on La Palma. There a tracking lens focussed the green laser light from the OGS on a tracking CCD attached to the transmitter platform. A self designed [2] program analyzed the CCD image and controlled the stepper motors for the platform so that the transmitter telescope always pointed on the green laser from Tenerife. Due to a

[2]National Instruments Corporation, 11500 N Mopac Expwy, Austin, TX 78759-3504, USA; www.ni.com

tracking-beam spreading of typically 50m in diameter after the 144km, the beams didn't wander off the tracking apertures and couldn't get lost even for great beam wander. The bidirectional closed-loop tracking enabled us to actively lock both telescopes on a reference spot ensuring high link stability and less attenuation due to beam wander.

2.1.2 Receiver

On Tenerife, the Observatorio del Teide is situated ∼2400m above sea level in Izaña, an area that lies across three municipal districts - La Orotava, Fasnia and Güímar. It is home to Europe's finest solar telescopes and the OGS (Coordinates: 28°18'N 16°30'W 2393m). The OGS (see figure 2.6) houses a reflector telescope run by the ESA which was originally built for laser communication with satellites, thus being the perfect proof-of-concept test object for future quantum-communication schemes via satellites.

Figure 2.6: (left)The reflector telescope at (right) the European Space Agency's (ESA's) Optical Ground Station (OGS) on Tenerife.

Receiver Telescope

The receiver telescope at the OGS on Tenerife is a 1m Ritchey-Chrétien/Coudé reflector telescope with a focal length of f=38.33m and a field of view of 8 arcmin in the Coudé configuration. It was originally built for laser communication with satellites and therefore has high pointing velocity (up to 2° per second, with maximum acceleration of $0.5°/s^2$), high pointing precision (average error in all possible telescope orientations is less than 10 arcseconds) and high tracking precision (average error of 2.5 arcseconds per hour) [44]. Figure 2.7 shows the optical path in the receiver telescope with the Cassegrain and the Coudé focus.

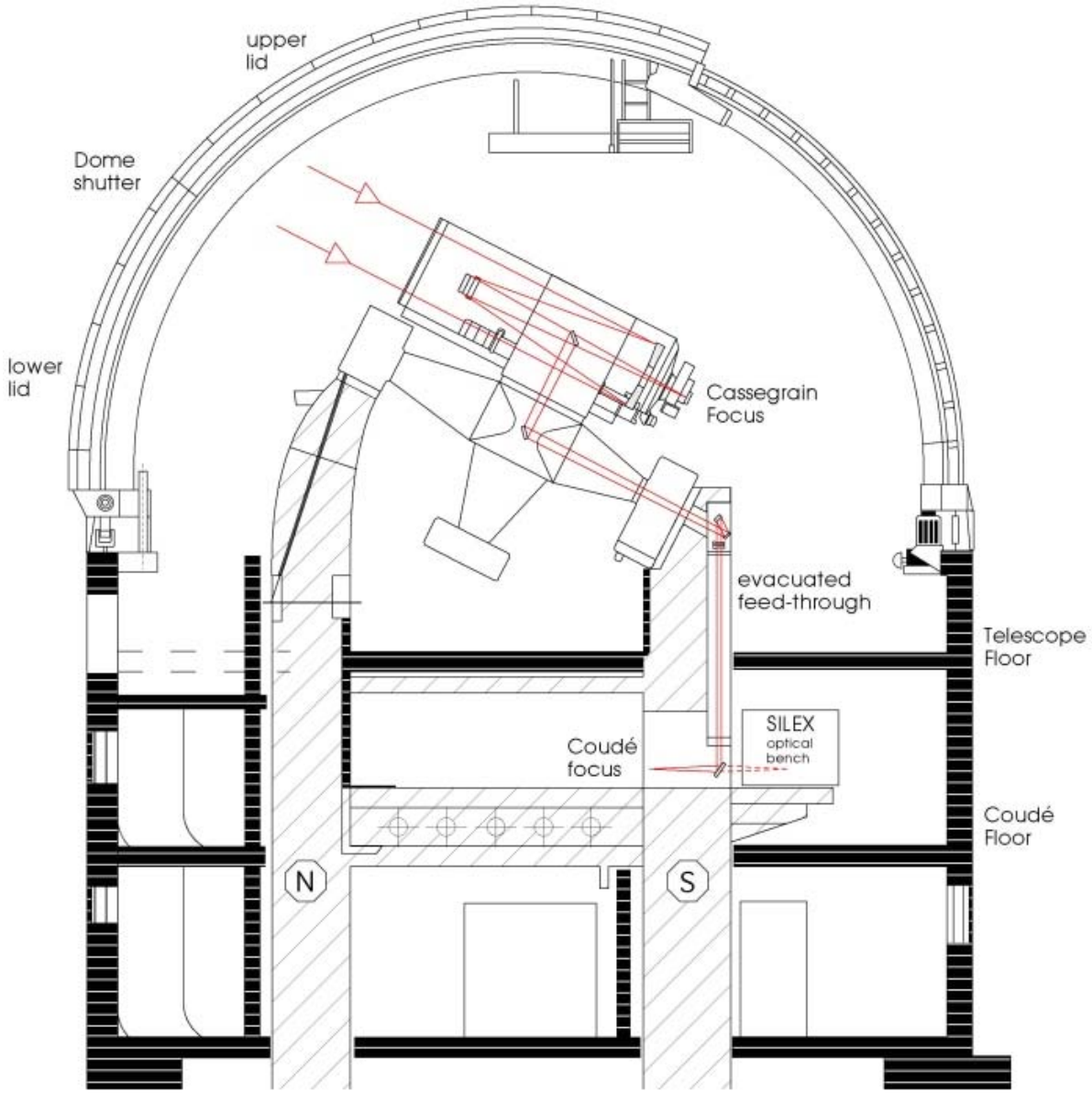

Figure 2.7: The optical path in the receiver telescope on Tenerife with the Cassegrain and Coudé focus [46]. Our detection module was attached to the optical table on the Coudé floor.

Detection Module

We attached our detection module (see chapter 3.2) to the optical table on the Coudé floor and therefore operated the telescope in the Coudé configuration which originally was used for communications tests with the Artemis satellite. Figure 2.8 shows the scheme of the telescope and the detection module implemented in the OGS. For accurate tracking and to minimize stray-light detection an adjustable iris in the Coudé focus reduced the effective field of view. After the Coudé focal plane a dichroic mirror (DM) mounted in a *Linos* [3] quick-change indexer transmitted the green tracking laser from La Palma to the tracking CCD and reflected photons of 810nm wavelength into the detection module (see figure 2.8). The indexer was necessary for quick and accurate removal and placement of the DM when switching between alignment of the detection module with an auxiliary lens system and the measurement process respectively.

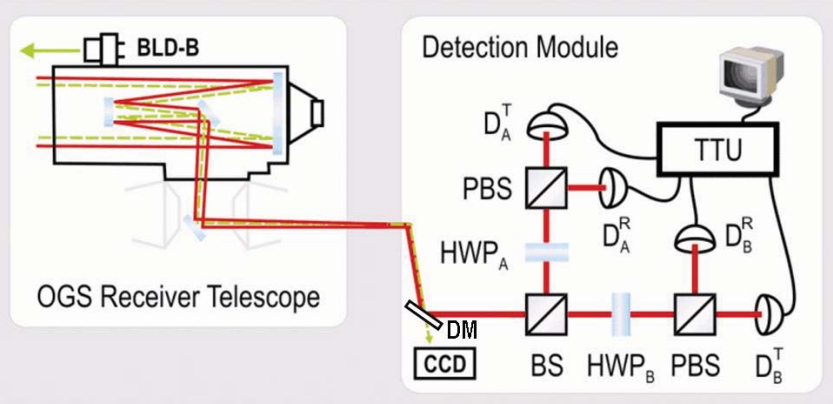

Figure 2.8: The experimental scheme of the receiver on Tenerife. A 532nm beacon laser diode (BLD-B) was attached to the 1m reflector telescope which guided the impinging beams to the detection module. Separation of the entangled photons and the tracking beam was achieved by a dichroic mirror after the Coudé focus reflecting 810nm and transmitting 532nm wavelengths. The detection module consisted of a 50/50 beam splitter (BS) and two polarization analyzers in arms A and B for the reflected and transmitted photons respectively. Two half-wave plates (HWP_A,HWP_B) and polarizing beam splitters (PBS_A,PBS_B) in the respective arms as well as the detectors D_A^T and D_A^R for the transmitted (T) and reflected (R) photons in arm A and D_B^T and D_B^R in arm B formed the polarization analyzers. The timetag unit (TTU) tagged every detector count with a timestamp and a self designed *LabView* program stored the data on the measurement PC.

[3]LINOS Photonics GmbH & Co. KG, Königsallee 23, D-37081 Göttingen, Germany; www.linos.com

2.2 Concept of the Coincidence Detection

In order to retrieve the S value of the CHSH inequality [24], we built up a setup for coincidence detection [47] where the incident photon pairs impinge on a 50/50 BS and will be either reflected or transmitted in the analyzer arms A or B respectively. As for each photon the probability of being reflected or transmitted is $\frac{1}{2}$, the probability for photon pairs to emit the BS in different output directions is $\frac{1}{2}\frac{1}{2} + \frac{1}{2}\frac{1}{2} = \frac{1}{2}$. So in half the cases a photon pair can be measured in different polarization bases A and B and therefore contribute to the S parameter. The CHSH form [24] of Bell's inequality [25] is defined by

$$S(\alpha, \beta, \alpha', \beta') = |E(\alpha, \beta) - E(\alpha, \beta')| + |E(\alpha', \beta) + E(\alpha', \beta')| \leqslant 2, \tag{2.3}$$

where the CHSH coincidence-expectation function E is

$$E(\alpha, \beta) = \frac{C_{TT}(\alpha, \beta) + C_{RR}(\alpha, \beta) - C_{TR}(\alpha, \beta) - C_{RT}(\alpha, \beta)}{C_{TT}(\alpha, \beta) + C_{RR}(\alpha, \beta) + C_{TR}(\alpha, \beta) + C_{RT}(\alpha, \beta)}, \tag{2.4}$$

with the coincidence detection rates $C_{i,j}$ between the detectors D^i_{A} and D^j_{B}. The indices i and j denote for transmission T or reflection R of a photon at the analyzers' PBSs in arm A and B respectively. Choosing the polarization-base angles in arm A and B to the Bell-test angles $\alpha = 0, \alpha' = \frac{\pi}{4}$ and $\beta = \frac{\pi}{8}, \beta' = \frac{3\pi}{8}$ respectively, leads to a theoretical maximal violation of the CHSH inequality for entangled photons with $S^{QM}_{max} = 2\sqrt{2} \approx 2.828 \nleqslant 2 = S^{Cl}_{max}$. Thus experimentally violating the CHSH inequality by more than 3 standard deviations σ proves the presence of entanglement.

3 Details

3.1 Polarization-Entangled Photon Source

The effect of spontaneous parametric down conversion (SPDC) in non linear crystals [48] is a widely-used method for the creation of entangled photon pairs. A pump photon is split up in two photons under conservation of momentum and energy. "Spontaneous" because of the spontaneous emission stimulated by vacuum fluctuations. "Parametric" denotes that the crystal state won't change due to the process, thus the combined energy and momentum of the produced photon pair match the energy and momentum of the pump photon, this is the so called phase matching criteria. "Down conversion" refers to the creation of two photons out of one in contrast to the inverse process called "up conversion". Depending on whether the created photons have the same or orthogonal polarization, we distinguish between type-I and type-II SPDC respectively.

In previous schemes based on nonlinear BBO bulk crystals [49] the produced photon pairs emit along two cones in such a way, that energy and momentum conservation is fulfilled and photons in one cone are horizontally polarized whereas in the other cone vertically polarized. Only for photon pairs emitting on the intersection lines of the cones one cannot distinguish from which cone they originate and therefore are entangled in polarization.

More recent schemes use periodically poled $KTiOPO_4$ (PPKTP) crystals [47; 50; 51] with the advantage of collinear generated photon pairs. Therefore a much bigger fraction of the produced photons can be collected, resulting in higher brightness of such sources. The most effective setup at the moment, combines an intrinsically phase-stable polarization Sagnac interferometer with the advantage of collinear SPDC and bidirectional pumping [50].

In figure 3.1 a polarization Sagnac interferometer is shown with its interfering clockwise and counterclockwise propagation possibilities for the pump photons. As one can verify, the vertical component of the pump beam is reflected at a 405nm and 810nm dual-wavelength polarizing beam splitter (PBS), rotated by $\frac{\pi}{2}$ at a dual-wavelength half-

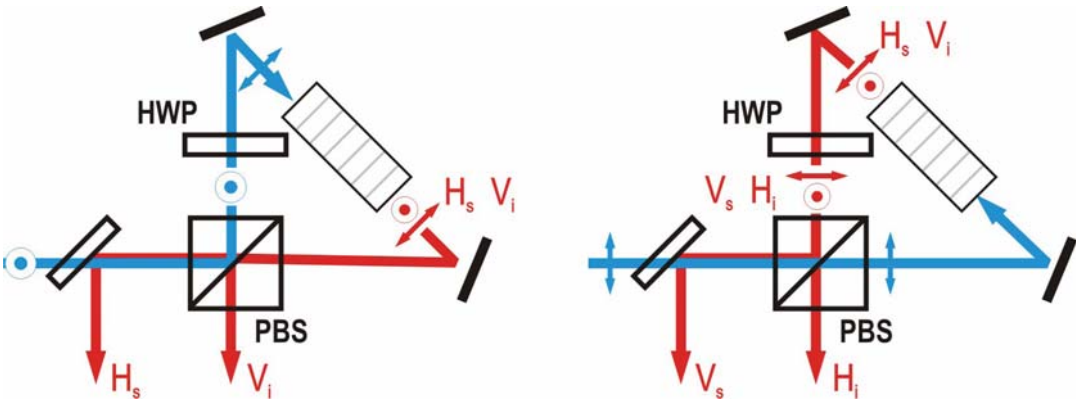

Figure 3.1: Scheme of the bidirectional pumped polarization Sagnac interferometer.(left) The vertically polarized component of the pump beam is reflected at the 405nm and 810nm dual wavelength polarizing beam splitter (PBS) and propagates clockwise. A dual wavelength half-wave plate (HWP) rotates the polarization state by $\frac{\pi}{2}$ and the now horizontally polarized pump beam is reflected in the PPKTP crystal producing an orthogonal polarized photon pair by type-II spontaneous parametric down conversion (SPDC). Due to the crystal's birefringence the horizontally polarized signal photon H_s propagates at higher velocity and emits ahead of the vertically polarized idler photon V_i. The PBS separates signal and idler photon into the left and right output mode respectively.
(right) The horizontal component of the pump beam transmits the PBS and propagates counterclockwise. After generation of a photon pair in the PPKTP crystal, the HWP rotates signal H_s and idler V_i photon by $\frac{\pi}{2}$ to V_s and H_i and therefore compensates the walkoff in respect to the case of clockwise beam propagation. At the PBS signal and idler are separated into the left and right output mode respectively but now the signal photon is horizontally polarized and the idler vertically polarized. Thus interference between the two propagation possibilities results in polarization entanglement of the output modes.

wave plate (HWP) and enters the PPKTP crystal with horizontal polarization. The two created photons are then separated at the PBS in respect to their polarization, so that the horizontally polarized photon ends up in the left arm and the vertically polarized one in the right arm. Due to different diffraction indices for the horizontal and vertical polarization in the nonlinear crystal, the horizontally polarized signal photon H_s propagates at higher velocity than the vertically polarized idler photon V_i, thus leading to a walkoff between the photons.

In the case of counterclockwise propagation, the horizontal component of the pump beam transmits the PBS and again creates an orthogonally polarized photon pair in the PPKTP crystal. The HWP rotates the photons by $\frac{\pi}{2}$ to compensate the walkoff in respect to the photons generated in clockwise propagation and the PBS reflects the vertically polarized photon into the left arm and transmits the horizontally polarized

one into the right arm. In the end the photons in the two output modes are entangled, because one does not know which polarization he will measure in one arm, but knows for sure, that the corresponding photon in the other arm will have orthogonal polarization.

3.1.1 Optimization of the Source

In order to find the optimal focussing parameters for four PPKTP crystals of different length (L=10,15,20,25 mm), we built up an optimization setup which is depicted in figure 3.2. We coupled the beam of a 405nm *Sacher* [4] laser diode into a polarization-

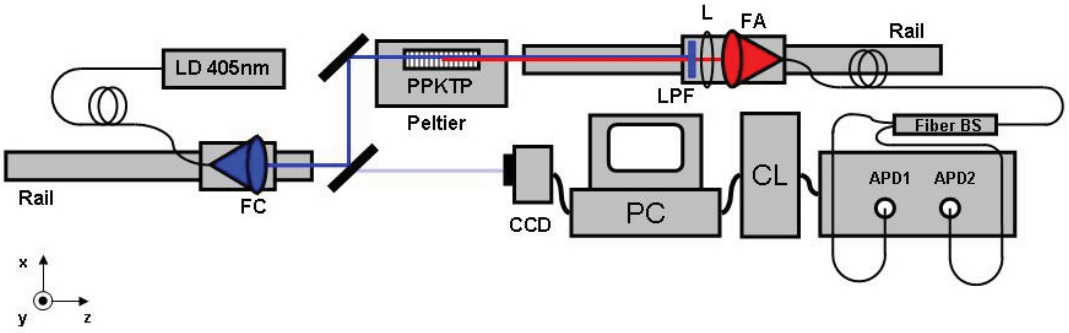

Figure 3.2: Optimization setup to find the optimal PPKTP crystal focussing parameters. A tuneable fiber coupler (FC) was mounted on a rail carrier to focus the 405nm pump beam via two laser mirrors into the PPKTP crystal at different spot waist sizes w_p. The first laser mirror transmitted a small fraction of the pump beam on a CCD-camera placed in the focal plane to monitor the spot waist size. Keeping the crystal temperature at 49.2°C with a Peltier oven allowed for generation of frequency degenerate photon pairs of 810nm wavelength. A longpass color glass filter (LPF) blocked stray laser light and a subsequent lens (L) coupled the photon pairs into a single-mode fiber connected to a fiber adapter (FA). Coincidence detection was done with a fiber beam splitter (BS), single-photon detectors (APD1, APD2) and a coincidence logic (CL) monitored by a self designed *LabView* program.

maintaining single-mode fiber and pumped the PPKTP crystal with 1mW of horizontally polarized light. In order to focus into the crystal at different spot waist sizes w_p, we used a *Schäfter+Kirchhoff* [5] fiber coupler mounted on a rail carrier. Tuning the lens position in the fiber coupler and the position of the fiber coupler on the rail, enabled us to set the desired spot waist sizes. Two laser mirrors guided the impinging pump beam through the crystal which was kept at a constant temperature of 49.2°C on a Peltier

[4]Sacher Lasertechnik GmbH, Rudolf Breitscheid Str. 1-5, D-35037 Marburg, Germany; www.sacher-laser.com

[5]Schäfter + Kirchhoff GmbH, Kieler Str. 212, D-22525 Hamburg, Germany; www.sukhamburg.de

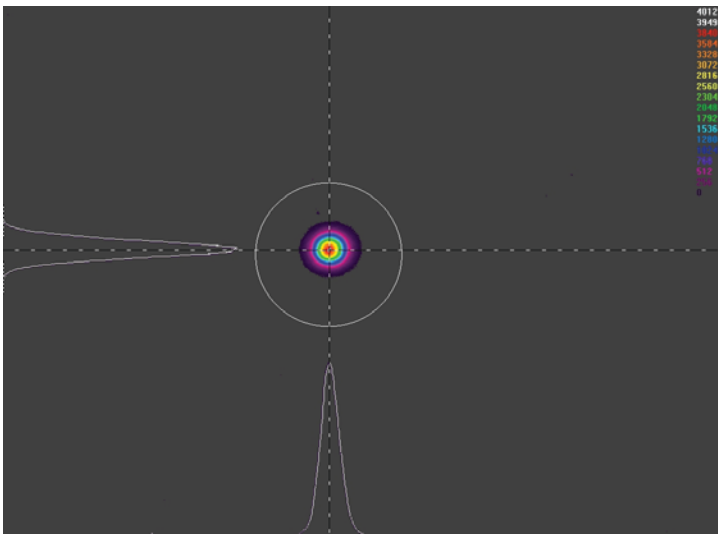

Figure 3.3: A typical gaussian beam profile in the focal plane of the pump beam recorded with a *Spiricon* CCD-camera. The software provided by the manufacturer allowed to measure the FWHM in x and y direction.

oven. At this specific temperature the generated photon pairs have the same wavelength of 810nm. The small fraction of light transmitted by the first laser mirror was used to check the spot waste size w_p with a *Spiricon* [6] CCD-camera placed in the focal plane of the pump beam. With the software provided by the manufacturer, we easily monitored the beam profile (see figure 3.3) to set the desired spot waist sizes w_p.

To collect the photon pairs generated by type-II SPDC, we mounted a coupling unit on a rail carrier to set different spot waist sizes $w_{s,i}$ for the signal s and idler i photons. The coupling unit consisted of a RG715 longpass color-glass filter to block stray laser light, an aspheric f=15.4mm lens adjustable in the xy plane and a fiber adapter adjustable in z direction. All components were attached to a 30mm cage system adjustable in the xy plane. In order to set the correct spot waist sizes $w_{s,i}$, we had to calibrate the coupling unit in respect to the rail position. So before mounting the oven we put the CCD-camera at the crystal position facing towards the coupling unit. Then we focused on the CCD-chip with an auxiliary 808nm laser light out of the single-mode fiber attached to the fiber adapter of the coupling unit. By measuring different spots dependent on the rail carrier position and fitting the data, we got a linear function which later allowed us to set the desired spot waist sizes $w_{s,i}$ by moving the coupling unit to the related position on the rail.

[6] Spiricon GmbH, Up de Worth 40, D-22927 Grosshansdorf, Germany; www.spiricon.de

The *SIFAM* [7] fiber beamsplitter (BS) attached to the fiber adapter and a *Perkin Elmer* [8] *SPCM-AQ4C* single-photon detector array (APD1,APD2) in connection with a self designed coincidence logic (CL) formed the detection assembly (∼40% detector quantum efficiency and 4.4ns coincidence time window). After careful collinear alignment of the whole setup, we measured the maximal coincidence count rate and its respective single count rates for each specific set of mode waist sizes $w_{p,s,i}$. This was done for each crystal length L and the obtained data let us estimate the optimal focussing parameters.

A closer look at the retrieved results and how our polarization-entangled photon source works will be given in the appended *Optics Express* paper "A wavelength-tuneable fiber-coupled source of narrowband entangled photons"(see chapter A.1.1).

[7]SIFAM Fibre Optics Ltd, Broomhill Way, Torquay, Devon, TQ2 7QL, United Kingdom; www.sifamfo.com

[8]PerkinElmer Inc., 940 Winter Street, Waltham, Massachusetts 02451, USA; www.perkinelmer.com

3.2 Detection Module

The verification of polarization entanglement between the photons generated by our source was realized with an analyzer setup similar to the one in [47]. To analyze the two-photon states on Tenerife, we built up a precast free-space detection module which could be easily integrated to the European Space Agency's (ESA's) Optical Ground Station (OGS). The main detection module consisted of a 50/50 beam splitter cube (BS), followed by a polarization analyzer in each arm, which was made up of a half-wave plate (HWP) and a polarizing beam splitter cube (PBS) directing the polarized light on the detectors. A timetag unit (TTU) electronically recorded each detector count together with detection time and channel number and the gathered data was stored on a local computer. For accurate alignment in our lab and later at the OGS, an auxiliary lens system in front of the detection module imitated the incident telescope beam at the OGS. Figure 3.4 shows the detection module together with the auxiliary lens system. The greyed Coudé-focus plane (CFP) , dichroic mirror (DM) and tracking CCD demonstrate the installations at the OGS.

3.2.1 Setup of the Detection Module

As the whole setup was designed for a collimated beam of 1.1 cm waist size we used 1" optics. All optical components were optimized and broadband antireflection coated for 810 nm wavelength to minimize losses in the setup and the used lenses were spherical plano-convex lenses. To get the detection module mobile, we mounted all components on a M6 threaded 450 x 600 x 12.5mm breadboard and put the breadboard on five 1"-posts of 25mm length. One post was placed in the center of the breadboard to ensure flatness and the others at each corner to make it attachable to optical tables via clamping forks. An enclosure system with black hardboards around the module and black masking tape on the rear side of the breadboard ensured good light isolation as needed for single-photon detection. As known from previous experiments, the beam from the telescope at the OGS emits ∼15cm above the optical table. To be able to adjust all optical components to the exact beam height at the OGS, we used height adjustable 1/2"-post assemblies and post collars to lock the height once found, but not the rotational degree of freedom for further alignment.

To simulate the incident beam at the OGS we used the auxiliary lens system as shown in figure 3.4. The fiber adapter (FA) and a f=50mm collimation lens were mounted in a 30mm cage system, with the lens in a z-axis cage translator to accurately

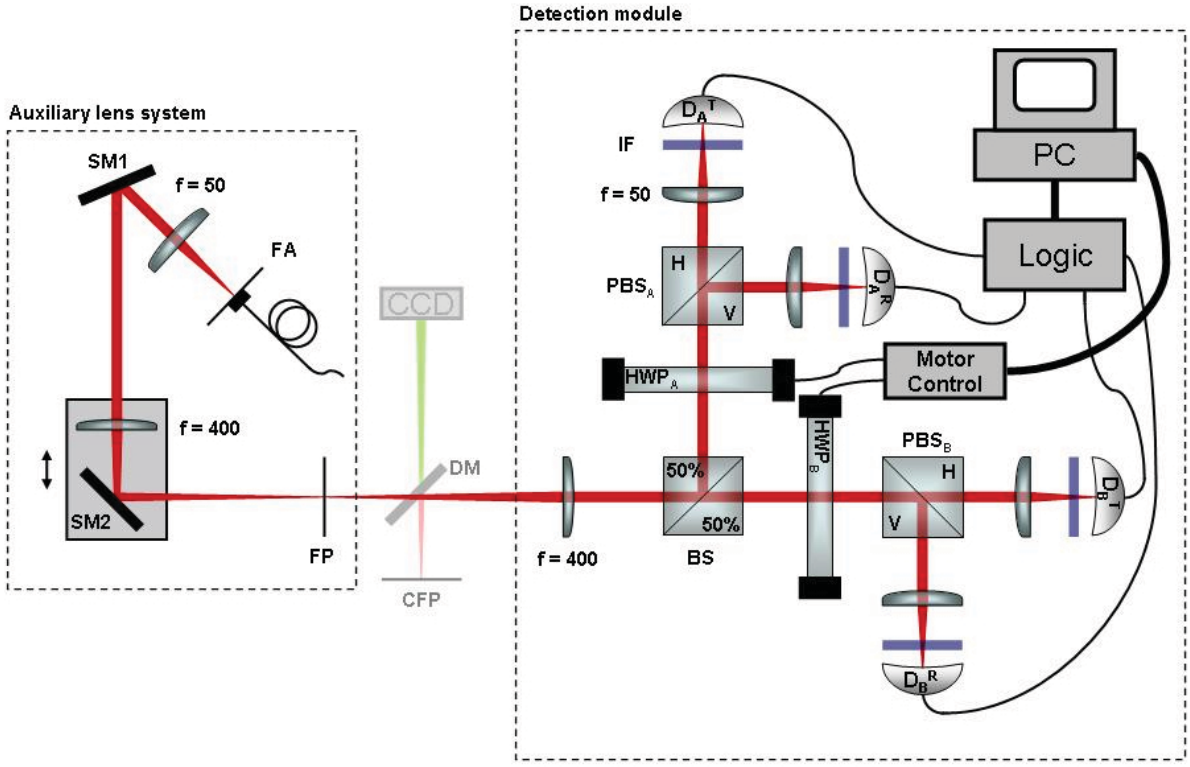

Figure 3.4: Setup scheme of the detection module and the auxiliary lens system. The auxiliary lens system was used to imitate the telescope beam at the Optical Ground Station (OGS), thus being able to accurately align the detection module. A f=50mm lens collimated the beam out of a single-mode fiber attached to a fiber adapter (FA). Two silver mirrors (SM1, SM2) on kinematic mirror mounts reflected the beam into the detection module. With a f=400mm lens in front of SM2 the collimated beam was refocussed in order to match the divergence of the impinging beam from the telescope. Mounting the f=400mm lens and SM2 on a translation stage and using kinematic mirror mounts allowed for optimal alignment of the auxiliary lens system in order to match height and direction of the telescope beam.
The f=400mm lens of the detection module collimated the incident beam before impinging on a 50/50 beam splitter (BS). The BS ether reflected or transmitted half the photons in the analyzer arms A or B respectively. Each analyzer arm consisted of a half-wave plate (HWP_A or HWP_B) mounted in a motorized rotation stage, a polarizing beam splitter (PBS_A or PBS_B) and two single-photon detectors (D_A^T, D_A^R or D_B^T, D_B^R. A f=50mm lens and a bandpass interference filter (IF) in front of each detector refocussed the beam onto the detectors' active areas and blocked stray light to minimize the dark count rate. All detectors were connected to a logic module for further signal processing and time tagging. A self designed *LabView* program controlled the detection process as well as the motorized rotation stages.

collimate the beam out of the single-mode fiber. The first silver mirror (SM1) reflected the collimated beam through a f=400mm lens onto the second silver mirror (SM2) which guided the beam into the detection module. Using two mirrors SM1 and SM2 on kinematic mirror mounts allowed us to vertically translate the beam to the desired beam height and SM2 together with the f=400mm lens mounted on a translation stage enabled us to horizontally translate the beam without changing the focal plane (FP) significantly. Thus we were able to fully match the incident beam at the OGS. The f=400mm lens of the auxiliary lens system simulated the Coudé focus and was positioned twice the focal length i.e. 800mm in front of the f=400mm collimation lens of the detection module. Mounted on a *Newport* [9] gimbal prism mount for accurate alignment, the 50/50 BS reflected or transmitted half the photons in the polarization analyzer arm A or B respectively. The polarization analyzer HWPs (HWP_A, HWP_B) were mounted in *Standa* [10] motorized rotation stages to quickly and automatically set the needed polarization-base angles. Also PBS_A and PBS_B were mounted on gimbal prism mounts and reflected or transmitted the vertically or horizontally polarized light respectively. In each arm of the PBSs a f=50mm lens refocussed the beam on a passively quenched *PerkinElmer* free-space single-photon detector with an active area of ∼0.5mm in diameter. A bandpass interference filter with a center wavelength of 810nm and 10nm FWHM was attached to the detector housing to block stray light and minimize the dark-count rate. The housing itself was mounted on a xyz-translation stage for accurate alignment of the detector's active area in respect to the focus of the f=50mm lens.

3.2.2 Motorized Rotation Stages

For fast and automated setting of the detection basis in the polarization analyzers, we used *Standa 8MR150* motorized rotation stages controlled by a *8SMC1-USBh-B2-4PS* 4-channel USB controller (see figure 3.5). The motorized rotation stages feature a resoluten of 0.6arcmin and consist of a limit switch in order to reset the stages to zero position. A built in bipolar stepper motor with 200 steps per revolution is controlled by a programmable microstep stepping-motor driver connected via USB 1.1 to the detection computer. Several self designed *LabView* programs implement VIs (i.e. *LabView* files) provided by the manufacturer to control the motors simultaneously from within the main measurement program.

[9] Newport Corporation, 1791 Deere Avenue, Irvine, CA 92606, USA; www.newport.com
[10] Standa, P.O.Box 377, 03012 Vilnius, Lithuania; www.standa.lt

Figure 3.5: The *Standa 8MR150* motorized rotation stage and its controller *8SMC1-USBh-B2-4PS*.

The program named *Init_Bell.vi* activates all selected motors and provides the controller with specific presets for the rotation stages. In order to ensure for correct detection-bases settings, *Reset2Switch.vi* reset all called rotation stages to zero position. Even though the limit-switch position didn't match the 0° mark of the rotation stage, we defined it as the zero position because it was the most repeatable and accurate one. Counting from the limit-switch position, the subprogram *Motion.vi* moved the called rotation stage to the desired HWP-angle setting. To find the optical axes of the HWPs in respect to the limit-switch positions, we placed each rotation stage between a horizontally and vertically adjusted polarizer and searched for minimum transmission of 808nm laser light.

3.2.3 Signal Processing

Single-Photon detection can be realized with avalanche photodiodes (APD) that operate in geiger mode. In this mode the APDs are reverse biased above the breakdown voltage in contrast to linear mode where the photodiodes are reverse biased slightly below the breakdown voltage. Biasing above the breakdown voltage leads to a very high electric field within the depleted region, thus even a single photon can initiate a self-sustaining avalanche multiplication process resulting in an avalanche current used to trigger a logic

Figure 3.6: Our passively quenched single-photon detector and the bandpass interference filter.

Si APDs – TE-Cooled

Typical Characteristics @ T = 0°C for "-TC" and -20°C for "-DTC"

Part #	Standard Package	PhotoSens. Diam.(mm)	Resp.@ 830nm (A/W)	Dark Curr. Id (nA)	Spect.Noise Curr. Dens. In (pA/√Hz)	Cap. @ 100kHz Cd (pF)	Resp. Time tr (ns)	NEP @ 830nm (fW/√Hz)	APD VOP Range (V)
C30902S-DTC [two-stage]	CC	0.5	128	1	0.02	1.6	0.5	0.16	160 - 250 [temp.depend.]

Figure 3.7: The specifications of the *Perkin Elmer C30902S-DTC* silicon APD.

pulse. Detecting a subsequent photon requires to quench the avalanche current in order to reset the APD for the next detection. The simplest way to do so is the passive quenching circuit with a resistor R_s in series to the APD. This resistor limits the output current of the APD and therefore the self-sustaining effect, allowing for resetting the bias voltage. However this method has a relatively long reload time and will cause detector dead times of a few μs, limiting the maximal count rate. In [52–54] more information about single-photon detection and the required electronics can be found.

Our detectors (see figure 3.6) were passively quenched *PerkinElmer* silicon APDs of type *C30902S-DTC* with a quantum efficiency of $\sim 25\%$. Figures 3.7 and 3.8 show the specifications and a drawing of the used APD respectively.

The APDs were mounted in a housing together with a small passive quenching circuit. Each detector was equipped with a high-voltage cable and a detection cable. The high-voltage cable connected the APD to a self designed high-voltage supply, biasing the APD with around +220V and cooling it to a temperature of about -30°C with the built

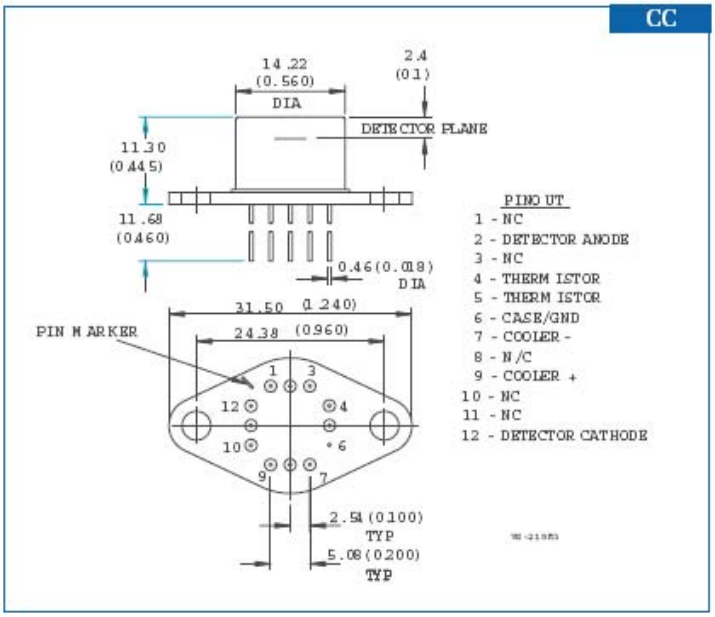

Figure 3.8: The technical drawing of the *Perkin Elmer C30902S-DTC* silicon APD.

in thermoelement. A *Tennelec* [11] *TC 454 Quad CFD* constant fraction discriminator (CFD) turned the detection signal into a well defined Nuclear Instrumentation Standard (NIM) logic pulse with "0" referring to 0V and "1" referring to -1V at 50Ω. Since the timetag unit works on basis of transistor-transistor logic (TTL) pulses ("0" and "1" refer to 0V and ∼3.3-5V respectively), the NIM signal was converted into a TTL signal by a *Phillips Scientific* [12] level translator. The TTL pulses triggered a self designed timetag unit which labeled every detection event with a 64-bit tag, containing the channel and a timetag with a resolution of 156ps. Simultaneously the gathered data was sent to the measurement computer via a *National Instruments* (NI)*PCI-6533* high-speed real-time digital-I/O connection with a maximum clock rate of 2MHz and a maximum data rate per channel of 2MBits/s. A self designed *LabView* program controlled the data acquisition process via the NI card from within the main measurement program and stored each detector click together with its timetag on the local hard drive. In figures 3.9 and 3.10 the signal processing scheme and a foto of the used equipment is shown.

[11] Tennelec was a US electronics company.
[12] Phillips Scientific, 31 Industrial Ave., Suite 1, Mahwah, N.J. 07430, USA; www.phillipsscientific.com

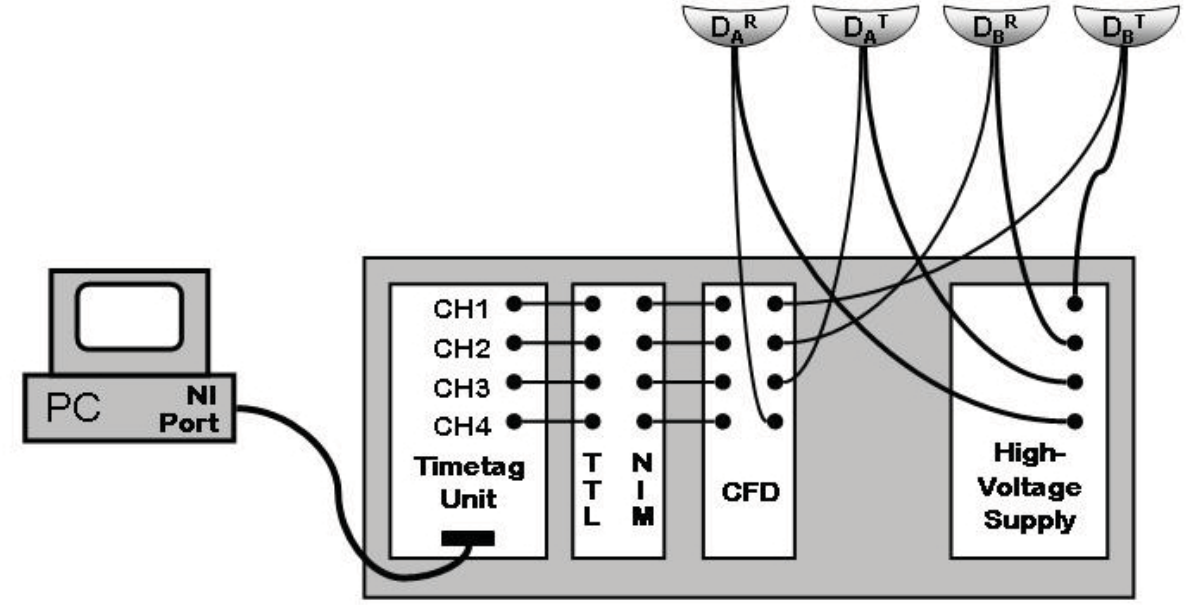

Figure 3.9: Scheme of the signal processing. A high voltage supply reverse biased the detectors D_A^R, D_A^T, D_B^R, D_B^T with ∼220V and cooled the APDs to about -30°C. Detector signals were converted into logic NIM pulses with a constant fraction discriminator (CFD) and translated to logic TTL pulses in the NIM/TTL level translator. The timetag unit provided each TTL signal of each channel with a time stamp and the processed data was transferred to a PC via a high-speed real-time *National Instruments* (NI) connection controlled by a self designed *LabView* program.

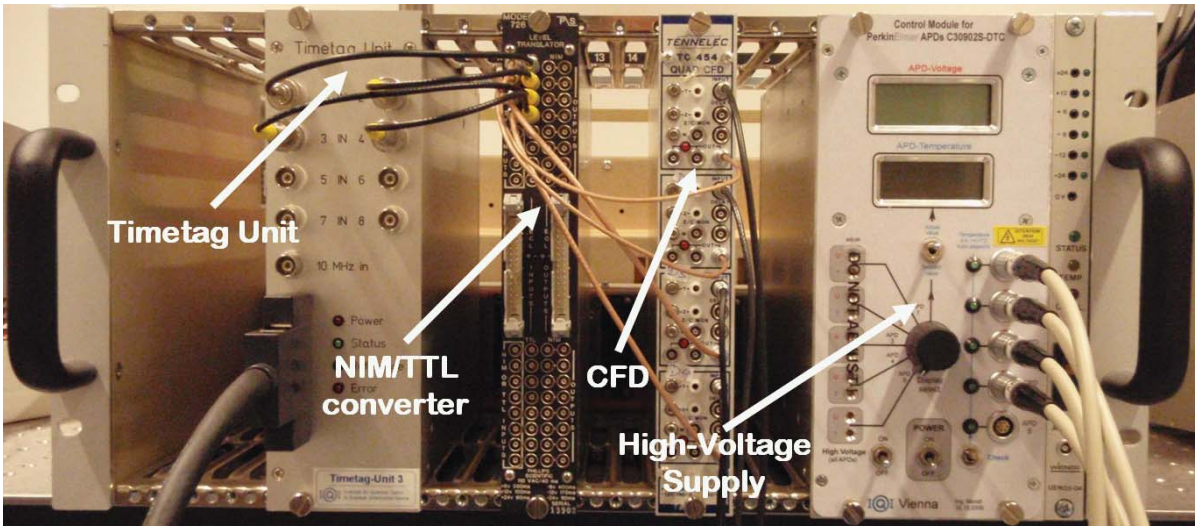

Figure 3.10: A foto of the equipment used for detection-signal processing. The timetag unit as well as the high voltage supply was built in-house.

3.2.4 Integration in the OGS

To ensure for accurate alignment of the detection module to the impinging beam from La Palma, it was necessary to match the alignment beam of the auxiliary lens system (see figure 3.4) as precise as possible with the beam from the telescope. Therefore we put an iris between the dichroic mirror (DM) and the collimation lens. The 808nm light from the auxiliary laser diode (ALD) on La Palma (see figure 2.4) was reflected by the DM on a second iris at the very end of the optical table. We set the aperture of the second iris to 11mm as expected for a collimated beam and adjusted it to the beam height at the Coudé focus. With the aid of an infrared viewer we aligned the DM, the first iris and the collimation lens to guide the beam parallel to the optical table through the second iris. Subsequently we removed the DM and aligned the auxiliary lens system. Therefore we coupled an 808nm laser diode in the auxiliary lens system (see figure 3.4)

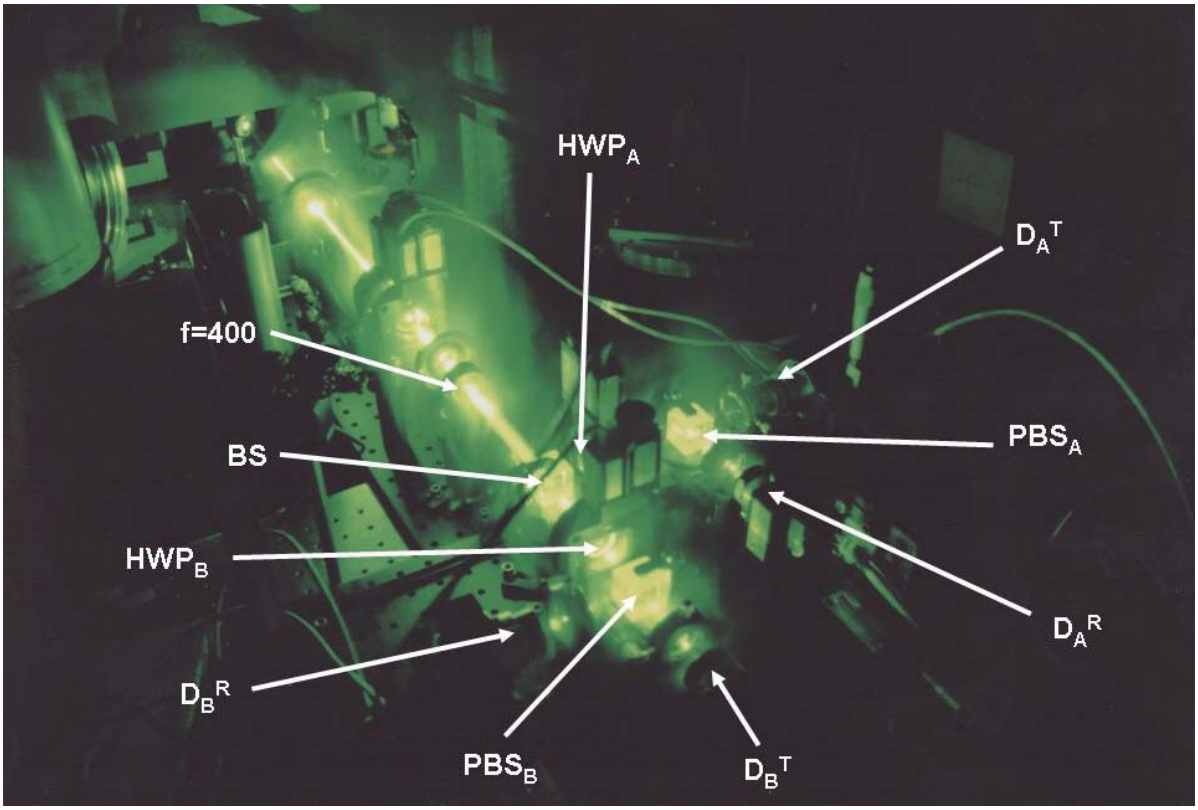

Figure 3.11: Coarse alignment of the detection module using a green laser for better visibility of the optical path and back reflections. A 532nm laser diode was coupled in a single-mode fiber connected to the auxiliary lens system, shining into the detection module. After adjustment of all components to the beam height, we orientated the optical components orthogonal in respect to the beam direction via back reflections.

and adjusted its components until the beam exactly passed through the first and second iris, thus matching the beam of the telescope.

Then we put the detection module on the optical table and attached it via clamping forks. For better visibility during the coarse alignment, we coupled a green laser in the auxiliary lens system and shined into the detection module. The height and orientation of each component was adjusted to the green beam shown in figure 3.11.

To adjust the orientation of the optical elements orthogonal to the beam direction, we used back reflections on the surfaces. We then coupled an attenuated 808nm laser into the auxiliary lens system, put a polarizer between the collimation lens and the BS and fine tuned the whole setup on single-photon level by maximizing the detector counts for 45° polarized photons measured in the $|H/V\rangle$ basis. Therefore we connected the outputs of the NIM/TTL level translator in figures 3.9 and 3.10 with a coincidence logic (CL) as used in figure 3.2 and continuously monitored the detector counts for each channel with our self designed *LabView* program.

4 Measurement and Analysis

4.1 Measurement

4.1.1 Measurement Procedure

Before starting the correlation measurement we had to set up a common polarization reference frame between both parties and adjust the phase Φ of the state Ψ in equation 2.1 to get a $|\Psi^-\rangle$ state at the receiver (a detailed description of this procedure is given in the appended paper "Testing quantum communication with photonic Bell states over a 71dB loss free-space channel" (see chapter A.1.2).

Once everything was well adjusted, we started the correlation measurement for the four coincidence-expectation values contributing to the CHSH inequality (see equation 2.3). The self designed *LabView* measurement program automatically set the wave plates $\mathrm{HWP_A}$ and $\mathrm{HWP_B}$ to the desired positions and started data acquisition for the first correlation measurement. The "clicks" together with the respective time stamps of each detector were stored in a data file on the hard drive of the measurement computer. After a measurement time of 900s a $\mathrm{C^{++}}$ program was called from within the measurement program and calculated the cross correlations between the detectors in a time range $\pm$250ns around zero delay with a resolution of 250ps. The cross-correlation output file was of type *.csv and could be imported in *Visual Basic* for further analysis. This procedure was repeated for the remaining sets of Bell angles and in total 10800s of data were acquired in three consecutive nights.

4.1.2 Measurement Data

The obtained data showed two coincidence peaks at $\pm$50ns delay τ between two detector files as expected due to the 10m delay fiber in one output arm of the source on La Palma. With a time resolution of 250ps, this corresponds to the indices 800 and 1200 at which index 1000 corresponds to $\tau = 0$. Figure 4.1 shows the data of the four relevant detector combinations ($D_1D_3 \widehat{=} C_{TT}$, $D_1D_4 \widehat{=} C_{RT}$, $D_2D_3 \widehat{=} C_{TR}$, $D_2D_4 \widehat{=} C_{RR}$) obtained by a 900s

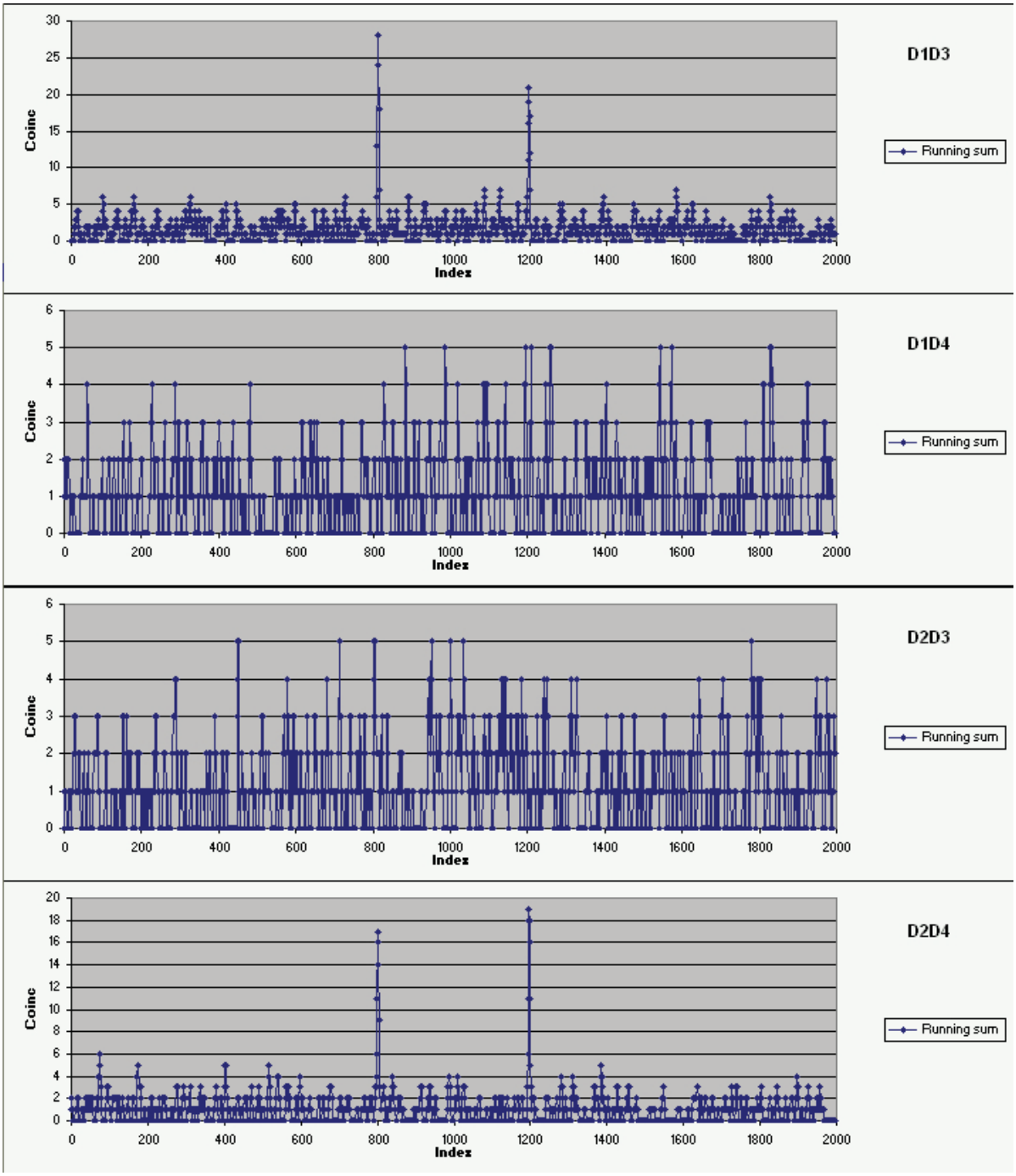

Figure 4.1: The coincidence data of the four relevant detector combinations ($D_1D_3 \widehat{=} C_{TT}$, $D_1D_4 \widehat{=} C_{RT}$, $D_2D_3 \widehat{=} C_{TR}$, $D_2D_4 \widehat{=} C_{RR}$) with a coincidence window of 1.25ns. C_{TT} and C_{RR} show distinct peaks at $\pm$50ns, whereas C_{RT} and C_{TR} only attained noise.

measurement for E($\pi/4, 3\pi/8$) and a coincidence-time window of 1.25ns. The files for the C_{TT} and C_{RR} coincidences show two distinct coincidence peaks, whereas in C_{RT} and C_{TR} only noise was registered. A coincidence peak at $\tau = -50$ns corresponds to the case where the delayed photon ends up in the first detector, as the count pattern of the second detector is shifted by -50ns in respect to the first detector. Vice versa for the $\tau = +50$ns peak, where the delayed photon ends up in the second detector.

A self-designed analysis software automatically searched for the coincidence peaks in predefined areas and allowed for further analysis.

4.2 Analysis Software

In order to simplify and speed up data analysis, we designed a *Microsoft Excel* sheet with macros to call *Visual Basic* sub procedures. The user interface of the *Microsoft Excel* sheet shown in figure 4.2 supported the following features:

Buttons

Import n ***files starting with file above*** - Before analyzing, n consecutive data files starting with the file in *File path* had to be imported to a three dimensional array $data(49, 1999, 7)$ where up to 50 files (0..49) with 2000 time-delay dependent cross-correlation data points in 8 channels were stored. Table 4.1 shows the channel allocation of the *data* array.

Channel	Allocation
0	Time bins
1	$D_1 D_2 \doteq D_{\mathrm{B}}^T D_{\mathrm{B}}^R$
2	$D_1 D_3 \doteq D_{\mathrm{B}}^T D_{\mathrm{A}}^T \doteq C_{TT}$
3	$D_1 D_4 \doteq D_{\mathrm{B}}^T D_{\mathrm{A}}^R \doteq C_{RT}$
4	$D_2 D_3 \doteq D_{\mathrm{B}}^R D_{\mathrm{A}}^T \doteq C_{TR}$
5	$D_2 D_4 \doteq D_{\mathrm{B}}^R D_{\mathrm{A}}^R \doteq C_{RR}$
6	$D_3 D_4 \doteq D_{\mathrm{A}}^T D_{\mathrm{A}}^R$
7	Sum of channels 1-6

Table 4.1: The channel allocation of the *data* array which contains the imported files.

Clear data - Clears all text boxes except the *Left/Right peak positions*, the *File count* and the *Coincidence window* text boxes. Any additional sheet except the *Control* sheet will be deleted as well.

Plot global data with m ***bins coincidence window*** - For a global overview and a first estimation at which positions the coincidence peaks will be found, we plotted the raw data (m=1) and inserted the approximate peak positions in the corresponding text boxes of the *Excel* sheet. Then we limited the coincidence-search volumes to $\pm$*Search delta* time bins (one time bin refers to a delay of 0.25ns) around the peak positions. These settings only were necessary for the first measurements as the coincidence-peak positions of all detector combinations didn't vary very strong

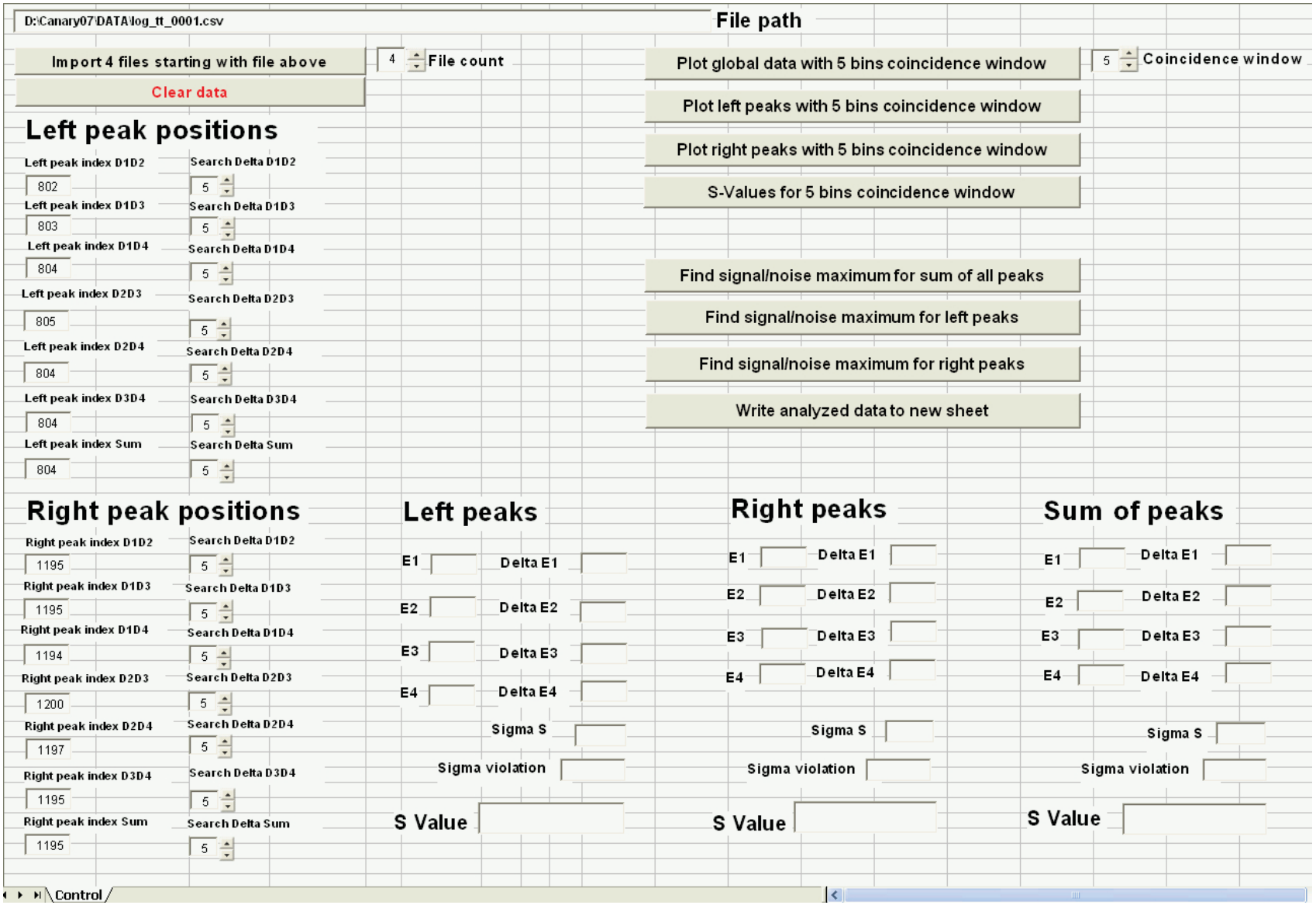

Figure 4.2: This self designed *Microsoft Excel* sheet imported the output files of the C^{++} cross-correlation program in a *Visual Basic* data array for further analysis. It supports S-Value calculation, data plotting, S/N-ratio calculation and export operations.

for different measurement runs and stayed in the search volumes defined by the peak positions and *Search delta*.

Plot left/right peaks with m ***bins coincidence window*** - Plotted the correlations for a coincidence window of $m \times 0.25$ns in a time window $\pm$*Search delta*$\times$0.25ns around the left or right peaks respectively.

S-Values for m ***bins coincidence window*** - Calculates the coincidence-expectation functions (see equation 2.4) and the S-Values (see equation 2.3) for the first four imported files as well as the standard deviations ΔE (see equation 5.9) and σ (see equation 5.10) of the expectation functions and the S-Value respectively. The text box *Sigma violation* indicates the violation of the maximal S-Value for local hidden variable models [24] $S_{max}^{Cl} = 2$ in terms of σ (see equation 5.11).

Find signal/noise maximum for sum of all/left/right peaks - Calculated and plotted the signal-to-noise (S/N) ratio

$$\frac{S}{N} = \frac{Coincidences \; - \; Background}{Background} \tag{4.1}$$

for the sum of the peaks (C_{TT}, C_{RT}, C_{TR}, C_{RR}), the left or the right peaks respectively for 10 different coincidence windows from 0.25ns to 2.5ns. The mean background level of each channel was retrieved from the first 200 data points with -250ns to -200ns delay which was well separated from the coincidence peaks at $\pm$50ns.

Write analyzed data to new sheet - Retrieved the peak coincidences of all detector combinations in all imported files, calculated the respective coincidence-expectation values and standard deviations ΔE and wrote the data into a new sheet. The such formatted data could be easily copied to another *Excel* file where the outcomes of the consecutive measurement runs were merged to obtain the overall S-Value and σ-violation.

Peak-search algorithm

In almost all of the analysis options a running summation of the raw data over the coincidence window and a subsequent peak-search algorithm were performed internally. The source code in listing 4.1 shows how this was implemented by the example of finding

```
'reset variables peak(filenumber,col)=False peak_count(filenumber,col)=0 left_global_pea
local_peak(filenumber,col)=0 local_peak_index(filenumber,col)=0 left_global_peak_index(

For i=left_peak_index(col)-Int(averaging/2)-left_peak_delta(col) _ To left_peak_index(c

    'sum over coincidence window
    avrg(filenumber,i,col)=0
    For j=0 To averaging
        avrg(filenumber,i,col)=avrg(filenumber,i,col)+data(filenumber,i+j,col)
    Next j

    'search algorithm
    If avrg(filenumber,i,col)>local_peak(filenumber,col) Then
        peak(filenumber,col)=True
        local_peak(filenumber,col)=avrg(filenumber,i,col)
        local_peak_index(filenumber,col)=i
    End If

    If (avrg(filenumber,i,col)<local_peak(filenumber,col)) _
    And (peak(filenumber, col)=True) Then
        If left_global_peak(filenumber,col)<local_peak(filenumber,col) Then
            left_global_peak(filenumber,col)=local_peak(filenumber,col)
            left_global_peak_index(filenumber,col)=local_peak_index(filenumber,col)
        End If
        peak(filenumber,col)=False
        peak_count(filenumber,col)=peak_count(filenumber,col)+1
        local_peak(filenumber,col)=avrg(filenumber,i,col)
    End If

Next i
```

Listing 4.1: *Visual Basic* source code of the running summation and peak-search algorithm

a left coincidence peak near -50ns detector delay. First, all used variables were reset. The subsequent main FOR loop ranged from minus to plus *Search delta* centered at the approximate peak position which was corrected by half the summation range as the peak position depends on the coincidence-time window. In the running summation the coincidences of consecutive time slots were successively summed up which is equivalent to an extension of the coincidence window. The first IF expression searched for local peaks and stored the coincidence peak with the respective position. If a local peak was found, the commands of the second IF expression were carried out. The embedded IF expression searched for the greatest local peak and thus for the global peak. Implementation of this code in FOR loops over the channels and files deliver the coincidence peaks of all detector combinations in every imported file. Therefore allowing the calculation of the coincidence-expectation functions to obtain the S-Value as well as signal-to-noise (S/N) ratios.

5 Results

The quality of the aligned detection module was characterized by the polarization contrast

$$V_{H/V} = \frac{D_{\mathrm{A}}^{\mathrm{T}}(0) + D_{\mathrm{B}}^{\mathrm{T}}(0) - D_{\mathrm{A}}^{\mathrm{R}}(0) - D_{\mathrm{B}}^{\mathrm{R}}(0)}{D_{\mathrm{A}}^{\mathrm{T}}(0) + D_{\mathrm{B}}^{\mathrm{T}}(0) + D_{\mathrm{A}}^{\mathrm{R}}(0) + D_{\mathrm{B}}^{\mathrm{R}}(0)} \tag{5.1}$$

for horizontally polarized incident photons, which were measured in the $|H/V\rangle$ basis. $D_m^n(\theta_m)$ with $m \in \{A, B\}$ and $n \in \{T, R\}$ denote the background-subtracted detector counts for the respective detector in the detection basis rotated by θ_m due to the HWP_m set to $\theta_m/2$. Together with similar measurements (see table 5.1) this yielded a mean polarization contrast of 99.5%.

Input pol.	$(\theta_{\mathrm{A}}, \theta_{\mathrm{B}})$	Pol. contrast
H	$(0, 0)$	99.5%
H	$(\pi/2, \pi/2)$	99.4%
$+\pi/4$	$(\pi/4, \pi/4)$	99.6%
$+\pi/4$	$(-\pi/4, -\pi/4)$	99.5%

Table 5.1: Polarization contrast of the detection module for specific input polarization of the photons measured in the polarization bases of the arms A and B rotated by θ_{A} and θ_{B} respectively.

In three consecutive nights from the 15^{th} until the 18^{th} of June 2007, we accumulated coincidences over a net amount of 9900s. The first measurement night contributed to $\mathrm{E}(0, 3\pi/8)$ with 48 coincidences over 900s. Next night we measured 66 coincidences over 900s contributing to $\mathrm{E}(0, \pi/8)$, 112 coincidences over 1800s contributing to $\mathrm{E}(\pi/4, \pi/8)$ and 52 coincidences over 900s contributing to $\mathrm{E}(\pi/4, 3\pi/8)$. In the last night we obtained 116 coincidences over 1800s contributing to $\mathrm{E}(0, \pi/8)$, 71 coincidences over 900s contributing to $\mathrm{E}(\pi/4, \pi/8)$, 140 coincidences over 1800s contributing to $\mathrm{E}(0, 3\pi/8)$ and 100 coincidences over 900s contributing to $\mathrm{E}(\pi/4, 3\pi/8)$. This lead to the total correlation values and coincidences shown in table 5.2, at which all data was obtained for a coincidence-time window of 1.25ns.

(θ_A, θ_A)	$\mathrm{E}(\theta_A, \theta_B)$	$\Delta\mathrm{E}(\theta_A, \theta_B)$	$\sum_{i,j\in\{T,R\}} C_{i,j}^{900s}$
$(0, \pi/8)$	-0.604	0.059	182
$(\pi/4, \pi/8)$	0.672	0.055	183
$(0, 3\pi/8)$	0.638	0.056	188
$(\pi/4, 3\pi/8)$	0.697	0.058	152

Table 5.2: The experimental polarization correlations $\mathrm{E}(\theta_A, \theta_B)$ for the CHSH inequality. The net accumulation time was 9900s and the standard deviations $\Delta\mathrm{E}(\theta_A, \theta_B)$ were calculated assuming Poissonian photon-count statistics.

This leads to an S-value of

$$S^{Exp} = 2.612 \pm 0.114. \tag{5.2}$$

Hence we violated the CHSH inequality by more than 5 standard deviations, which proves the faithful transmission of entanglement over 144km.

The standard deviation $\sigma = 0.114$ of the S-value was calculated assuming Poissonian statistics for the photon-count process over a finite time interval [55]. Therefore the standard deviation $\Delta C_{i,j}$ of the coincidence rate $C_{i,j}$ is

$$\Delta C_{i,j}(\alpha, \beta) = \sqrt{C_{i,j}(\alpha, \beta)} \quad \text{with} \quad i, j \in \{T, R\}. \tag{5.3}$$

With the definition of the terms

$$C_{\parallel}(\alpha, \beta) = C_{T,T}(\alpha, \beta) + C_{R,R}(\alpha, \beta) \tag{5.4}$$

$$C_{\perp}(\alpha, \beta) = C_{T,R}(\alpha, \beta) + C_{R,T}(\alpha, \beta) \tag{5.5}$$

and the respective errors

$$\Delta C_{\parallel}(\alpha, \beta) = \sqrt{C_{\parallel}(\alpha, \beta)} \tag{5.6}$$

$$\Delta C_{\perp}(\alpha, \beta) = \sqrt{C_{\perp}(\alpha, \beta)} \tag{5.7}$$

equation 2.4 can be written in the form

$$E(\alpha, \beta) = \frac{C_{\parallel}(\alpha, \beta) - C_{\perp}(\alpha, \beta)}{C_{\parallel}(\alpha, \beta) + C_{\perp}(\alpha, \beta)}. \tag{5.8}$$

Gaussian error propagation leads to the standard deviation

$$\Delta E(\alpha, \beta) = \sqrt{\left(\frac{\partial E}{\partial C_{\parallel}} \Delta C_{\parallel}\right)^2 + \left(\frac{\partial E}{\partial C_{\perp}} \Delta C_{\perp}\right)^2} = \frac{2\sqrt{C_{\parallel}^2(\alpha, \beta) C_{\perp}(\alpha, \beta) + C_{\parallel}(\alpha, \beta) C_{\perp}^2(\alpha, \beta)}}{(C_{\parallel}(\alpha, \beta) + C_{\perp}(\alpha, \beta))^2} \tag{5.9}$$

and finally

$$\sigma = \Delta S(\alpha, \beta, \alpha', \beta') = \sqrt{\Delta E^2(\alpha, \beta) + \Delta E^2(\alpha, \beta') + \Delta E^2(\alpha', \beta) + \Delta E^2(\alpha', \beta')}. \quad (5.10)$$

This allows to calculate the violation of the CHSH inequality in terms of the standard deviation σ

$$\sigma_{\text{violation}} = \frac{S^{\text{Exp}} - 2}{\sigma} \quad (5.11)$$

To get an impression of the quality of our measurements, we calculated the S-values and σ-violations (in terms of the respective σ) by incrementally increasing the measurement time. As presented in figure 5.1, the S-value violated the CHSH inequality already for the first value and the violation exceeded the 3σ barrier already at the third data point.

Moreover, a close look at the single-photon and photon-pair link attenuations revealed that the two transmitter modes were completely independent as the average net attenuations were 32.1dB and 64.2dB respectively. This proves that our experiment truly emulated the scenario with two separated receivers.

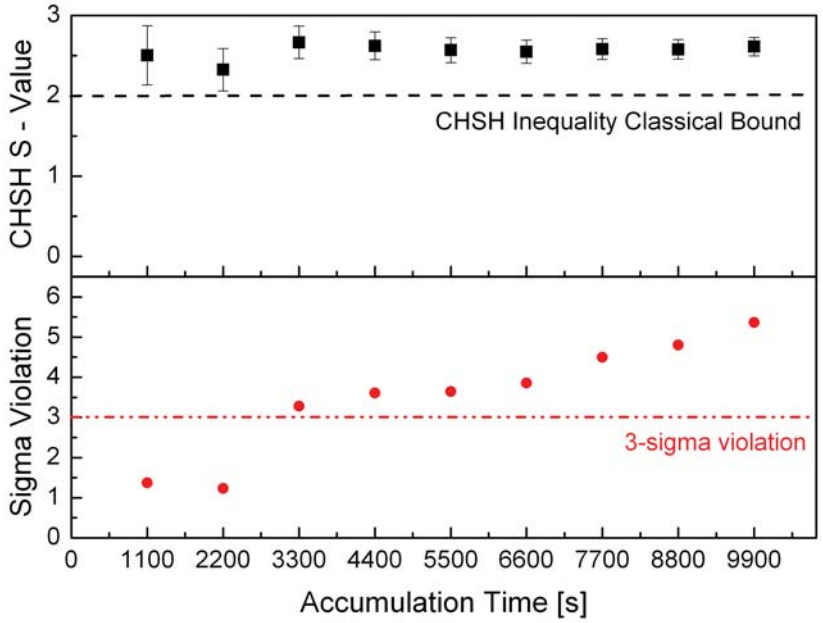

Figure 5.1: The time evolution of the S-value (black boxes) and the σ-violation (red bullets).

A more detailed view on the achieved results will be given in the appended paper "Testing quantum communication with photonic Bell states over a 71dB loss free-space channel" (see chapter A.1.2), which was submitted to *Nature Physics*.

6 Conclusion and Outlook

We successfully emulated conditions that are expected for a LEO-satellite down link with two ground receivers and we faithfully transmitted a maximally quantum-entangled state over a long-distance free-space link of 144km. The violation of the CHSH inequality by more than 5 standard deviations proves that photonic entanglement endures a 144km transmission through turbulent atmosphere. Concerning the independence of both transmitter modes, the experiment can also be interpreted as a source-in-the-middle scenario with two receiver stations separated by 288km.

We successfully employed space hardware, as the receiver station was originally built for laser communication with satellites. Additionally, with a pump power of only 20mW, our highly efficient and compact source yielded a pair production rate of 10^7 pairs/s, which meets the estimated optimal amount for space based quantum communication [5]. Thus our optimized source for polarization-entangled photon pairs is proposed to be implemented in a satellite-borne quantum transceiver [12]. These results pave the way for first quantum communication experiments in space and the ESA already plans the implementation of a satellite-borne platform for quantum communication with a launch date by end of 2014 [56].

The implementation of more advanced protocols such as quantum dense coding or quantum teleportation (see chapter 1.2.3) requires two-photon interference on a beam splitter. To check the feasibility of such schemes, we performed a test with classical light out of the 808nm auxiliary laser diode (ALD) on La Palma. Figure 6.1 shows the scheme of the interference module we used. The incident beam was polarized in 45° direction (45° Pol) and a polarizing beam splitter (PBS) reflected and transmitted the vertical and horizontal beam components respectively. Rotation of the vertical polarization component to horizontal polarization by a half-wave plate and subsequent recombination of the beams on a 50/50 beam splitter (BS) lead to interference. A CCD-camera slightly out of focus of the $f = 50$ lens captured the beam profile with the shadow of the secondary telescope mirror in the center. As depicted in figure 6.2 (right), we clearly observed interference fringes when rotating the vertical polarization component to horizontal (i.e.

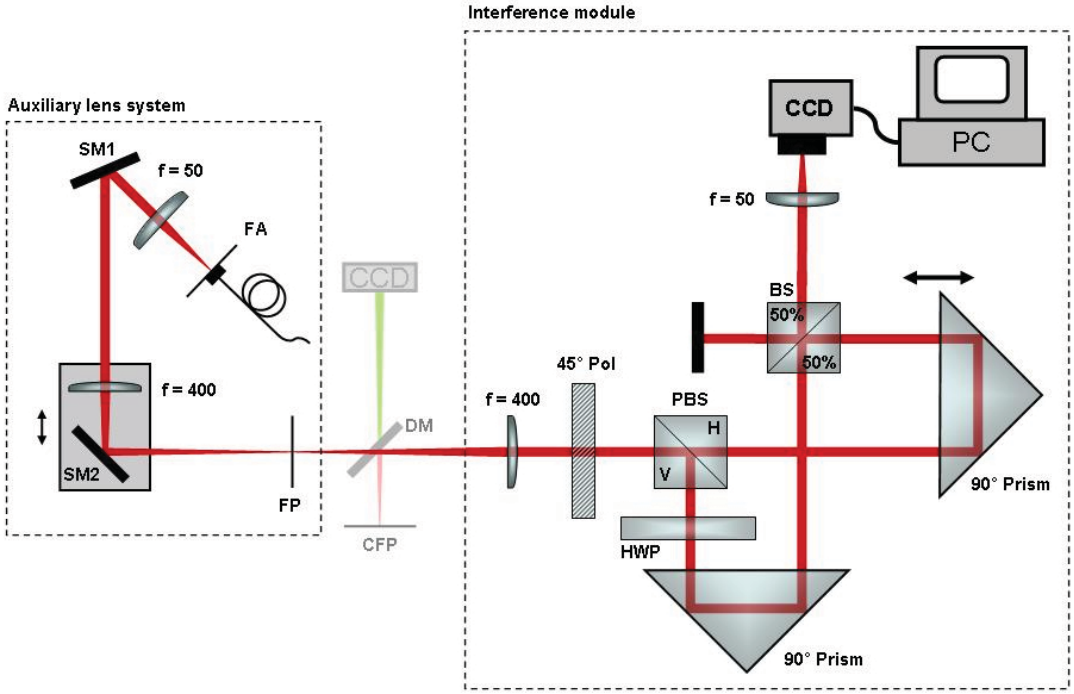

Figure 6.1: The setup for the interference test. The polarizer (45° Pol) is adjusted in 45° direction and the polarizing beam splitter (PBS) reflects and transmits the vertical and horizontal beam components respectively. A half-wave plate (HWP) rotates the vertical polarization component to horizontal and both components are recombined on the 50/50 beam splitter (BS). In one output arm of the BS a CCD camera is placed to capture the interference fringes.

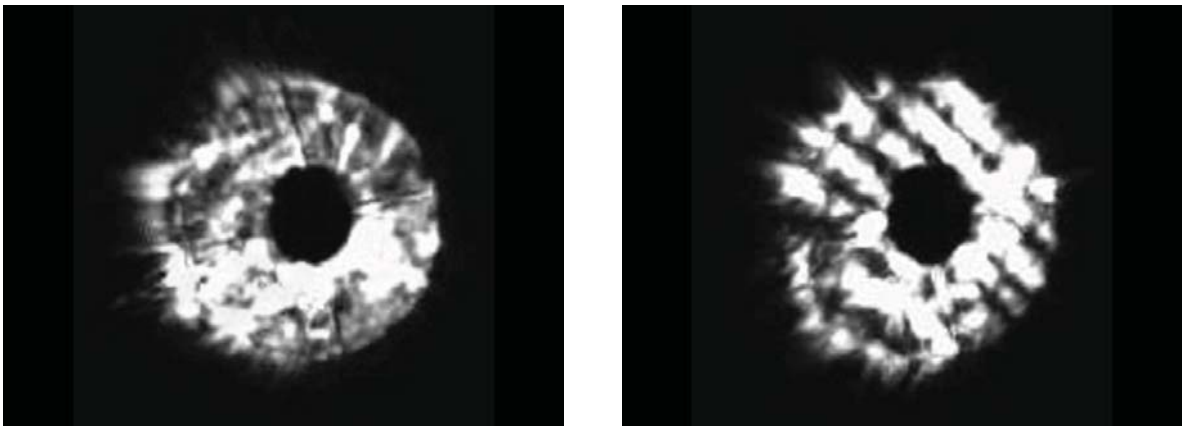

Figure 6.2: The snap-shots of the interference test captured with a CCD camera slightly out of the focal plane. The black disk in the center is the shadow of the secondary telescope mirror. One can clearly distinguish between (left) no interference and (right) interference fringes.

$\theta_{\mathrm{HWP}} = 45°$), whereas the fringes vanished without the rotation (i.e. $\theta_{\mathrm{HWP}} = 0°$). Although the experimental test didn't show two-photon but single-photon interference, the obtained result is a sufficient prove of the feasibility of two-photon interference for upcoming long-distance free-space experiments.

In the near future, an entanglement-based space-time experiment is planned at the 144km free-space inter-island link (see figure 6.3 (left)). Two quantum-random-number generators (QRNG) (a and b) operate outside the source's light cone and ensure for intrinsic random measurement settings at Alice (A) and Bob (B) respectively. Hence, the chosen measurement bases cannot be known by the entangled pair in the moment of creation. One photon of the entangled pair is measured locally after a delay of $\sim 30\mu$s and the partner photon is sent over the 144km free-space link to Bob (B). As shown in figure 6.3 (right), for an observer who moves at v/c times the speed of light

$$\frac{v}{c} = \frac{c\,\Delta\tau}{\Delta x} = \frac{c\,(\tau_B - \tau_A)}{L} = \frac{c\,(480\mu s - 30\mu s)}{144km} \approx 0.938 \tag{6.1}$$

Alice and Bob simultaneously measure the entangled photons.

On the rooftop of the IQOQI in Vienna, we built up a telescope platform equipped with a power supply and single-mode fibers leading to the lab. This platform enables us to connect both, a transmitter and a receiver telescope to the setup in the lab and therefore facilitates the realization of new free-space experiments by far. For instance

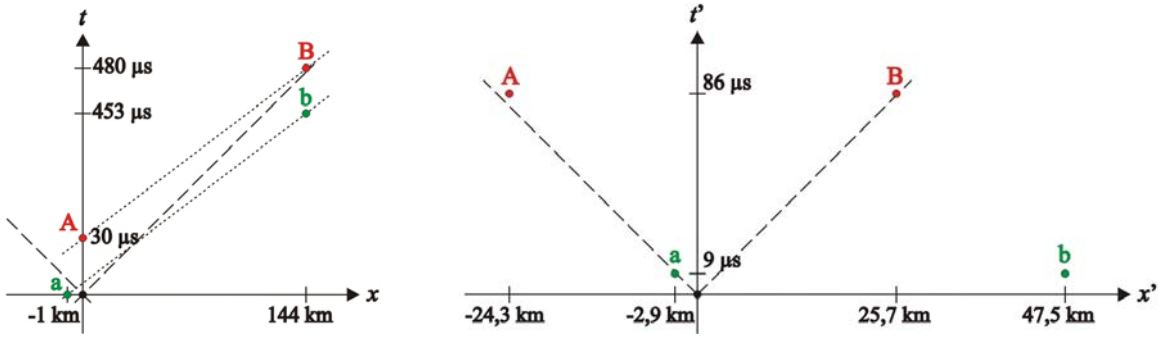

Figure 6.3: (left) The space-time experiment in the rest frame [13] . Alice's (A) and Bob's (B) quantum-random-number generators (a and b respectively) operate outside the source's light cone, ensuring intrinsic random settings for the measured photons.
(right) The space-time experiment observed from within a moving system. Alice's (A) and Bob (B) now simultaneously measure the entangled photon pairs.

[13] Graphs drawn by DI Johannes Kofler.

the feasibility of two-photon interference over a inter-city free-space link could be tested for the implementation of a quantum dense coding protocol.

A Appendix

A.1 Papers

A.1.1 A wavelength-tuneable fiber-coupled source of narrowband entangled photons

The following pages contain a reprint of the *Optics Express* paper "A wavelength-tuneable fiber-coupled source of narrowband entangled photons". It presents the optimized polarization-entangled photon source which is proposed to be implemented in a satellite-based quantum transceiver.

A wavelength-tunable fiber-coupled source of narrowband entangled photons

Alessandro Fedrizzi[1], Thomas Herbst[1], Andreas Poppe[2], Thomas Jennewein[1] and Anton Zeilinger[1,2]

[1]*Institute for Quantum Optics and Quantum Information, Austrian Academy of Sciences, Boltzmanngasse 3, 1090 Wien, Austria*

[2]*Quantum Optics, Quantum Nanophysics and Quantum Information, Faculty of Physics, University of Vienna, Boltzmanngasse 5, 1090 Vienna, Austria*

zeilinger-office@univie.ac.at

Abstract: We demonstrate a wavelength-tunable, fiber-coupled source of polarization-entangled photons with extremely high spectral brightness and quality of entanglement. Using a 25 mm PPKTP crystal inside a polarization Sagnac interferometer we achieve a spectral brightness of 273000 (s mW nm)$^{-1}$, a factor of 28 better than comparable previous sources while state tomography showed the two-photon state to have a tangle of $T = 0.987$. This improvement was achieved by use of a long crystal and careful selection of focusing parameters. We demonstrate that, due to the particular geometry of the setup, the signal and idler wavelengths can be tuned over a wide range without loss of entanglement.

OCIS codes: (270.0270) Quantum Optics; (190.4410) Nonlinear Optics, parametric processes;

References and links

1. A. K. Ekert,"Quantum cryptography based on Bells theorem," Phys. Rev. Lett. **67**, 661-663 (1991).
2. T. Jennewein, C. Simon, G. Weihs, H. Weinurter, and A. Zeilinger,"Quantum cryptography with entangled photons," Phys. Rev. Lett. **84**, 4729-4732 (2000).
3. C. H. Bennett, G. Brassard, C. Crépeau, R. Jozsa, A. Peres, and W. K. Wootters,"Teleporting an unknown quantum state via dual classical and Einstein-Podolsky-Rosen channels," Phys. Rev. Lett. **70**, 1895-1899 (1993).
4. D. Bouwmeester, J. W. Pan, K. Mattle, M. Eibl, H. Weinfurter, and A. Zeilinger,"Experimental quantum teleportation," Nature (London) **390**, 575-579 (1997).
5. E. Knill, R. Laflamme, and G. J. Milburn,"A scheme for efficient quantum computation with linear optics," Nature (London) **409**, 46-52 (2001).
6. P. G. Kwiat, K. Mattle, H. Weinfurter, A. Zeilinger, A. V. Sergienko, and Y. Shih,"New high-intensity source of polarization-entangled photon pairs," Phys. Rev. Lett. **75**, 4337-4341 (1995).
7. M. Pelton, P. Marsden, D. Ljunggren, M. Tengner, A. Karlsson, A. Fragemann, C. Canalias, and F. Laurell,"Bright, single-spatial-mode source of frequency non-degenerate, polarization-entangled photon pairs using periodically poled KTP," Opt. Express **12**, 3573-3580 (2004).
8. F. König, E. J. Mason, F. N. C. Wong, and M. A. Albota,"Efficient and spectrally bright source of polarization-entangled photons," Phys. Rev. A **71**, 33805 (2005).
9. H. Hübel, M. R. Vanner, T. Lederer, B. Blauensteiner, T. Lorünser, A. Poppe, and A. Zeilinger,"High-fidelity transmission of polarization encoded qubits from an entangled source over 100 km of fiber," Opt. Express **15**, 7853-7862 (2007).
10. P. G. Kwiat, P. H. Eberhard, A. M. Steinberg, and R. Y. Chiao,"Proposal for a loophole-free Bell inequality experiment," Phys. Rev. A **49**, 3209-3220 (2004).
11. C. E. Kuklewicz, M. Fiorentino, G. Messin, F. N. C. Wong, and J. H. Shapiro,"High-flux source of polarization-entangled photons from a periodically poled $KTiOPO_4$ parametric down-converter," Phys. Rev. A **69**, 013807 (2004).
12. M. Fiorentino, G. Messin, C. E. Kuklewicz, F. N. C. Wong, and J. H. Shapiro,"Generation of ultrabright tunable polarization entanglement without spatial, spectral, or temporal constraints," Phys. Rev. A **69**, 041801 (2004).

13. B. S. Shi and A. Tomita,"Generation of a pulsed polarization entangled photon pair using a Sagnac interferometer," Phys. Rev. A **69**, 013803 (2004).
14. T. Kim, M. Fiorentino, and F. N. C. Wong,"Phase-stable source of polarization-entangled photons using a polarization Sagnac interferometer," Phys. Rev. A **73**, 012316 (2006).
15. F. N. C. Wong, J. H. Shapiro, and T. Kim,"Efficient generation of polarization-entangled photons in a nonlinear crystal," Laser Physics, **16**, 1517-1524, (2006).
16. J. Fan and A. Migdall,"A broadband high spectral brightness fiber-based two-photon source," Opt. Express **15**, 2915-2920 (2007).
17. C. Liang, K. F. Lee, M. Medic, P. Kumar, R. H. Hadfield, and S. W. Nam,"Characterization of fiber-generated entangled photon pairs with superconducting single-photon detectors," Opt. Express **15**, 1322-1327, (2007).
18. S. M. Spillane, M. Fiorentino, and R. G. Beausoleil,"Spontaneous parametric down conversion in a nanophotonic waveguide," Opt. Express **15**, 8770-8780, (2007).
19. S. Gröblacher, T. Paterek, R. Kaltenbaek, C. Brukner, M. Zukowski, M. Aspelmeyer, and A. Zeilinger,"An experimental test of non-local realism," Nature (London) **446**, 871-875, (2007).
20. T. Paterek, A. Fedrizzi, S. Gröblacher, T. Jennewein, M. Zukowski, M. Aspelmeyer, and A. Zeilinger,"Experimental test of non-local realistic theories without the rotational symmetry assumption," arXiv:0708.0813v1 [quant-ph]
21. K. J. Resch, M. Lindenthal, B. Blauensteiner, H. R. Boehm, A. Fedrizzi, C. Kurtsiefer, A. Poppe, T. Schmitt-Manderbach, M. Taraba, R. Ursin, P. Walther, H. Weier, H. Weinfurter, and A. Zeilinger,"Distributing entanglement and single photons through an intra-city, free-space quantum channel," Opt. Express **13**, 1, 202-209 (2005).
22. C. Z. Peng, T. Yang, X. H. Bao, J. Zhang, X. M. Jin, F. Y. Feng, B. Yang, J. Yang, J. Yin, Q. Zhang, N. Li, B. L. Tian, and J. W. Pan,"Experimental free-space distribution of entangled photon pairs over 13km: towards satellite-based global quantum communication," Phys. Rev. Lett. **94**, 150501 (2005).
23. R. Ursin, F. Tiefenbacher, T. Schmitt-Manderbach, H. Weier, T. Scheidl, M. Lindenthal, B. Blauensteiner, T. Jennewein, J. Perdigues, P. Trojek, B. Ömer, M. Fürst, M. Meyenburg, J. Rarity, Z. Sodnik, C. Barbieri, H. Weinfurter, and A. Zeilinger,"Entanglement-based quantum communication over 144km," Nature Physics **3**, 481-486 (2007).
24. D. N. Matsukevich and A. Kuzmich,"Quantum state transfer between matter and light," Science **306**, 663-666 (2004).
25. B. Julsgaard, J. Sherson, I. Cirac, J. Fiurasek, and E. S. Polzik,"Experimental demonstration of quantum memory for light," Nature (London) **432**, 482-486 (2004).
26. C. Kurtsiefer, M. Oberparleitner, and H. Weinfurter, "High-efficiency entangled photon pair collection in type-II parametric fluorescence," Phys. Rev. A **64**, 023802 (2001).
27. F. A. Bovino, P. Varisco, M. A. Colla, G. Castagnoli, G. Di Giuseppe, and A. V. Sergienko, "Effective fiber-coupling of entangled photons for quantum communication," Opt. Commun. **227**, 343-348 (2003).
28. D. Ljunggren and M. Tengner, "Optimal focusing for maximal collection of entangled narrow-band photon pairs into single-mode fibers," Phys. Rev. A **72**, 062301 (2005).
29. M. H. Rubin, D. N. Klyshko, Y. H. Shi, and A. V. Sergienko,"Theory of two-photon entanglement in Type-II optical parametric down-conversion," Phys. Rev. A **50**, 5122-5233 (1994).
30. D. F. V. James, P. G. Kwiat, W. J. Munro, and A. G. White,"Measurement of qubits," Phys. Rev. A **64**, 052312 (2001).
31. V. Coffman, J. Kundu, and W. K. Wootters,"Distributed entanglement," Phys. Rev. A **61**, 052306 (2000).
32. K. Kato and E. Takaoka,"Sellmeier and thermo-optic formulas for KTP," Appl. Opt. **41**, 50405044 (2002).
33. S. Emanueli and A. Arie,"Temperature-dependent dispersion equations for KTiOPO4 and KTiOAsO4," Appl. Opt. **42**, 6661-6665, (2003).
34. M. Fiorentino, C. E. Kuklewicz, and F. Wong,"Source of polarization entanglement in a single periodically poled $KTiOPO_4$ crystal with overlapping emission cones," Opt. Express **13**, 1, 127-135 (2005).

1. Introduction

Sources for photonic entanglement form an integral part of quantum optics experiments and quantum information protocols like quantum key distribution [1,2], quantum teleportation [3,4] and quantum computing [5]. To date the most successful method of creating polarization entangled photon pairs is spontaneous parametric downconversion (SPDC) in nonlinear crystals. In the first practical and efficient scheme, orthogonally polarized photon pairs were created in a Type-II BBO bulk crystal and emitted along intersecting cones [6]. Since then nonlinear optics has advanced; Periodic poling of nonlinear crystals considerably relaxes the phasematching conditions for SPDC and allows to fully exploit the material's nonlinear properties. These crys-

tals are best employed in collinear configuration, where a much bigger fraction of the created photons can be entangled than in the conelike geometry of [6], thus leading to downconversion sources of higher spectral brightness. This increase comes at the cost of a new problem though, the need to spatially separate the collinear downconversion modes.

When the downconverted photons are created at substantially different wavelengths, they can be separated by dichroic mirrors, and several demonstrations of this have reported high spectral brightness [7–9]. For many applications, however, wavelength-degenerate photons are preferable. The first attempt to build a source based on periodically poled $KTiOPO_4$ (PPKTP) and collinear beam propagation used a simple beamsplitter to separate the output modes, at the cost of an unwanted 50% loss in the coincidences [11]. A more effective method, originally proposed in [10], is to interferometrically combine the outputs of two downconverters on a polarizing beamsplitter. The authors of [12] implemented this idea, using one bidirectionally pumped PPKTP crystal in a folded Mach-Zehnder interferometer. The spectral brightness of this source reached 4000 pairs(s mW nm)$^{-1}$, but the Mach-Zehnder interferometer was sensitive to vibrations and even with active phase stabilization the visibility of the setup was limited to 90%. To avoid the need to actively stabilize their setup, the authors of [13] combined the downconversion pairs created in a type-I BBO crystal on a symmetric beamsplitter in a intrinsically phase-stable Sagnac interferometer. This configuration proved to be stable, but the achieved count rates and visibilities did not come close to the configurations realized before. Finally, in a recently published work Kim et al. [14] ingeniously combined the advantageous features of [12] and [13], bidirectionally pumping a type-II PPKTP crystal in a polarization Sagnac interferometer. The authors reported a detected photon-pair yield of 5000 (s mW nm)$^{-1}$ at a 96.8% visibility. In an update [15], these numbers were significantly improved to 9800 (s mW nm)$^{-1}$ at 98% visibility.

During this time, there has also been significant improvement in the development of correlated photon-pair sources based on four-wave mixing in single-mode fibers [16, 17] and SPDC in nonlinear crystal waveguides [18]. The strong spatial confinement of the pump beam in nonlinear waveguides leads to higher effective material nonlinearities and thus the generation of photon pairs of much higher spectral brightness than in bulk periodically poled crystals. Yet, to date no high quality polarization entanglement has been demonstrated in these schemes.

In this paper we demonstrate a fiber-coupled source of polarization-entangled photons, based upon the scheme by Kim et al. [14]. We show that the wavelength of the downconversion photons can be tuned without loss of visibility over a range of $\pm$26 nm around degeneracy merely by changing the temperature of the nonlinear crystal. Wavelength tunability of entangled photons has been claimed before [8, 9] but was not demonstrated to the extent achieved here. The high purity of the entangled photon state in our setup enables further tests on fundamental concepts of physics for example on the violation of local or non-local realism [19, 20], which place increasingly stringent lower bounds on the required degree of entanglement. The high spectral brightness of the source makes it perfectly suitable for free-space quantum communication experiments [21–23]. Given that the range of wavelengths accessible to this source covers important atomic transitions in rubidium or caesium, it is also a promising candidate for atom-photon coupling experiments, e.g. photonic memories for quantum repeaters [24, 25].

The paper is organized as follows: in section 2 we briefly review spontaneous parametric downconversion in periodically poled crystals. In section 3 we discuss the influence of the crystal length on the performance of a downconversion setup as well as the optimal focusing conditions for type-II PPKTP crystals of varying length. In section 4 we describe the source of polarization-entangled photons and in section 5 we present our results on obtained spectral brightness, quality of entanglement and wavelength tunability.

2. Downconversion in periodically poled crystals

Parametric downconversion in a nonlinear crystal can be described by the spontaneous splitting of a pump photon (p) into a pair of photons (usually called *signal s* and *idler i*) according to conservation of photon energy $\omega_p = \omega_s + \omega_i$ and momentum. In periodically poled crystals, the effective nonlinearity of the medium is periodically inverted by the application of an electric field with alternating directions during the crystal fabrication process. In contrast to birefringent phasematching in bulk crystals the quasi-phasematching conditions now involve an additional term which depends on the crystal-poling period Λ:

$$\mathbf{k}_p(\lambda_p, n_p(\lambda_p, T)) = \mathbf{k}_s(\lambda_s, n_s(\lambda_s, T)) + \mathbf{k}_i(\lambda_i, n_i(\lambda_i, T)) + \frac{2\pi}{\Lambda(T)} \tag{1}$$

where $\mathbf{k}_{p,s,i}$ are the wavevectors of the pump, signal and idler photons, and $n_{p,s,i}$ the wavelength and temperature-dependent refractive indices of the crystal for the respective wave fields. Assuming a fixed pump wavelength, Eq. 1 shows that the $\mathbf{k}$ vectors of the signal and idler photons are temperature dependent, in particular, for a fixed emission angle, wavelength-degenerate photons will only be created at one certain temperature T . Quasi-phasematching in periodically poled crystals allows for almost arbitrary phasematching angles and wavelengths in comparison to the nontrivial conditions in bulk nonlinear crystals, where only birefringent and angle phasematching is possible. In particular, periodically poled crystals can be tailored such that $\mathbf{k}_{p,s,i}$ are parallel to one of the crystallographic axes X, Y or Z. For a type-II SPDC process this means that the orthogonal signal and idler beams do not experience transversal walkoff, an effect which severely limits the maximum useful length of birefringent nonlinear crystals to less than 10 mm in typical downconversion setups. In section 3 we compare photon-pair yields coupled to single-mode optical fibers and the corresponding single-photon bandwidths of downconversion photons created in periodically poled crystals of various lengths. Furthermore we find the optimal focusing conditions for each crystal resulting in unprecedented photon yields.

3. Optimization of beam focusing and crystal properties

In downconversion experiments it is well known that focusing the pump beam drastically improves count rates and collection efficiencies into single-mode fibers. The quest for the optimal focusing parameters has been the subject of theoretical and experimental investigations [26–28]. We followed the lines of Ljunggren et al. [28], who numerically calculated optimal focusing conditions for downconversion in PPKTP crystals and made predictions for the expected dependence of count rates and photon bandwidths on crystal length. The two key parameters for an entangled photon source which can be maximized via optimal focusing are the detected coincidence rate R_c and the coincidence-to-single-photon coupling ratio $\eta_c = R_c/\sqrt{R_i R_s}$, with R_i and R_s being the single photon count rates. As pointed out in [28] the focusing conditions for these parameters are not generally the same, as the number of single photons and photon pairs coupled into fibers do not solely depend on the total number of pairs created but also on the mode quality factor M^2 of the downconversion and its overlap with the fiber modes.

Here, instead of measuring M^2 factors as done in [28] we directly compared single photon and coincidence count rates for four ($L = 10, 15, 20, 25$ mm) X-cut flux-grown PPKTP crystals manufactured by *Raicol*. The crystals had a grating period of 10 μm and were quasi-phasematched for collinear degenerate downconversion at $\lambda_p = 405$ nm and $49.2\,^\circ C$. The 405 nm laser diode used in our setup had limited power, therefore we chose to find the optimal focusing conditions for a maximal coincidence rate $R_{c\,\max}$.

We pumped a given crystal of length L with spot waist sizes w_p from $15-55\ \mu m$, coupling the downconversion into a single mode fiber attached to a fiber beamsplitter and two detectors. For each w_p we varied mode waist sizes $w_{s,i}$ between $(15\mu m < w_{s,i} < 55\mu m)$ continuously monitoring single and coincidence count rates. The obtained data, exemplary shown for the $L = 15$ mm crystal in figures 1(a) and (b), was numerically fitted with polynomial functions. From these fits, for each w_p we obtained one optimal $w_{s,i\ \mathrm{opt}}$ and, in consequence one optimal set $(w_p, w_{s,i})_{\mathrm{opt}}$ for each crystal length L.

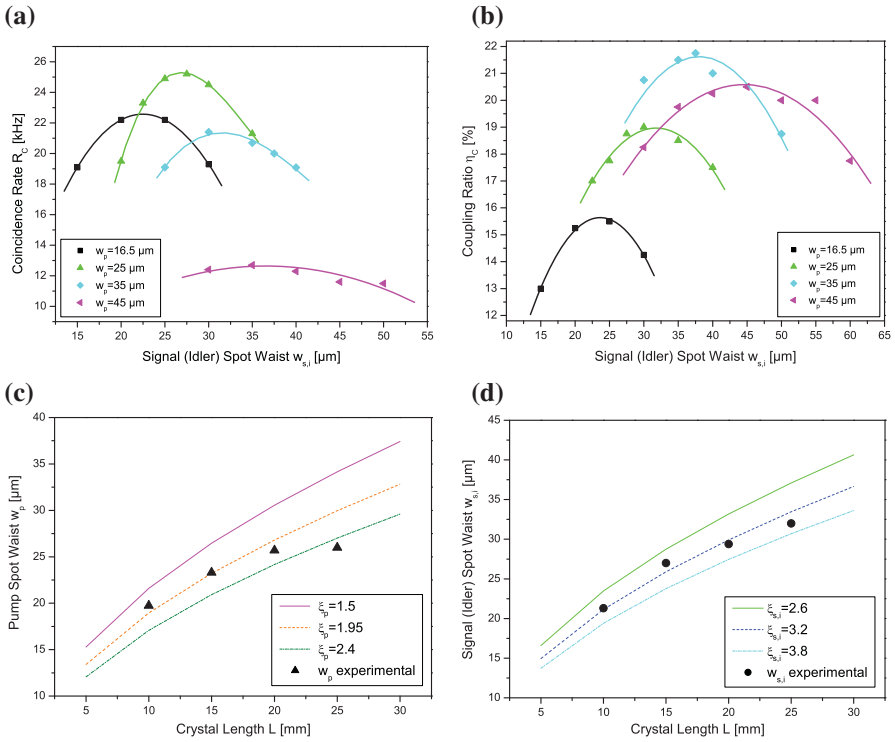

Fig. 1. Measured coincidence count rates R_c (a) and coupling ratios η_c (b) for a $L = 15$ mm crystal for a series of focusing conditions. From these measurements we determined pump (c) and signal (idler) (d) spot waist sizes w_p and $w_{s,i}$ for maximal photon-pair count rate $R_{c\ \mathrm{max}}$ and crystals of length $10, 15, 20$ and 25 mm. The detected count rates were repeatable to within 5%. The lines drawn for three constant values of the dimensionless parameters ξ_p and $\xi_{s,i}$ ($\xi = L/z_r$, where z_r is the Rayleigh range) show the supposed independence of $\xi_{p\ \mathrm{opt}}$ and $\xi_{s,i\ \mathrm{opt}}$ of L. While this behavior is certainly given for $\xi_{s,i\ \mathrm{opt}}$ (black dots), it was not observed for $\xi_{p\ \mathrm{opt}}$. (black triangles).

The results in Fig. 1 (c) and (d) show the spot waist sizes for maximal photon-pair yield for the pump beam and the signal (idler) modes for different crystal lengths. For crystals from $10-25$ mm the optimal focusing conditions for $R_{c\ \mathrm{max}}$ are $(20\mu m \lesssim w_{p\ \mathrm{opt}} \lesssim 26\mu m)$ (Fig. 1(c)) and $(21\mu m \lesssim w_{s,i\ \mathrm{opt}} \lesssim 32\mu m)$ (Fig. 1(d)). Using the dimensionless parameters $\xi_p = L/z_{r\ p}$ and $\xi_{s,i} = L/z_{r\ s,i}$, where $z_{r\ p,s,i}$ are the Rayleigh ranges of the pump and the signal (idler) modes in the crystal, this corresponds to $(1.8 \lesssim \xi_{p\ \mathrm{opt}} \lesssim 2.6)$ and $\xi_{s,i\ \mathrm{opt}} \sim 3.2$. We found that for the signal and idler modes the focusing parameter $\xi_{s,i\ \mathrm{opt}}$ is independent of L (cf. [28]), but that the pump focus parameter $\xi_{p\ \mathrm{opt}}$ rises with L, which might be due to increasing contribution of

grating defects in longer crystals.

For the $L = 15$ mm crystal we could also deduce the focusing conditions for a maximal coincidence-to-single-photon coupling ratio $\eta_{c\,\max} = max\ \eta_c(\xi_p, \xi_{s,i})$. The parameters ξ_p and $\xi_{s,i}$ differ significantly from those for $R_{c\,\max}$ with $\xi_p \sim 0.7$ and $\xi_{s,i} \sim 1.5$. The reason is presumably that for tighter confinement of the pump field within the crystal, a higher total of pairs is generated, which results in a higher R_c. Due to the stronger focusing these pairs will however be created in an increasingly higher order spatial longitudinal multimode (cf. [28]) which leads to a decreasing overlap between the coupling fiber modes and the downconversion mode and hence to a lower coupling ratio η_c.

Consider the properties of the power spectrum of the emitted two-photon state, obtained by using first-order perturbation theory [29]:

$$I \propto sinc^2(\frac{L}{2}\Delta k) \tag{2}$$

where Δk is the phase mismatch, $k_p - k_i - k_s - \frac{2\pi}{\Lambda}$. The authors of [28] conclude that the flux of

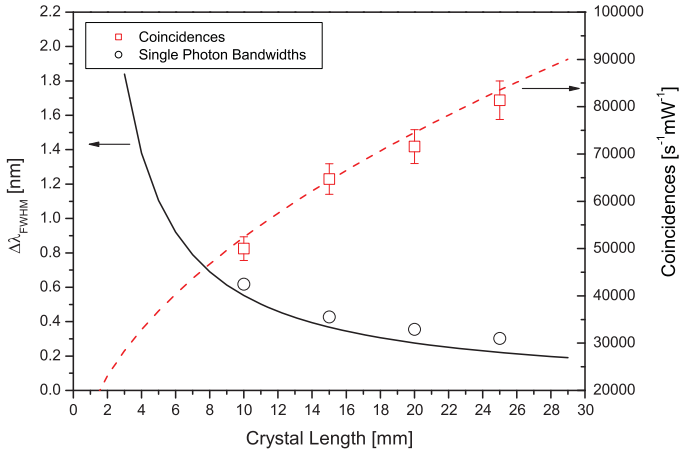

Fig. 2. Measured spectral bandwidths (FWHM) of downconversion photons and photon-pair yields for PPKTP crystals of various lengths. The single photon bandwidth (black circles) was determined via interference in a single photon Michelson interferometer and is shown compared to theoretic values calculated using Eq. 4 (black line). The measured coincidence rates (red squares) show the expected square root dependence on L (Eq. 3).

downconversion photons R_c coupled into single-mode optical fibers in collinear configurations with optimal focusing relates to the crystal length L as

$$R_c \sim \sqrt{L}. \tag{3}$$

The $sinc^2$ function in Eq. 2 drops to a value of 0.5 for $\frac{L}{2}\Delta k = 1.39$. By writing Δk as a function of λ_i, expanding Δk in a Taylor series around $\lambda_i = 810$ nm and neglecting higher order terms, we arrive at an expression for the single-mode bandwidths of the signal and idler photons:

$$\Delta\lambda_{s,iFWHM} = \frac{5.52x10^{-3}}{L}\ \text{nm} \tag{4}$$

The spectral brightness B of the produced downconversion light, a value for the comparison of different downconversion setups, given by the number of produced photon pairs per second, per milliwatt of pump power and per nm bandwidth, therefore scales as $B \sim L\sqrt{L}$.

The experimental results on the photon-pair yield R_c and the bandwidth $\Delta\lambda_{s,i}$ of the down-converted photons for different crystal lengths are shown in Fig. 2. The maximum photon-pair yields R_c resulted from the evaluation of the optimal focusing conditions. A least-square fit of the corresponding data points to expression 3 yielded $R_c(L) = 16220 \times \sqrt{L}$ pairs $s^{-1}mm^{1/2}$ with excellent agreement to the square root dependence on L. The photon bandwidths $\Delta\lambda_{s,i}$ were determined with a single-photon Michelson interferometer and in Fig. 2 directly compared to the single mode bandwidths predicted by theory (eq. 4).

4. Entangled Photon Source Setup

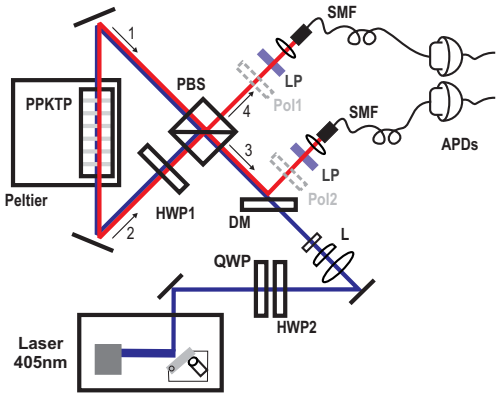

Fig. 3. Scheme of the fiber-coupled entangled photon source. A 405nm *Littrow* diode laser whose polarization and phase are set by a quarter- (QWP) and a half-wave plate (HWP2) is focussed via a combination of one spherical and two cylindrical lenses (L) into a PPKTP crystal inside a polarization Sagnac loop built up by dual-wavelength polarizing beamsplitter (PBS) a dual-wavelength half-wave plate (HWP1) (anti-reflection coated for 405 and 810 nm) and two laser mirrors. The downconversion modes are coupled into single mode fibers (SMF). Remaining stray laser light is blocked by two RG715 longpass color glass filters (LP). Polarizers (Pol1, Pol2) can be inserted to characterize the produced photon pairs.

Once we had found the optimal focusing conditions for the PPKTP crystals and ascertained that the use of long crystals indeed yielded more photon pairs and narrower bandwidth the entangled photon source was set up. The source is pumped by a *Toptica* 405 nm grating-stabilized laser diode, focussed to a circular spot of waist $w_o = 27\ \mu m$ at the center of the crystal. The polarization state of the laser beam is controlled by a combination of a halfwave- (HWP2) and a quarter-wave plate (QWP).The 25 mm PPKTP crystal is mounted in a crystal oven, at the center of a polarization Sagnac interferometer (PSI) which consists of a dual wavelength polarizing beamsplitter cube (PBS), a dual wavelength half-wave plate (HWP1) oriented at $\frac{\pi}{4}$ and two laser mirrors (see Fig. 3). The vertical component of the laser beam is reflected at the PBS and rotated to horizontal orientation by HWP1. It creates pairs of photons with orthogonal polarizations $|H_s\rangle_1$ and $|V_i\rangle_1$, the number subscripts denoting the spatial mode of the photons, which propagate in clockwise direction. The horizontal component of the beam is transmitted at the PBS and likewise creates pairs $|H_s\rangle_2$ and $|V_i\rangle_2$ propagating in counterclockwise direction. At HWP1, $|H_s\rangle_2$ and $|V_i\rangle_2$ are rotated by $\frac{\pi}{2}$ into $|V_s\rangle_2$ and $|H_i\rangle_2$. The counterpropagating pairs in modes 1 and 2 are then combined at the PBS, where again horizontal photons are transmitted and vertical photons reflected such that $|H_s\rangle_1, |V_i\rangle_1 \rightarrow |H_s\rangle_3, |V_i\rangle_4$ and $|V_s\rangle_2, |H_i\rangle_2 \rightarrow |V_s\rangle_3, |H_i\rangle_4$. The two-photon state emerging in modes 3 and 4 is thus $|H_s\rangle_3 |V_i\rangle_4 + e^{i\phi} |V_s\rangle_3 |H_i\rangle_4$. The phase ϕ

is set via appropriate adjustment of HWP2 and QWP [14]. Output mode 3 is identical to the pump input mode, therefore the downconversion photons have to be separated from the pump by a dichroic mirror (DM). Subsequently, the photons in modes 3 and 4 are coupled into single mode optical fibers whose waists are matched via $f = 18.4$mm aspheric lenses to the pump waist in the crystal according to the focus parameters given in section 3.

Note that, due to birefringence, orthogonally polarized photons in the crystal travel at different group velocities, causing the $|H\rangle$ photon to leave the crystal before the $|V\rangle$ photon. This longitudinal walkoff renders the photons partly distinguishable and leads to a decrease in the degree of entanglement. This effect, which is inherent to all Type-II downconversion schemes, is compensated by flipping the two photons in the counterclockwise arm of the PSI by $\frac{\pi}{2}$. The longitudinal walkoff of pair 2 is inverted with respect to pair 1 and while there is still always a non-zero delay between $|H\rangle$ and $|V\rangle$ photons in modes 3 and 4, the arrival time of the photons contains no information about the respective photon polarization anymore. The efficiency of this compensation scheme depends only on the precision and orientation of HWP1 and is thus more effective than in other schemes.

5. Entangled photon source performance and tunability

The use of a 25 mm long PPKTP crystal in the perfectly compensated PSI scheme and the optimum choice of focus parameters results in unprecedented photon yields and spectral brightness and a very high degree of entanglement. Using a *PerkinElmer* SPCM-AQ4C single photon detector array with a quantum efficiency of $\sim 40\%$ and a home-built FPGA coincidence counter with a coincidence time window of 4.4 ns, we detected 82000 photon pairs/s at 1 mW of pump power.

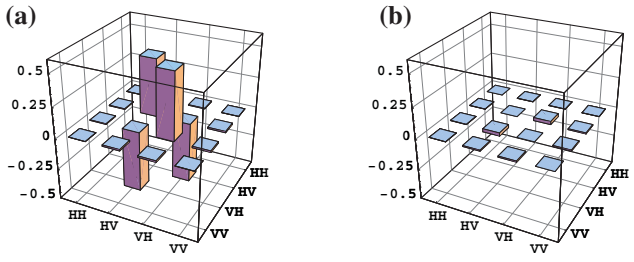

Fig. 4. (color online) Tomography of the two-photon quantum state. The real (a) and imaginary (b) part of the density matrix was reconstructed from 36 linearly independent coincidence measurements. The resulting fidelity F to the $\left|\psi^-\right\rangle$ state was $F = 0.9959 \pm 0.0001$ and the Tangle $T = 0.9875 \pm 0.0003$. Within the resolution of this representation the experimental graph is in excellent agreement to the theoretic expectation.

The detected coincidence-to-single-photon ratio η_c was 28.5%. The overall loss of the optical components in the setup including the single-mode fibers, which were not AR-coated, and the $100:1$ extinction ratio of the PBS, add up to a total of 15.4% averaged over the optical paths for output mode 3 and 4. Taking into account the 40% detector efficiency, the maximal achievable coupling ratio is 33.8%, which in turn shows that in our setup the mode overlap, the probability that one photon of a pair is collected, given that its partner photon is in its respective collection mode, is 84.4%. When set to the optimal focusing conditions for $\eta_{c\,\max}$, the photon pair yield of the source decreases by 20% to 65000 pairs/s while the mode overlap increases to 95%, to our knowledge the highest value reported so far.

The photons have a measured $FWHM$ bandwidth of 0.3 nm (see Fig. 2), the spectral brightness of the source is therefore 273000 pairs (s mW nm)$^{-1}$. The visibility of the two-photon quantum state measured for degenerate photons ($\lambda_{s,i} = 810$ nm) in the $|\pm\rangle = \frac{1}{\sqrt{2}}(|H\rangle \pm |V\rangle)$ basis was 99.5%. The produced entangled state was further characterized using full quantum state tomography [30]. The fidelity $F = \langle\psi^-|\,\rho\,|\psi^-\rangle$ of the two-photon density matrix ρ with the maximally entangled state $|\psi^-\rangle = \frac{1}{\sqrt{2}}(|H\rangle|V\rangle - |V\rangle|H\rangle)$ was $F = 0.9959 \pm 0.0001$ and the tangle, a measure for the degree of entanglement as defined in [31] was $T = 0.9875 \pm 0.0003$. The measurements for visibility and quantum state tomography were performed at 0.25 mW of pump power and averaged over 10 seconds. The statistical standard deviations of these results were estimated by performing a 100 run Monte Carlo simulation of the state tomography analysis, with Poissonian noise added to the count statistics in each run [30]. Figure 4 shows the reconstructed real and imaginary parts of the density matrix ρ of the produced states. After subtraction of accidental coincidences caused by detector darkcounts, fidelity and tangle increase to $F = 0.9978 \pm 0.0001$ and $T = 0.9940 \pm 0.0001$, respectively. The state is thus very close to a pure entangled state. Indeed in the H/V basis we measured polarization contrasts of up to 9500:1 (accidentals subtracted), a regime where visibility measurements are limited by the extinction ratio of the polarizers, which was found to be $10000:1$. The exact crystal temperature for wavelength degeneracy, 49.2 $^\circ C$, was calculated from theory via Eq. 1. We experimentally confirmed this temperature with a single-photon spectrometer, measuring λ_i and λ_s for temperatures from 25 $^\circ C$ to 60 $^\circ C$ (see Fig. 5).

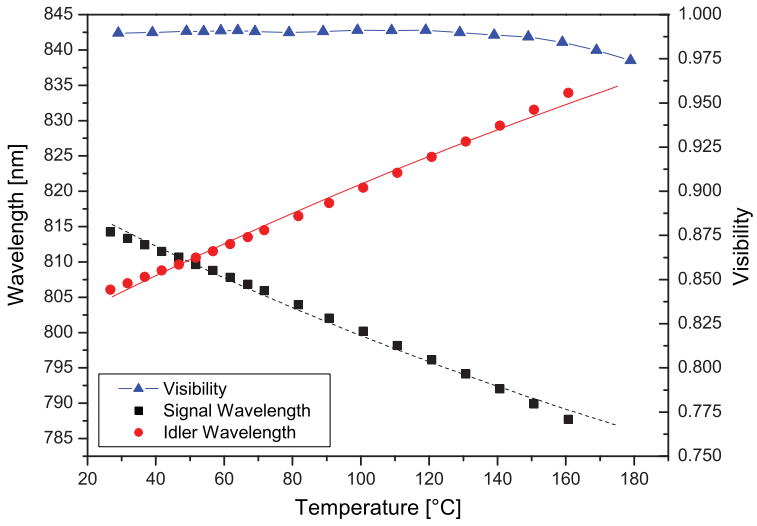

Fig. 5. Signal (black rectangles) and idler (red circles) wavelengths and 2-photon visibility (blue triangles) as a function of crystal temperature. The wavelengths were measured with a scanning single photon spectrometer with a resolution of 0.2 nm. Our crystal oven allows us to reach a wavelength spacing of more than 50 nm.

The most striking feature of the setup is that the visibility of the entangled state stays above 99% in a large wavelength range (Fig. 5). It starts to decrease slightly for wavelength shifts of more than ± 18 nm, reaching 97.5% at 810 ± 26 nm at $\sim 180\,^\circ C$. The most likely cause for this decrease is that all optical components in the setup were specified and coated for 810 nm and act as partial polarizers at substantially higher or lower wavelengths.

The refractive indices needed to calculate theoretical values for λ_i and λ_s, according to Eq.

1, were obtained via the Sellmeier and temperature-dependent Sellmeier equations for KTP from [32] and [33]. The thermal expansion coefficient for KTP which affects the crystal poling period Λ also stems from [33]. Note that these equations are of an empirical nature and do not exactly reproduce the actual refractive indices for the whole spectral and temperature range. In particular, the temperature-dependent extensions for the Sellmeier equations from [33] do not extend to wavelengths lower than 532 nm. In order to reproduce the crystal temperature for degenerate downconversion and to obtain an accurate wavelength fit over the whole temperature range, we had to adopt $\partial n_y/\partial t\,|_{405nm} = 28 \times 10^{-6}$, reported in [34].

6. Conclusion

We have demonstrated a fiber-coupled, wavelength-tunable source of narrowband, polarization-entangled photons. By comprehensive optimization of focusing conditions and the use of a 25 mm long crystal, we achieved a spectral brightness of 273000 (s mW nm)$^{-1}$, a factor of 28 higher than comparable previous setups. The entangled state has a tangle $T = 0.987$ and the coincidence-to-single-photon coupling ratio is 28.5%. We demonstrated wavelength tuning of entangled photons in a range of $\pm$26 nm around degeneracy with virtually no decrease in entanglement. These properties, combined with the intrinsic phase stability of the Sagnac-type setup, the compactness, and the ease of use, make this setup a perfect tool for quantum communication experiments both in the laboratory and in the field.

Acknowledgements

Thanks are due to Hannes Huebel for valuable help in starting up the project, to Bibiane Blauensteiner for the single photon spectrometer and to Robert Prevedel and Nathan Langford for helpful discussions. We acknowledge support by the Austrian Science Foundation (FWF), project number SFB1520, the Austrian Space Agency within the ASAP program, the EC funded program QAP, the DTO-funded U.S. Army Research Office and the City of Vienna.

A.1.2 Testing quantum communication with photonic Bell states over a 71dB loss free-space channel

A preprint of the paper "Testing quantum communication with photonic Bell states over a 71dB loss free-space channel" is provided in the following pages. The paper reports on the successful transmission of Bell states over the 144km free-space link and was submitted to *Nature Physics*.

Testing quantum communication with photonic Bell states over a 71 dB loss free-space channel

Alessandro Fedrizzi,[1] Rupert Ursin,[1] Thomas Herbst,[1] Matteo Nespoli,[1] Robert Prevedel,[1,2]
Thomas Scheidl,[1] Felix Tiefenbacher,[1] Thomas Jennewein,[1] and Anton Zeilinger[1,2]

[1]*Institute for Quantum Optics and Quantum Information, Austrian Academy of Sciences, Boltzmanngasse 3, 1090 Wien, Austria*
[2]*Quantum Optics, Quantum Nanophysics and Quantum Information, Faculty of Physics, University of Vienna, Boltzmanngasse 5, 1090 Vienna, Austria*

(Dated: April 1, 2008)

Quantum communication enables tasks not possible in classical communication scenarios [1]. Many quantum communication protocols require the distribution of entangled states between distant parties. Here we experimentally demonstrate the successful transmission of entangled photon states over a 144 km free-space link. We emulate quantum key distribution over two independent transmitter modes with a total channel loss of 71.2 dB, a regime which corresponds to a two-link satellite quantum communication scenario and surpasses the maximum channel loss accessible to state-of-the-art quantum cryptography schemes relying on weak coherent laser pulses [2] by 30 dB. We show that the received entangled states have an excellent, noise-limited fidelity, even though they are subject to extreme attenuation and turbulent atmospheric fluctuations. This is a compelling argument for entanglement based quantum communication on a global scale and an important step towards the realization of two-photon quantum communication protocols [3] like teleportation, purification and dense coding in free-space.

Introduction - Entangled photonic qubits are ideal quantum information carriers because they can be easily generated, manipulated and transmitted over large distances via optical fibres or free-space links. The maximal transmission distance in optical fibres, which are widely used in classical communication, is limited to the order [2, 4] of ∼100 km and quantum repeaters [5], which might help overcome this limit, are still an elusive technology and far from being implemented in the real world. In view of these problems, the most promising option for global quantum communication is free-space transmission using satellites [6]. Since the first demonstration of free-space quantum communication with entangled photons in an outdoor environment [7], distances have quickly increased from initially 600 m to a ∼10 km scale [8–10]. Ultimately, a 144 km free-space link was set up between two Canary Islands with a receiver telescope originally built for laser communication with satellites [11, 12]. There, via the transmission of individual entangled photons, entanglement-based [11] and decoy-state quantum key distribution [12] (QKD) has already been demonstrated.

The present work constitutes a major technological and fundamental milestone on the road to global quantum communication. From the fundamental perspective, in contrast to earlier results in entanglement-based quantum communication experiments on the ∼100 km scale [4, 11], we transmit both photons of entangled pairs via two independent spatial modes to a common receiver, and show that entanglement was preserved by violation of a Clauser-Horne-Shimony-Holt (CHSH) Bell inequality [13]. From the technological perspective, our system overcomes a channel loss which is 1000 times higher than the limit of 40 dB for realistic decoy state QKD devices as revealed in a recent analysis [14] of the experiment in ref. [2]. The achieved noise-limited fidelity proves the feasibility of quantum communication protocols requiring the transmission of two photons, e.g. quantum dense coding, entanglement purification, quantum teleportation [3] and quantum key distribution without a shared reference frame [15] over a free-space channel. In addition, the photon pair flight time of ∼0.5 ms is the longest lifetime of photonic Bell states reported so far, almost 4 times longer than the previous high of ∼ 125 μs [16].

Experiment - The experiment was conducted between La Palma and Tenerife, two Canary Islands situated in the Atlantic Ocean off the West African coast.

An overview of the experimental scheme is shown in figure 1. At the transmitter station at La Palma, photon pairs were generated in a 10mm long, periodically poled $KTiOPO_4$ crystal which was bidirectionally pumped by a 405 nm diode laser. The photon pairs with a wavelength of 810 nm and a bandwidth (FWHM) of 0.6 nm were coherently combined in a polarization Sagnac interferometer (see ref. [17] for details) and emitted in the maximally entangled state:

$$|\psi\rangle = \frac{1}{\sqrt{2}}\left(|HV\rangle + e^{i\phi}\,|VH\rangle\right) \tag{1}$$

At 20 mW of pump power, the source produced ∼10^7 photon pairs/s of which ∼10^6 pairs/s and ∼ 3.3×10^6 single photons/s were locally detected. The photon pairs were coupled into single-mode fibres with a length difference of 10

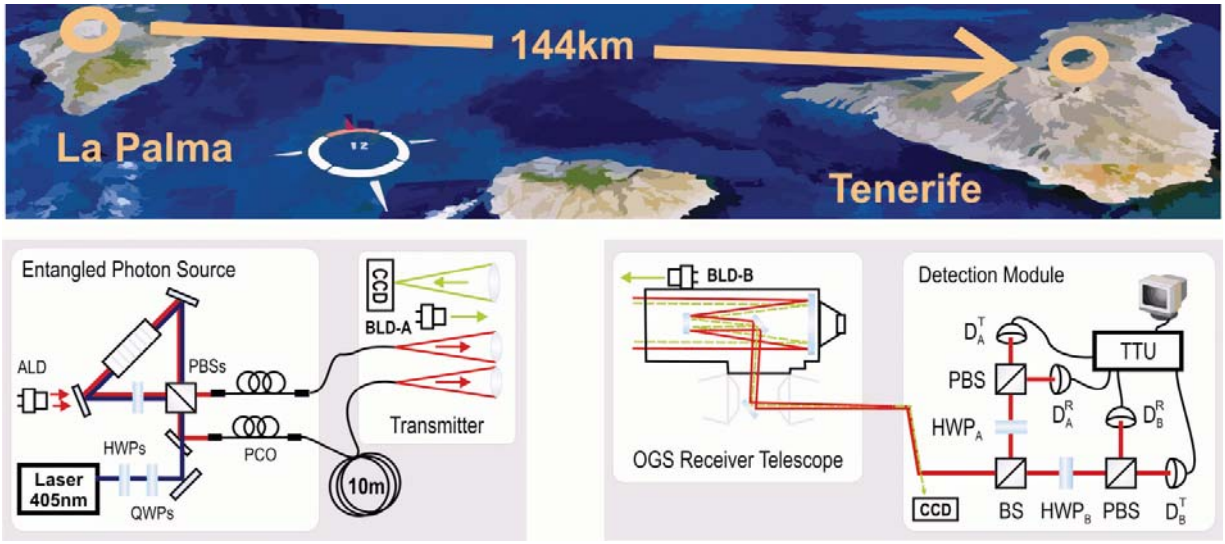

FIG. 1: Satellite image (NASA World Wind) of the Canary Islands of Tenerife and La Palma and overview of the experimental scheme. At La Palma, a Sagnac down-conversion source [17] creates narrow-band entangled photon pairs. Manual polarization controllers (PCO) and an auxiliary laser diode (ALD) are used for polarization alignment. The photon pairs are transmitted via a pair of telescopes mounted on a rotatable platform to the 144 km distant receiver (OGS) on Tenerife. The transmitter telescope platform is actively locked to a 532 nm beacon laser diode (BLD-B) attached to the OGS. Likewise, the OGS receiver telescope tracks the virtual position of a 532 nm beacon laser attached to the transmitter (BLD-A). At the OGS, the overlapping photon beams are collected and guided to the detection module by a system of mirrors. This module consists of a 50/50 beamsplitter cube (BS), two half-wave plates ($\mathrm{HWP_A}$, $\mathrm{HWP_B}$) two polarizing beamsplitter cubes (PBS) and four single-photon silicon avalanche photo diodes ($\mathrm{D_A^T}$, $\mathrm{D_A^R}$, $\mathrm{D_B^T}$, $\mathrm{D_B^R}$), where the subscript denotes the polarization analyzer (A,B) as defined by halfwave plate (A,B) and a PBS and the superscript the respective detector (R,T) in either analyzer.

m which introduced a time delay of $\Delta t = 50$ ns between the two photons. Both fibres were equipped with manual polarization controllers to compensate for the polarization rotation they induced. The fibres were connected to two transmitter telescopes which consisted of a single-mode fibre coupler and a f/4 best form lens (f=280 mm) and were mounted on a joint rotatable platform. A bidirectional closed-loop tracking mechanism [12] (figure 1) compensated for spatial drifts of the optical path through the time-dependent atmosphere. Compared to ref. [11], where only the transmitter telescope was able to automatically track the receiver, this greatly enhanced the long-term stability of the optical link.

At the receiver, the incoming photons were collected by the 1 m mirror (effective focal length f=38 m) of the European Space Agency's Optical Ground Station (OGS), located on Tenerife. To ensure that turbulence induced beam wander did not divert the beam off the detectors, the photons were collimated (f = 400 mm) before they were guided to a polarization analysis module. Here, a symmetric beam splitter (BS) directed impinging photons randomly to one of two polarization analyzers (A, B), each consisting of a half-wave plate ($\mathrm{HWP_A}$, $\mathrm{HWP_B}$), mounted in a motorized rotation stage, and a polarizing beam splitter (PBS). The polarized light was then refocused (f=50mm) onto four single-photon avalanche diodes (SPADs). Each click of the SPADs was recorded by a time-stamping unit (156 ps resolution) which encoded and stored the arrival time and channel number of events. Figure 2a shows the cross-correlations of these time-stamps for two exemplary measurements. One can clearly identify the two coincidence peaks at ± 50 ns around zero delay, which corresponds to the fibre delay Δt introduced at the transmitter. The average width (FWHM) of the coincidence peaks was 560 ps. To obtain the number of coincident photons, we summed up the number of correlations in a time window of 1.25 ns centred at the coincidence peak positions (figure 2b).

As a witness for the presence of entanglement between the received photons, we chose a CHSH Bell inequality [13]:

$$S(\alpha, \beta, \alpha', \beta') = |E(\alpha, \beta) - E(\alpha, \beta')| + |E(\alpha', \beta) + E(\alpha', \beta')| < 2, \tag{2}$$

where $E(\theta_A, \theta_B) = (C_{TT}(\theta_A, \theta_B) + C_{RR}(\theta_A, \theta_B) - C_{TR}(\theta_A, \theta_B) - C_{RT}(\theta_A, \theta_B))/N$ is the normalized correlation value of polarization measurement results on photon pairs. $C_{ab}(\theta_A, \theta_B)$ is the number of coincidences measured between detectors at the (T/R) output ports (figure 1) of the polarization analysers A and B set to angles (θ_A, θ_B) and N is the sum of these coincidences. Whenever S exceeds the classical bound $S > 2$, the polarization correlations cannot

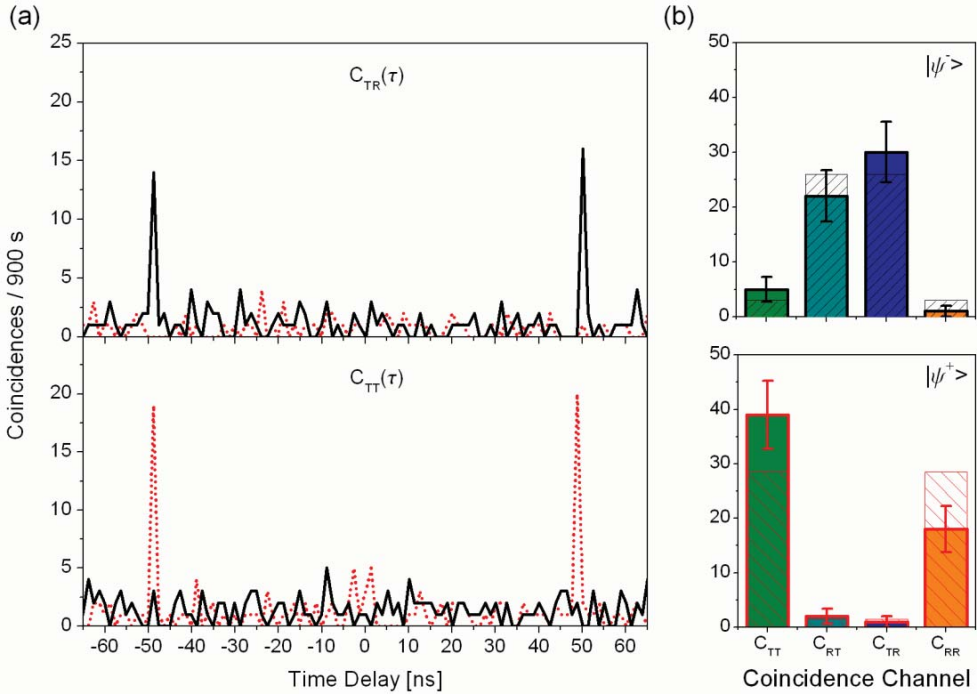

FIG. 2: Coincidence histograms and the respective accumulated coincidence events for measurements on two different Bell states. (a) Timing distribution of two out of four coincidence channels. $C_{\mathrm{TR}}(\tau)$ and $C_{\mathrm{TT}}(\tau)$ between detectors $\mathrm{D_A^T}$-$\mathrm{D_B^R}$ (top) and $\mathrm{D_A^T}$-$\mathrm{D_B^T}$ (bottom) for a $\left|\Psi^-\right\rangle$ state (black line) and a $\left|\Psi^+\right\rangle$ state (dotted red line). The analyzer wave plates $\mathrm{HWP_A}$ and $\mathrm{HWP_B}$ in the detection module were set to $(\pi/8, \pi/8)$. For each detector combination, there are two coincidence peaks at ± 50 ns which can be clearly distinguished from the accidental background. (b) Total coincidence counts and Poissonian standard deviations for all four relevant coincidence channels integrated over a 1.25 ns time window centred at the peak positions. They show distinct $\left|\Psi^-\right\rangle$ (top) and $\left|\Psi^+\right\rangle$(bottom) signatures. The full-colored columns show the joint results of the four corresponding detector combinations necessary to fully characterize the state. The dashed columns show the ideal expectation. The accumulation time for each measurement was 900 seconds.

be explained by local hidden variable models [13]. For the maximally entangled state $|\Psi^-\rangle$, quantum theory predicts a value of $S_{\max} = 2\sqrt{2}$ for the settings $(\alpha, \beta, \alpha', \beta') = (0, \pi/8, \pi/4, 3\pi/8)$.

Before measuring the polarization correlations for equation 2, we had to establish a common polarization reference frame between the individual transmitters and the receiver and to adjust the phase ϕ of the quantum state in equation 1 such that the detected coincidence signature was consistent with one of the desired Bell states.

For the polarization compensation, we used an auxiliary 808 nm laser diode, which was directed at the entangled source such that linearly polarized light was coupled into the fibres at a well defined single-photon level (figure 1). We set $\mathrm{HWP_A}$ and $\mathrm{HWP_B}$ in the detection module to (0,0), measuring in the $|H/V\rangle$ basis, and we manually adjusted the fibre polarization controllers at the source to maximize the single-photon polarization visibility $V_{\mathrm{H/V}}$ in the remote detectors. The achieved visibility in this basis was typically 95%.

Once the linear polarization was set, the auxiliary laser was switched off and ϕ was adjusted using entangled photons. The visibility $V_{\pm}$ in the $|\pm\rangle$ basis depends on ϕ as $V_{\pm} = V_0 \cos(\phi)$. To determine the relation between ϕ and the wave plates controlling the pump laser in the source (HWPs, QWPs) we set $\mathrm{HWP_A}$ and $\mathrm{HWP_B}$ in the detection module to $(\pi/8, \pi/8)$, measured $V_{\pm}$ for three different settings of HWPs and QWPs in the equatorial plane of the Poincar sphere representing the pump laser polarization (see ref. [16]) and then numerically fitted a cosine function to the obtained data points. The fitted two-photon fringes in figure 3 have a visibility of $V_0 = 84\% \pm 2.4\%$. From this fit we deduced the wave plate settings to obtain either a $|\Psi^-\rangle$ or a $|\Psi^+\rangle$ state in the detection module. This procedure was repeated each night at the beginning of a measurement.

The coincidence measurements in figure 2 were obtained after we prepared $|\Psi^-\rangle$ and $|\Psi^+\rangle$ states with this method. The measured respective visibility of $V_{\pm} = 80\% \pm 7.6\%$ and $V_{\pm} = 90\% \pm 5.5\%$ at the receiver is depicted in figure 3. As the linear polarization of the individual photons can be adjusted arbitrarily at the source, we were thus able to prepare, transmit and distinguish at the receiver any of the 4 Bell states.

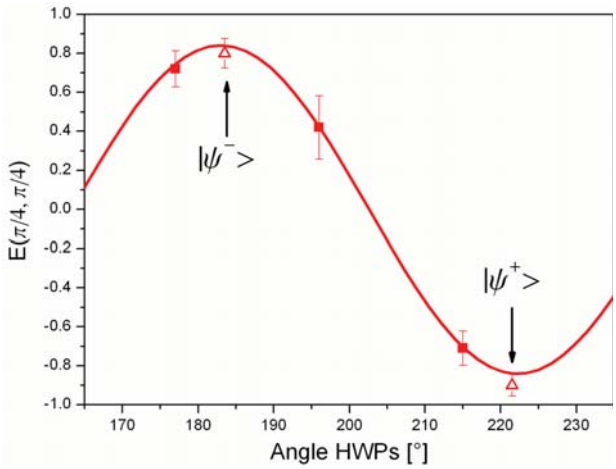

FIG. 3: Scan of the phase ϕ of the entangled two-photon state in one measurement night. We measured the visibility of the entangled states in the $|\pm\rangle$ basis for three settings of the wave plates controlling the pump laser (squares). After fitting a cosine function ($V_0 = 84\% \pm 2.4\%$) to these data points we were able adjust the source to emit either $\left|\Psi^-\right\rangle$ or $\left|\Psi^+\right\rangle$ states. We prepared these states and observed, in this example, a visibility of $V_\pm = 90 \pm 5.5\%$ for the $\left|\Psi^+\right\rangle$ and $V_\pm = 80\% \pm 7.6\%$ for the $\left|\Psi^-\right\rangle$ state (triangles).

Results - The detection module in our experiment allowed us to directly measure the expectation values $\mathrm{E}(\theta_A, \theta_B)$ in equation 2 with 4 different sets of angles of $\mathrm{HWP_A}$ and $\mathrm{HWP_B}$ (table I). We first aligned the system to obtain a $|\Psi^-\rangle$ state at the receiver. For each setting (θ_A, θ_B), we repeatedly accumulated data for typically 900 seconds, which eventually amounted to a total of 9900 seconds acquired in three consecutive nights. Each detector registered a dark count rate of ∼400 /s, of which ∼200 /s were intrinsic and ∼200 /s originated from background light. On average, we received 2500 single-photons/s and 0.071 transmitted photon pairs/s. Relating to the local rates at the source, the single-photon link attenuation was therefore 34.1 dB and the pair attenuation 71.2 dB. To this total channel attenuation, 3 dB were contributed by the BS in the receiver module and 2 dB were due to the lower efficiency of the detectors used at the receiver (∼25%) compared to those at the source (∼40%). The average net attenuation of the free-space link was thus 32.1 dB and 64.2 dB respectively. This shows that the two transmitter modes in our experiment are truly as independent as they would be in a QKD experiment with two separated receiver telescopes. Even though the final singles-to-coincidence ratio at the receiver was just 1.7×10^{-5}, the coincidence signal-to-noise ratio (SNR) was as high as ∼15:1.

The accumulated coincident events for the different detector pairs yielded the correlation values shown in table I.

(θ_A, θ_A)	$\mathrm{E}(\theta_A, \theta_B)$	$\Delta\mathrm{E}(\theta_A, \theta_B)$
$(0, \pi/8)$	-0.604	0.059
$(\pi/4, \pi/8)$	0.672	0.055
$(0, 3\pi/8)$	0.638	0.056
$(\pi/4, 3\pi/8)$	0.697	0.058

TABLE I: Experimental polarization correlations $\mathrm{E}(\theta_A, \theta_B)$ for the CHSH inequality. The total integration time was 9900 seconds. The standard deviations $\Delta\mathrm{E}(\theta_A, \theta_B)$ were calculated assuming Poissonian photon count statistics.

According to equation 2, the resulting CHSH Bell parameter S is:

$$S = 2.612 \pm 0.114. \tag{3}$$

This is a distinct violation of the CHSH inequality by 5.4 standard deviations and thus a convincing proof of the successful transmission of highly entangled Bell states. Over the course of the whole experiment the two-photon fringe visibility V, which is linked to the CHSH S-value via $S = V \times S_{\max}$, was $V = 92.3\% \pm 4.4\%$. In a QKD experiment [18], this would correspond to a quantum bit error ratio of $3.85\% \pm 2.2\%$ which is well below the limit necessary to

exclude an eavesdropper. From the time-tags recorded for measurements in the $|H/V\rangle$ and $|\pm\rangle = \frac{1}{\sqrt{2}}(|H\rangle \pm |V\rangle)$ basis, we can extract a secure key with a rate of ∼0.03 bits/s. According to ref. [14], a detailed analysis of all error sources, including the source visibility (99.2%), multi-photon pair emissions, the polarization contrast of the detection module (99.5%) and the background, reveals that a maximal visibility of 92.8% can be achieved. The observed V=92.3% is in very good agreement to this limit. The same analysis reveals that, with our setup, a secure key could certainly be obtained up to an overall channel attenuation of ∼80 dB.

Conclusion - In conclusion, we have transmitted both photons of entangled pairs over a 144 km channel with a total loss of 71.2 dB. This corresponds to the expected loss regime for satellite quantum communication with two ground receivers [6]. Even though in our experiment the same receiver telescope was used for both photons, the two transmitter modes are spatially separated. Our experiment therefore realistically emulates QKD using entangled photons in a symmetric scheme, where the photon source is placed in between two receiver stations which are separated by 288 km. The locally created photon-pair rate of 10^7 pairs/s matches the optimal rate for quantum communication in space estimated in ref. [6] and the SNR of 15:1 at the receiver significantly exceeds the SNR of 4.8 required for a Bell-inequality violation. The source for entangled photons, pumped by a low-power diode laser, can be readily integrated for a satellite-borne quantum communication terminal which was not the case for hardware used in refs. [8, 11]. By violating the CHSH inequality by more than 5 standard deviations, we have shown that the received two-photon states are still highly entangled. Our results confirm that the photons are virtually not subject to decoherence on their 144 km flight through air. In addition to proving the feasibility of entanglement-based satellite quantum communication with two receiver stations, we lay the groundwork for the implementation of two-photon quantum communication protocols over high-loss free-space channels.

Acknowledgments

We are grateful to H. Weinfurter, F. Sanchez, A. Alonso (IAC), J. Perdigues and Z. Sodnik (ESA), T. Augusteijn and the staff of the Nordic Optical Telescope in La Palma for their support at the trial sites. This work was supported by ESA under the General Studies Programme (No. 18805/04/NL/HE), the European Commission through Project QAP (No. 015846), the DTO-Funded U.S. Army Research Office, the Austrian Science Foundation (FWF) under project number SFB1520 and the ASAP-Programme of the Austrian Space Agency (FFG).

[1] N. Gisin and R. Thew, Nature **1**, 165 (2007).
[2] H. Takesue, S. Nam, Q. Zhang, R. Hadfield, T. Honjo, K. Tamaki, and Y. Yamamoto, Nature **1**, 343 (2007).
[3] D. Bouwmeester, A. Ekert, and A. Zeilinger, *The Physics of Quantum Information: Quantum Cryptography, Quantum Teleportation, Quantum Computation* (Springer, 2001).
[4] H. Hübel, M. Vanner, T. Lederer, B. Blauensteiner, T. Lorünser, A. Poppe, and A. Zeilinger, Optics Express **15**, 7853 (2007).
[5] L. Duan, M. Lukin, J. Cirac, and P. Zoller, Nature **414**, 413 (2001).
[6] M. Aspelmeyer, T. Jennewein, M. Pfennigbauer, W. Leeb, and A. Zeilinger, Selected Topics in Quantum Electronics, IEEE Journal of **9**, 1541 (2003).
[7] M. Aspelmeyer, H. Bohm, T. Gyatso, T. Jennewein, R. Kaltenbaek, M. Lindenthal, G. Molina-Terriza, A. Poppe, K. Resch, M. Taraba, et al., Science **301**, 621 (2003).
[8] C. Peng, T. Yang, X. Bao, J. Zhang, X. Jin, F. Feng, B. Yang, J. Yang, J. Yin, Q. Zhang, et al., Physical Review Letters **94**, 150501 (2005).
[9] K. Resch, M. Lindenthal, B. Blauensteiner, H. Böhm, A. Fedrizzi, C. Kurtsiefer, A. Poppe, T. Schmitt-Manderbach, M. Taraba, R. Ursin, et al., Optics Express **13**, 202 (2005).
[10] I. Marcikic, A. Lamas-Linares, and C. Kurtsiefer, Applied Physics Letters **89**, 101122 (2006).
[11] R. Ursin, F. Tiefenbacher, T. Schmitt-Manderbach, H. Weier, T. Scheidl, M. Lindenthal, B. Blauensteiner, T. Jennewein, J. Perdigues, P. Trojek, et al., Nature Physics **3**, 481 (2007).
[12] T. Schmitt-Manderbach, H. Weier, M. Fürst, R. Ursin, F. Tiefenbacher, T. Scheidl, J. Perdigues, Z. Sodnik, C. Kurtsiefer, J. Rarity, et al., Physical Review Letters **98**, 10504 (2007).
[13] J. Clauser, M. Horne, A. Shimony, and R. Holt, Physical Review Letters **23**, 880 (1969).
[14] X. Ma, C. Fung, and H. Lo, Physical Review A **76**, 12307 (2007).
[15] J. Boileau, D. Gottesman, R. Laflamme, D. Poulin, and R. Spekkens, Physical Review Letters **92**, 17901 (2004).
[16] I. Marcikic, H. de Riedmatten, W. Tittel, H. Zbinden, M. Legré, and N. Gisin, Physical Review Letters **93**, 180502 (2004).
[17] A. Fedrizzi, T. Herbst, A. Poppe, T. Jennewein, and A. Zeilinger, Opt. Express **15**, 15377 (2007).
[18] C. Bennett, G. Brassard, and N. Mermin, Physical Review Letters **68**, 557 (1992).

A.2 Lab-View Programs

A.2.1 Measurement Program

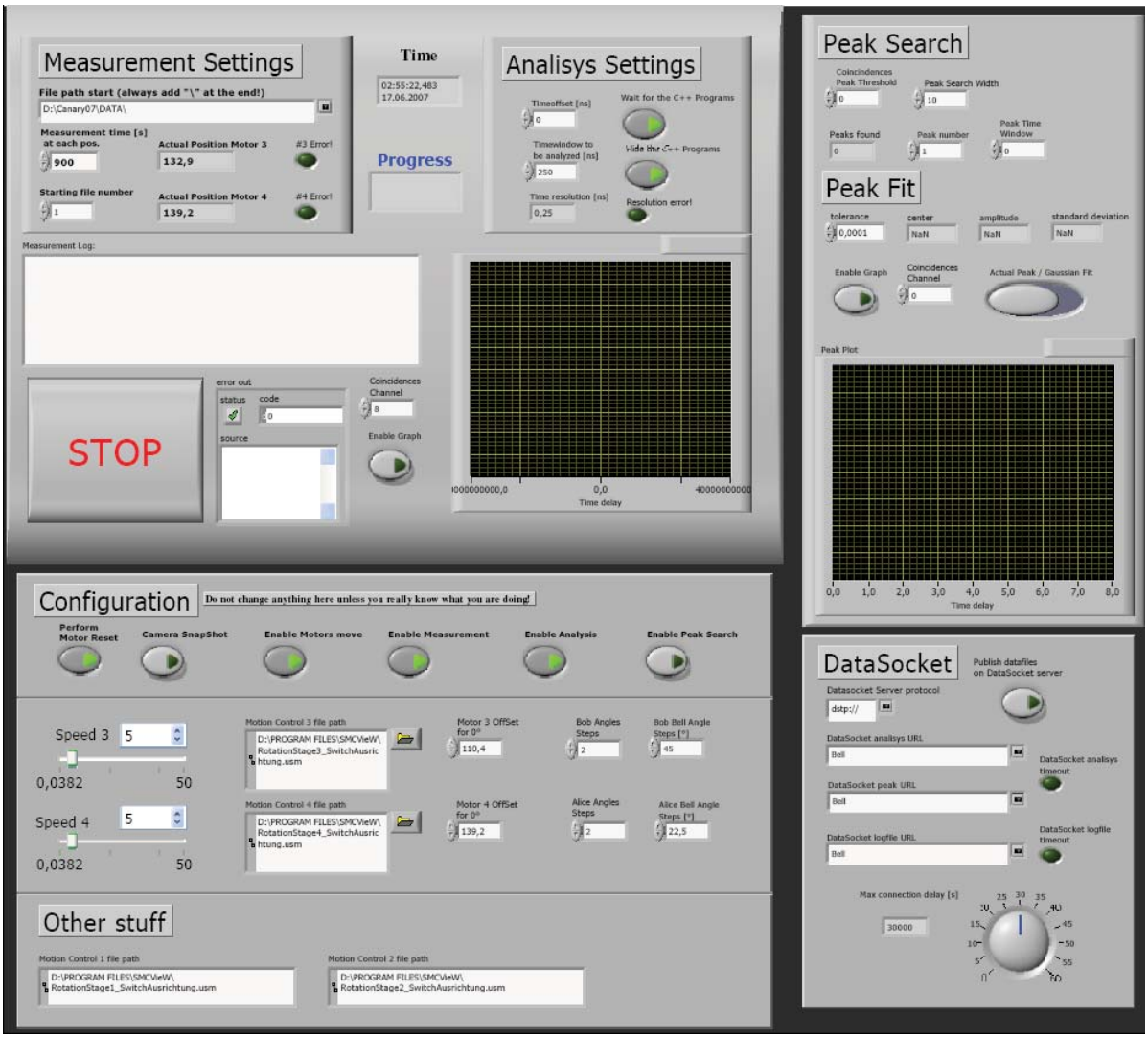

Figure A.1: The front panel of the measurement program.

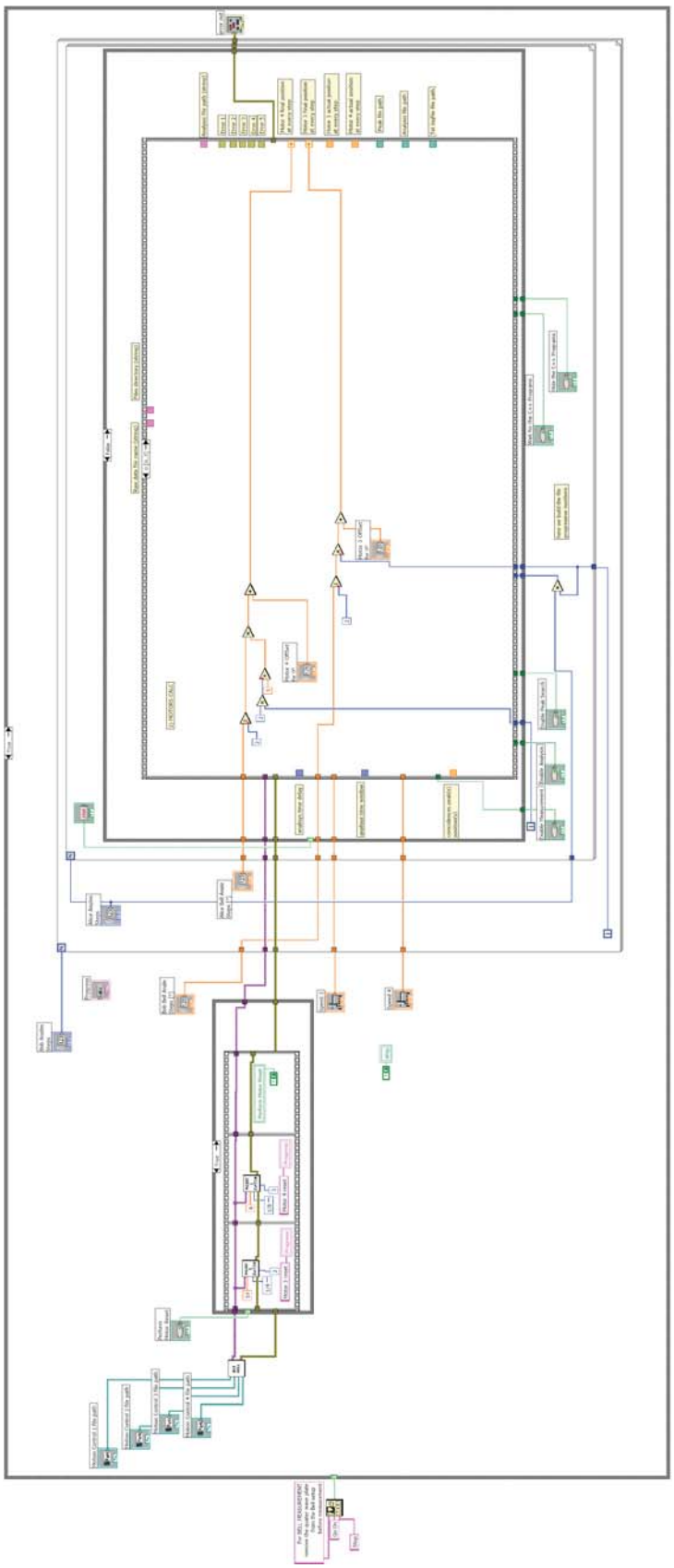

Figure A.2: The main case structure and the embedded stacked sequence structure of the block diagram.

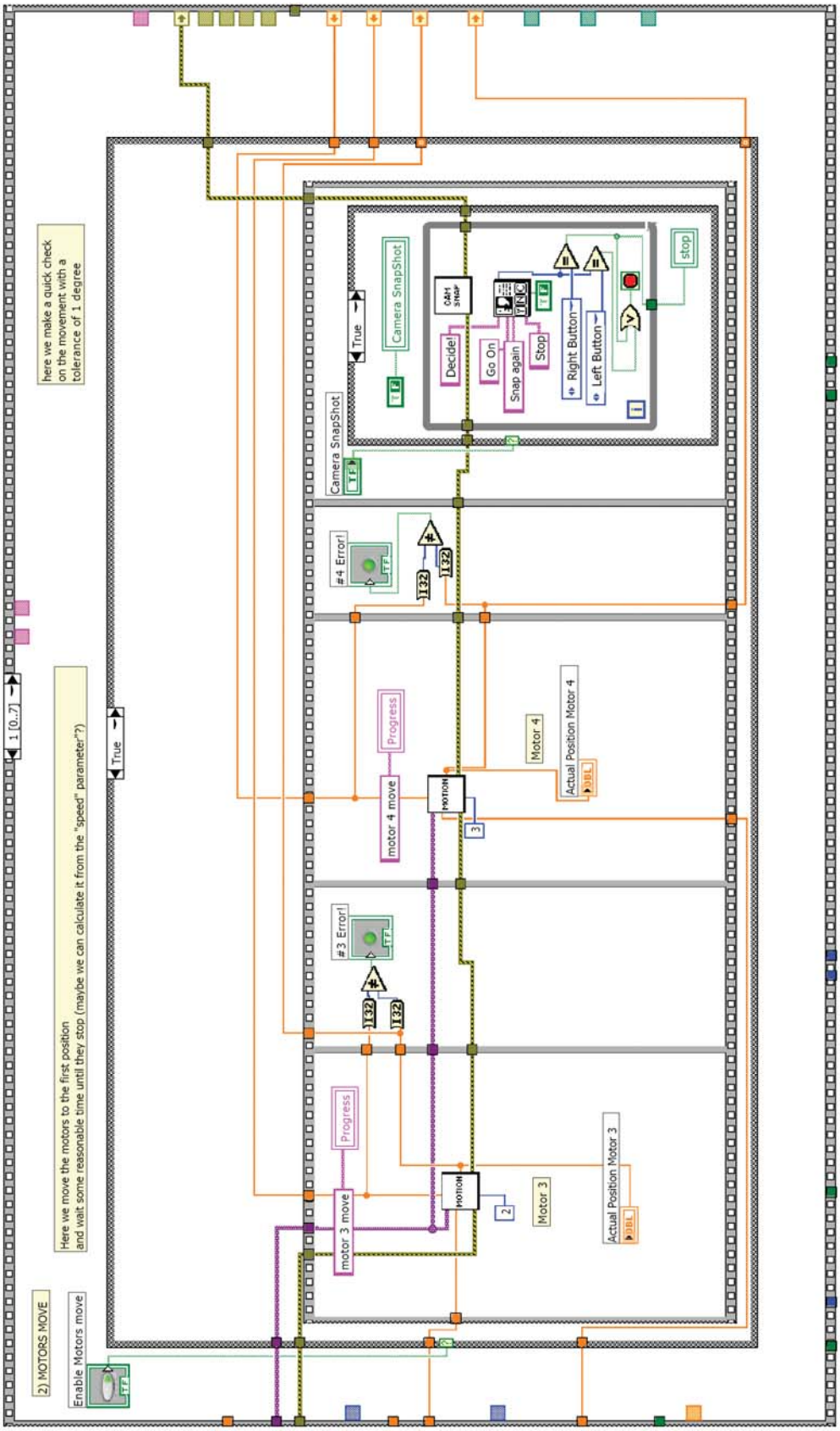

Figure A.3: Sequence 1 in the stacked sequence structure.

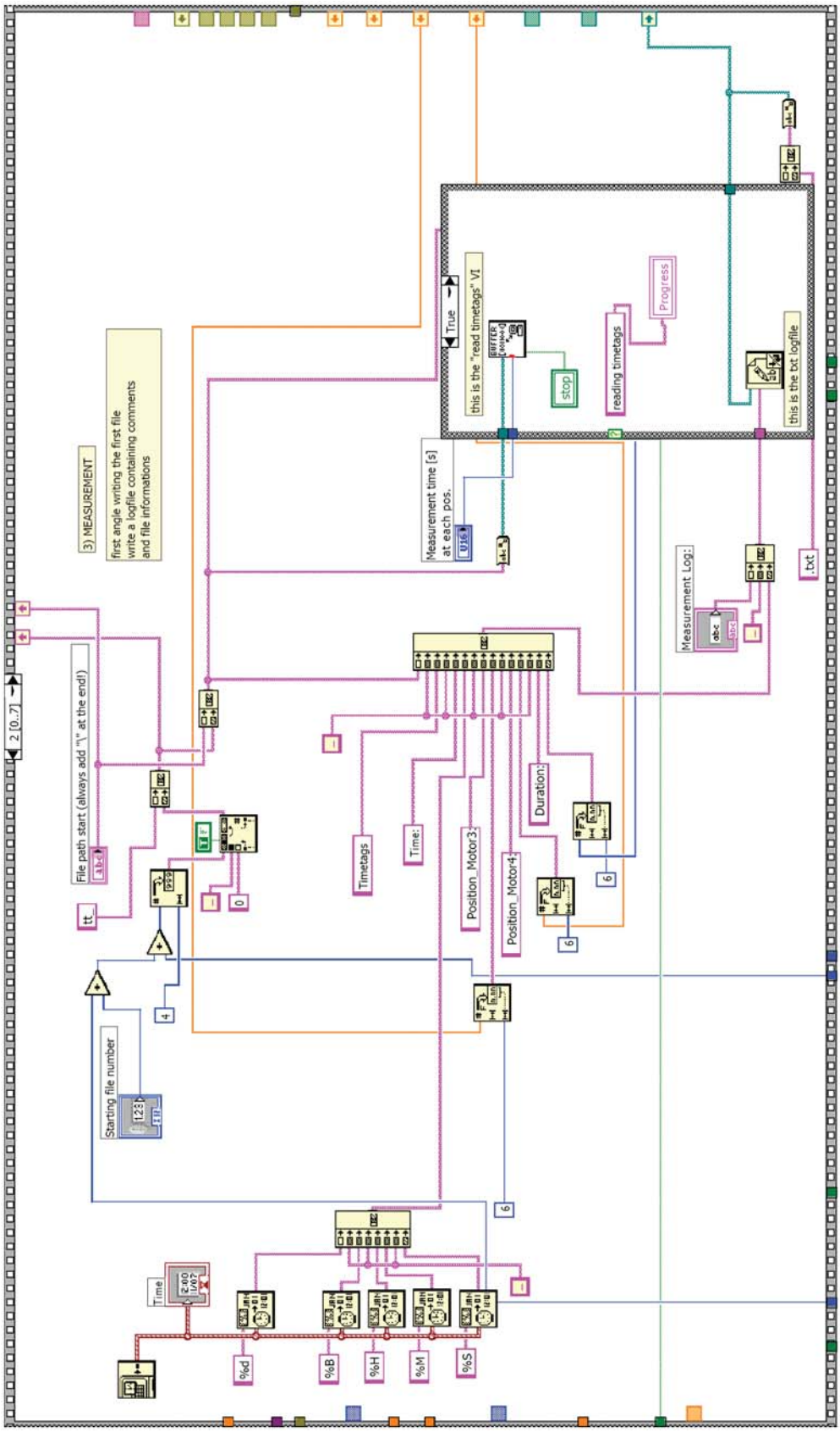

Figure A.4: Sequence 2 in the stacked sequence structure.

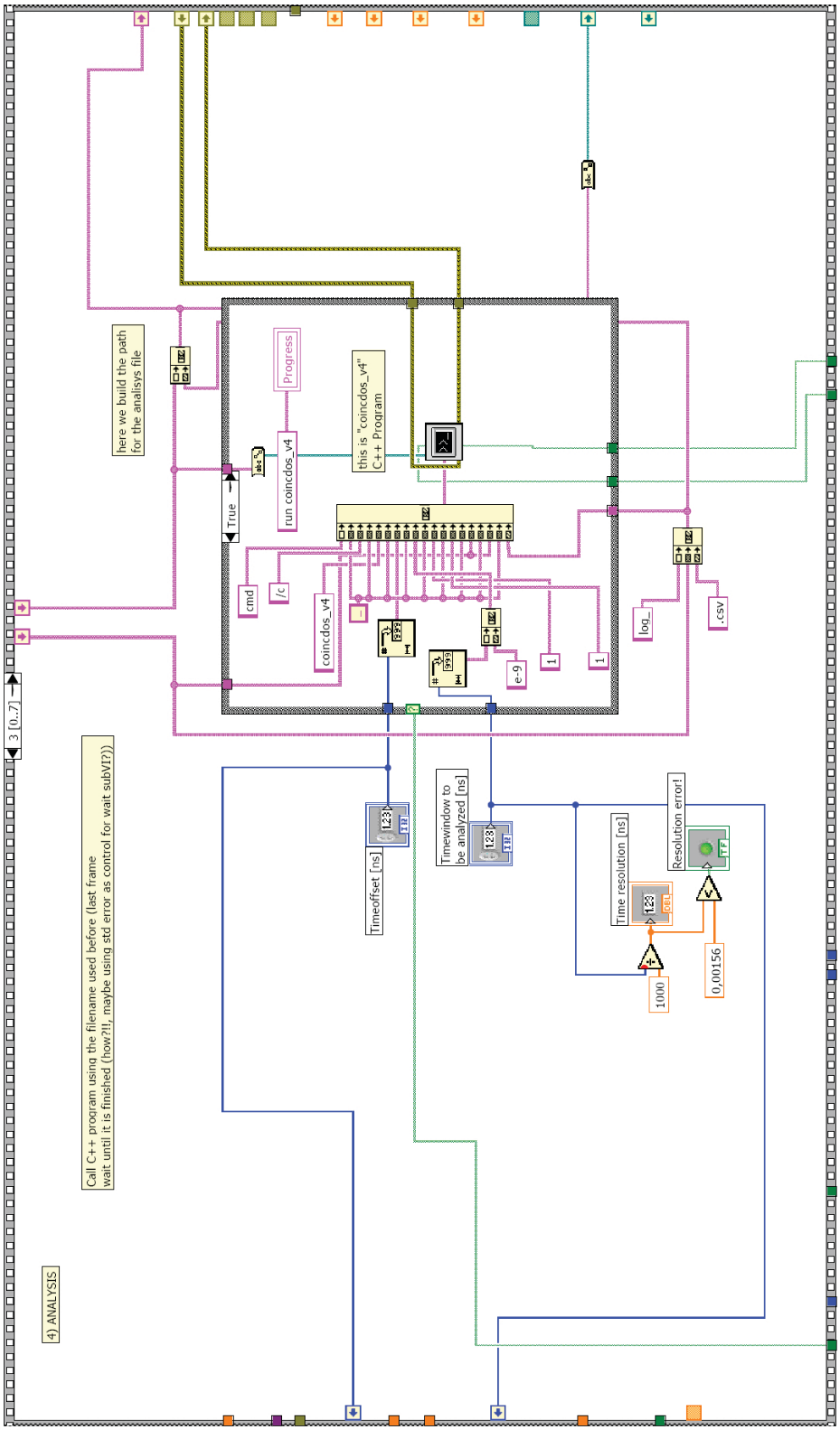

Figure A.5: Sequence 3 in the stacked sequence structure.

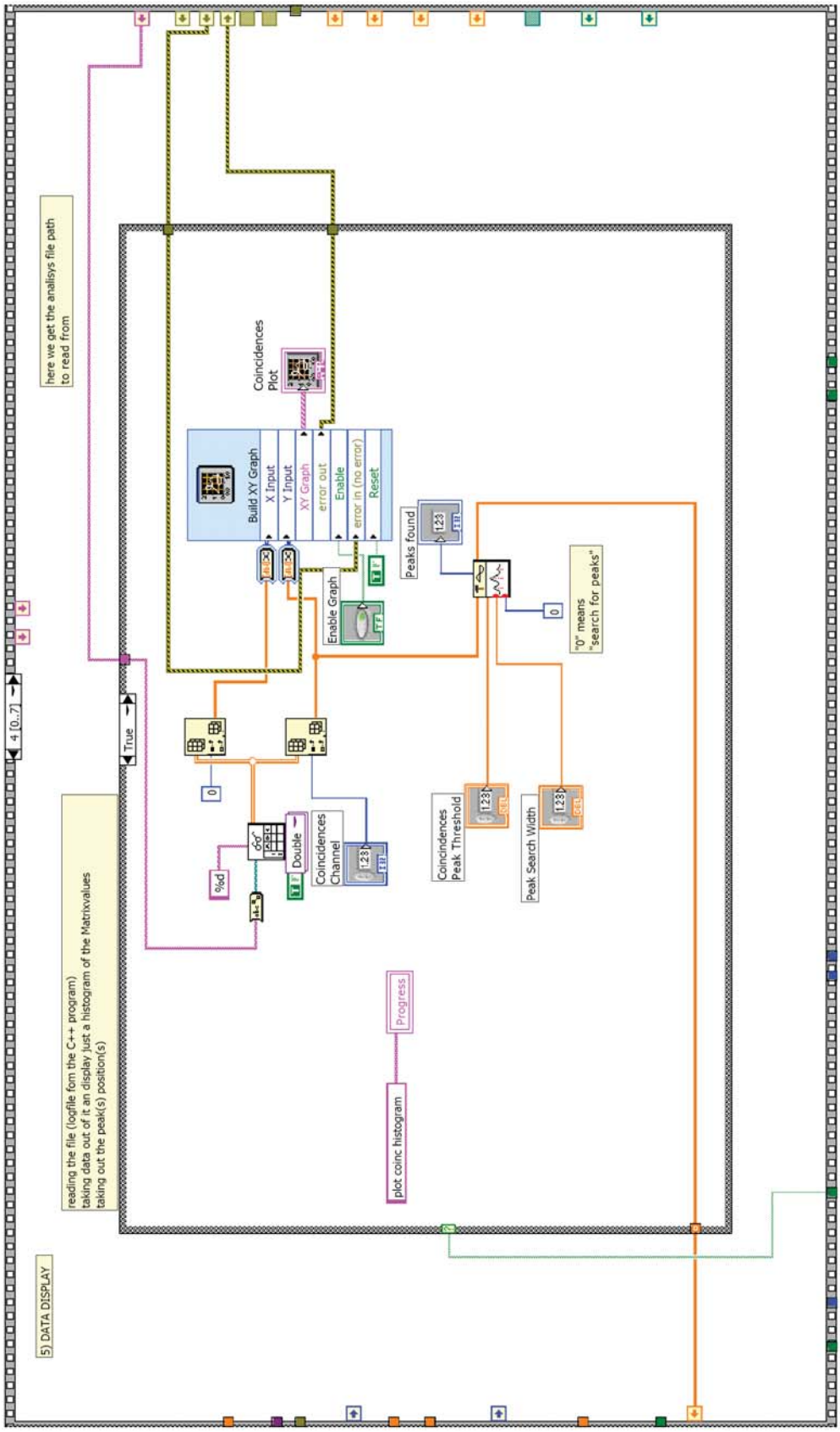

Figure A.6: Sequence 4 in the stacked sequence structure.

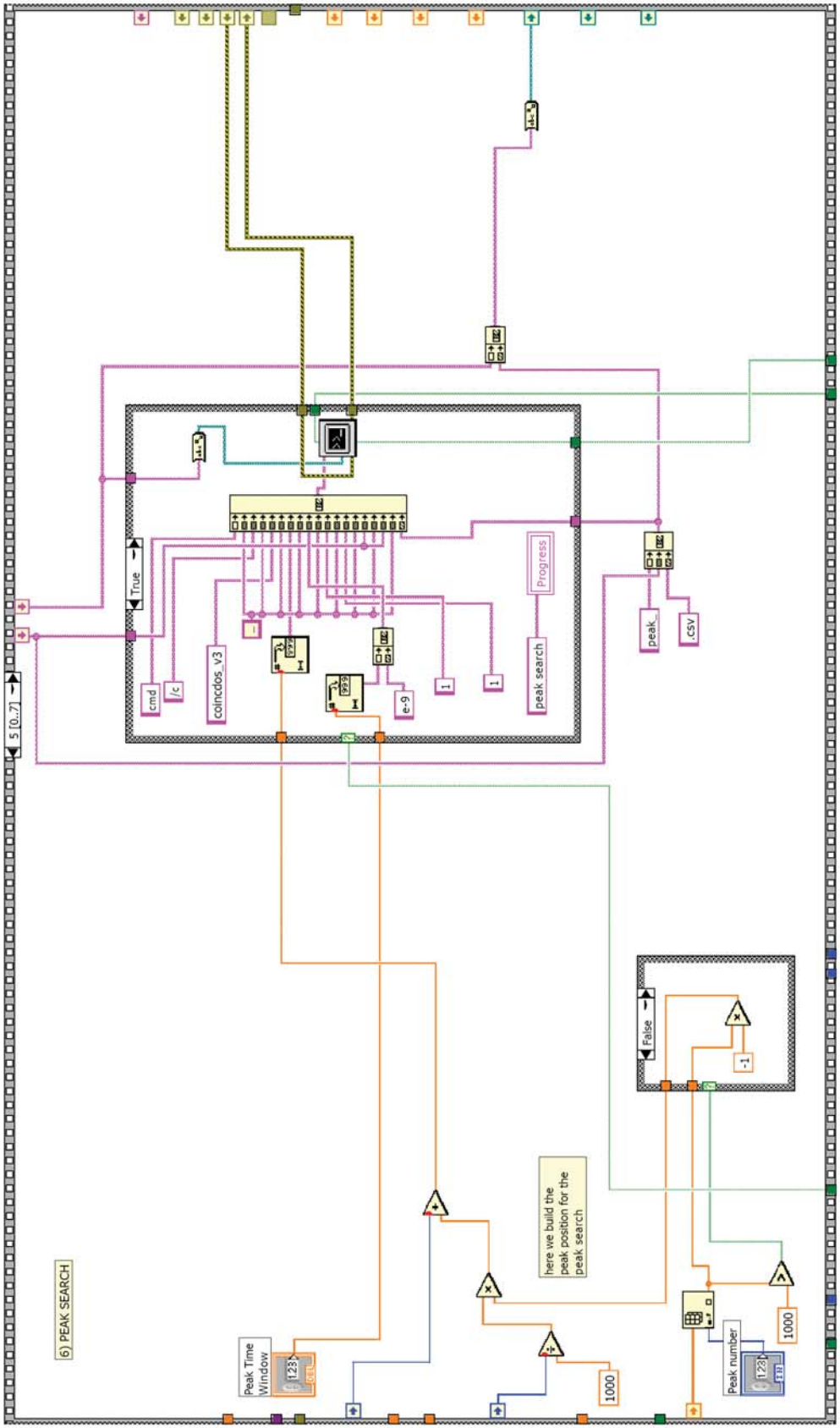

Figure A.7: Sequence 5 in the stacked sequence structure.

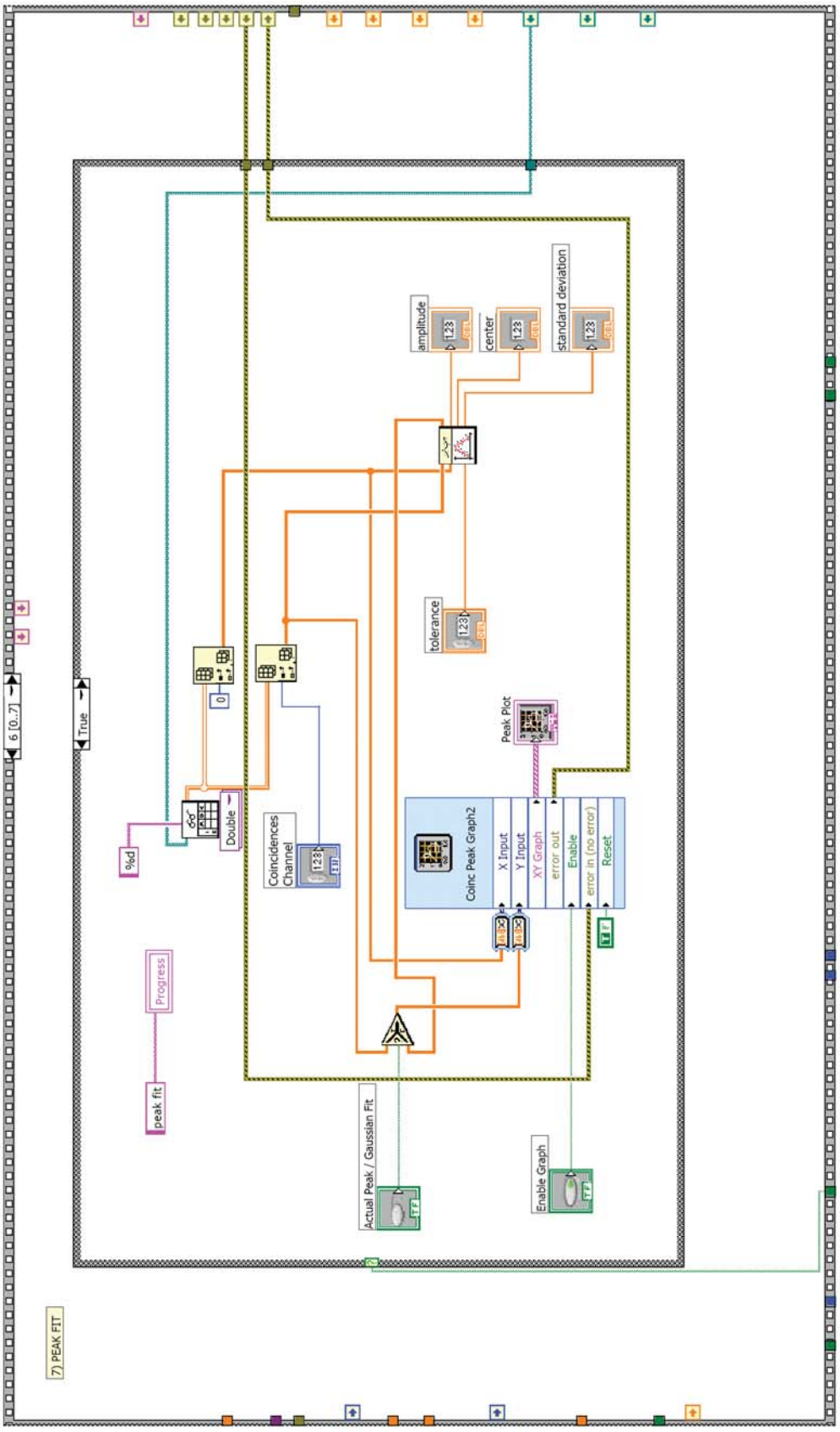

Figure A.8: Sequence 6 in the stacked sequence structure.

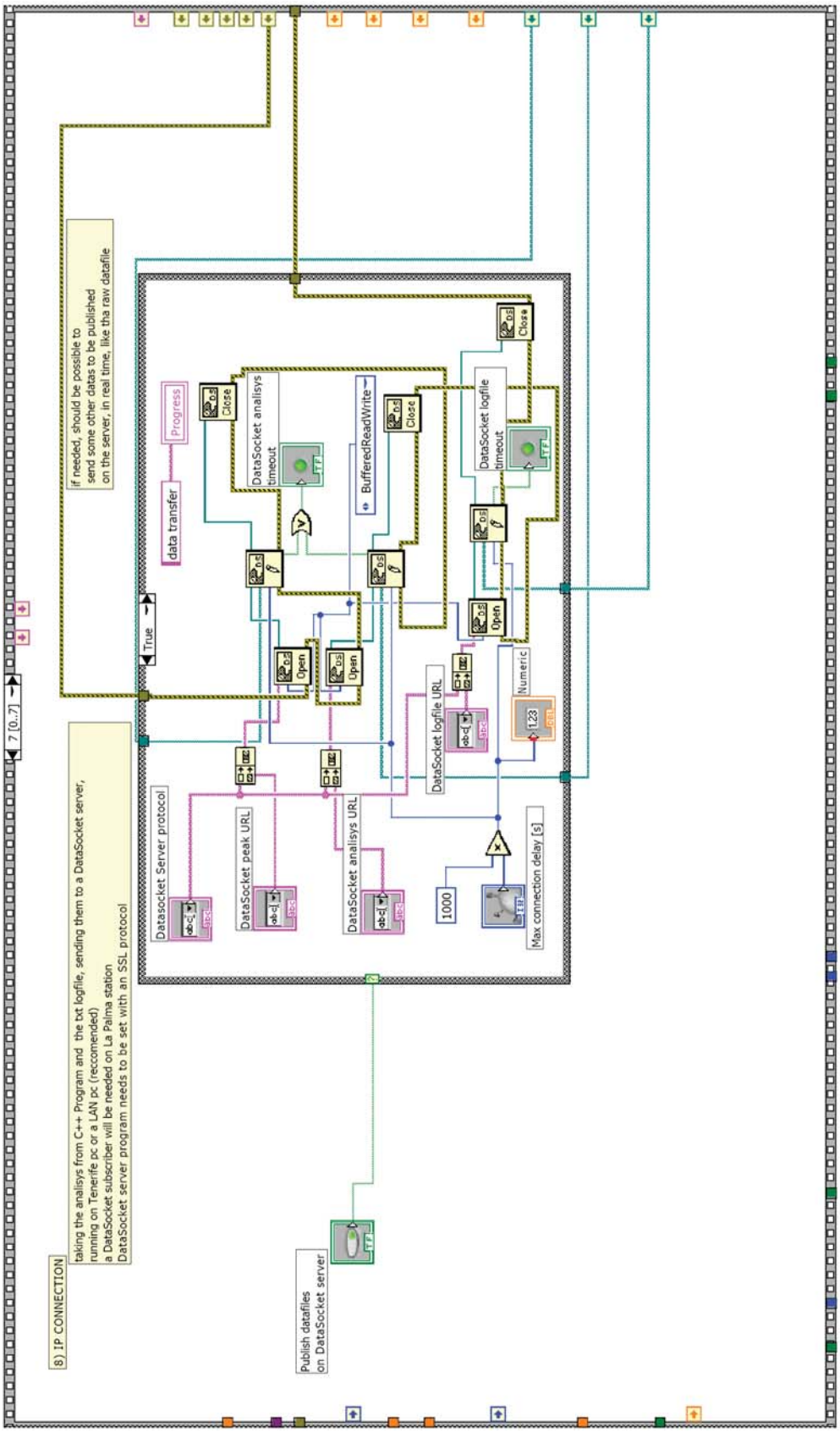

Figure A.9: Sequence 7 in the stacked sequence structure.

A.2.2 Rotation-Stage Control

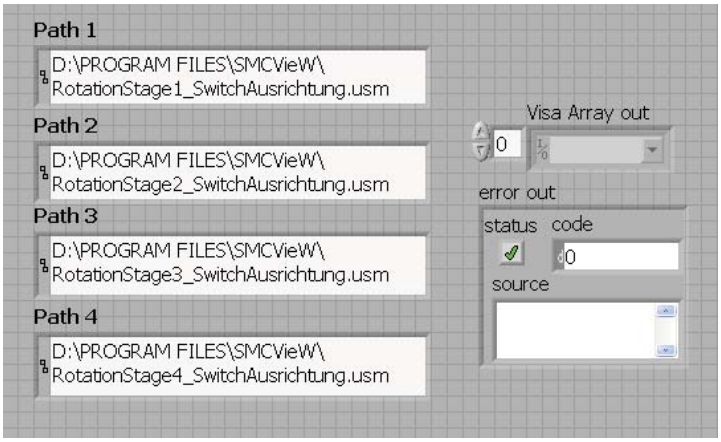

Figure A.10: The front panel of the *init_bell.vi*.

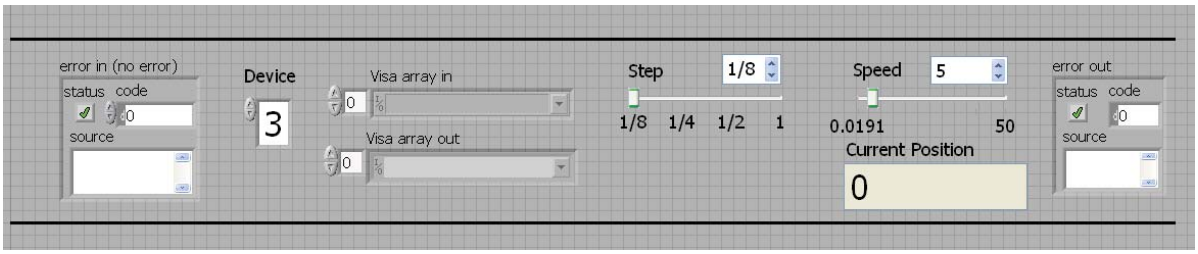

Figure A.11: The front panel of the *reset2switch.vi*.

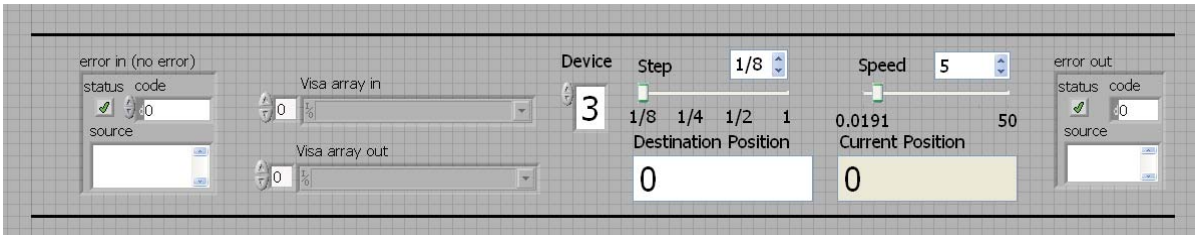

Figure A.12: The front panel of the *motion.vi*.

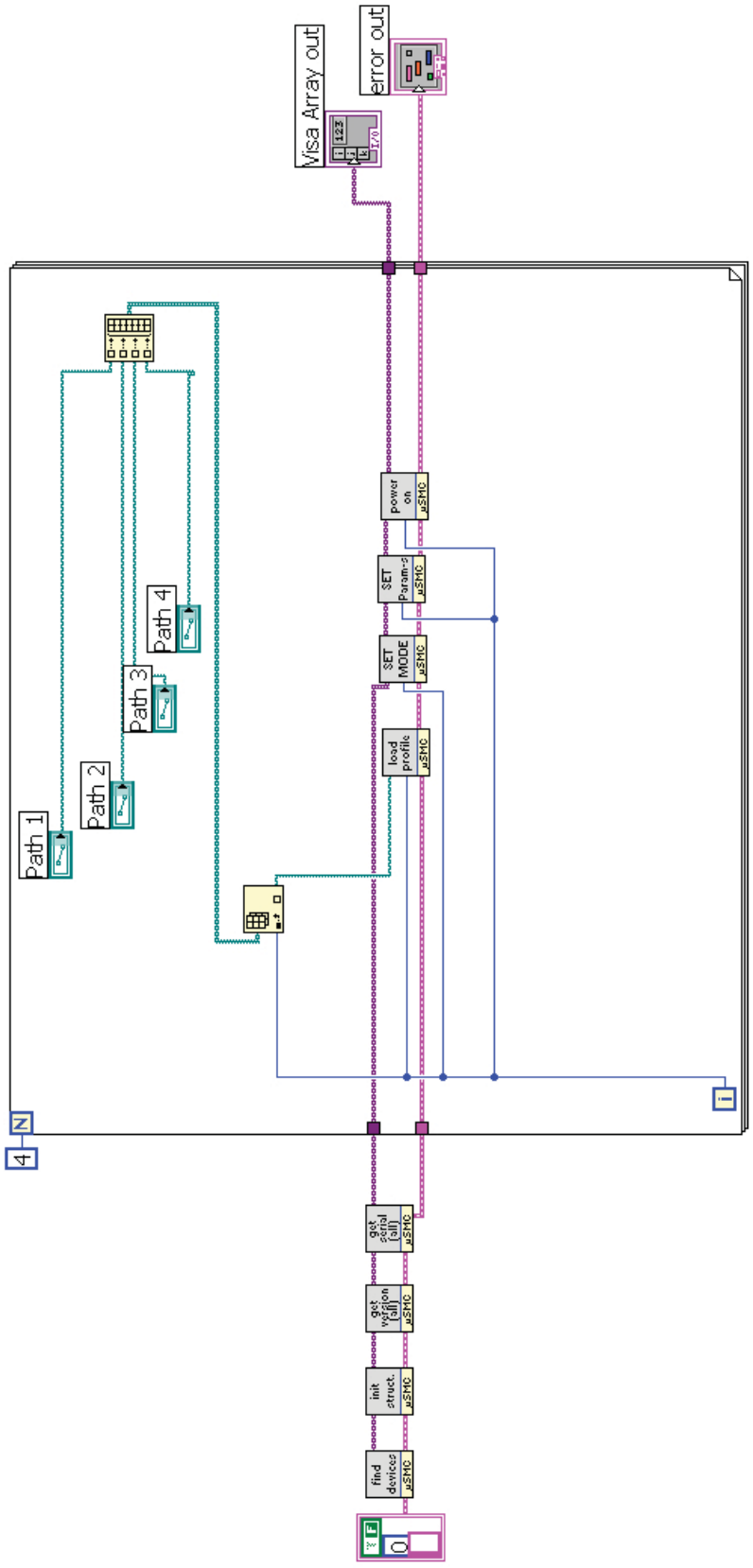

Figure A.13: The block diagram of the *init_bell.vi*.

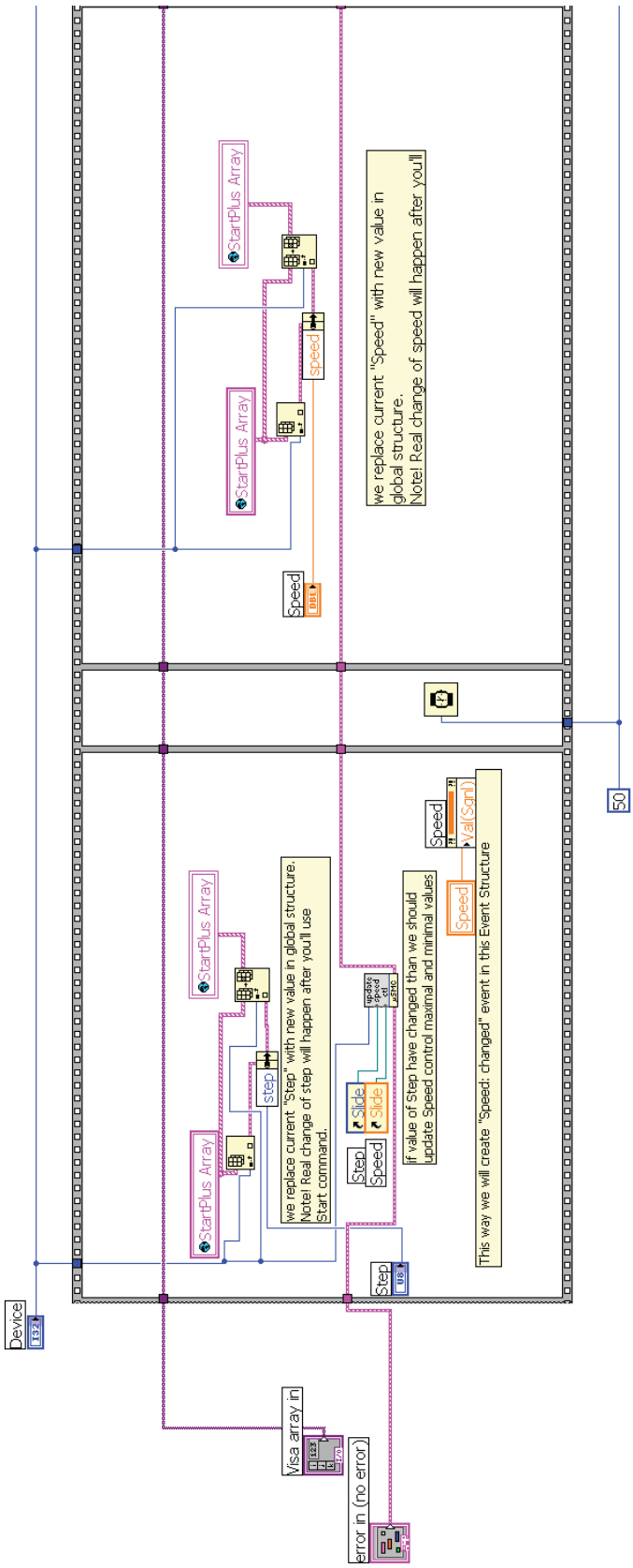

Figure A.14: The first sequence of the *reset2switch.vi*.

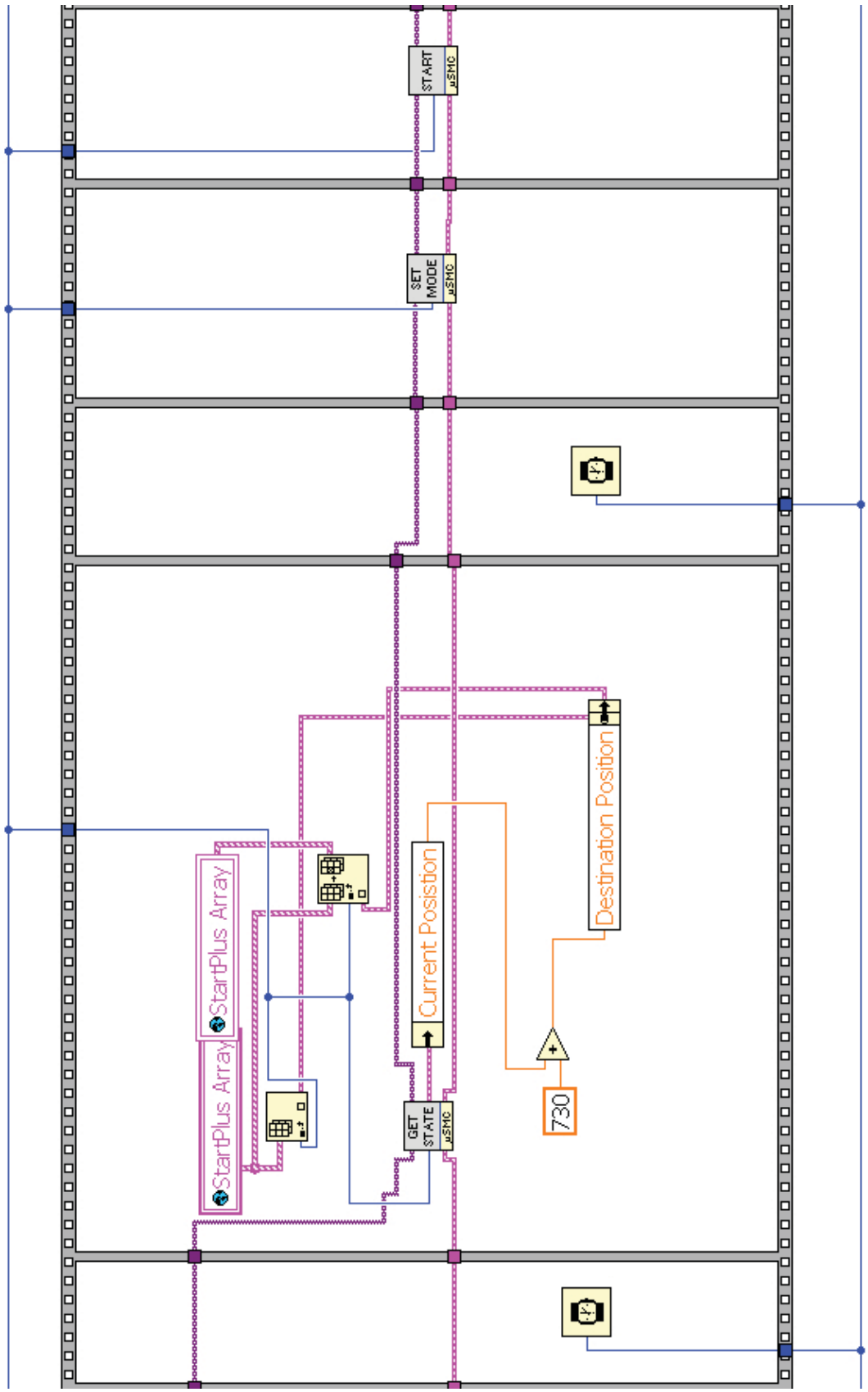

Figure A.15: The second sequence of the *reset2switch.vi*.

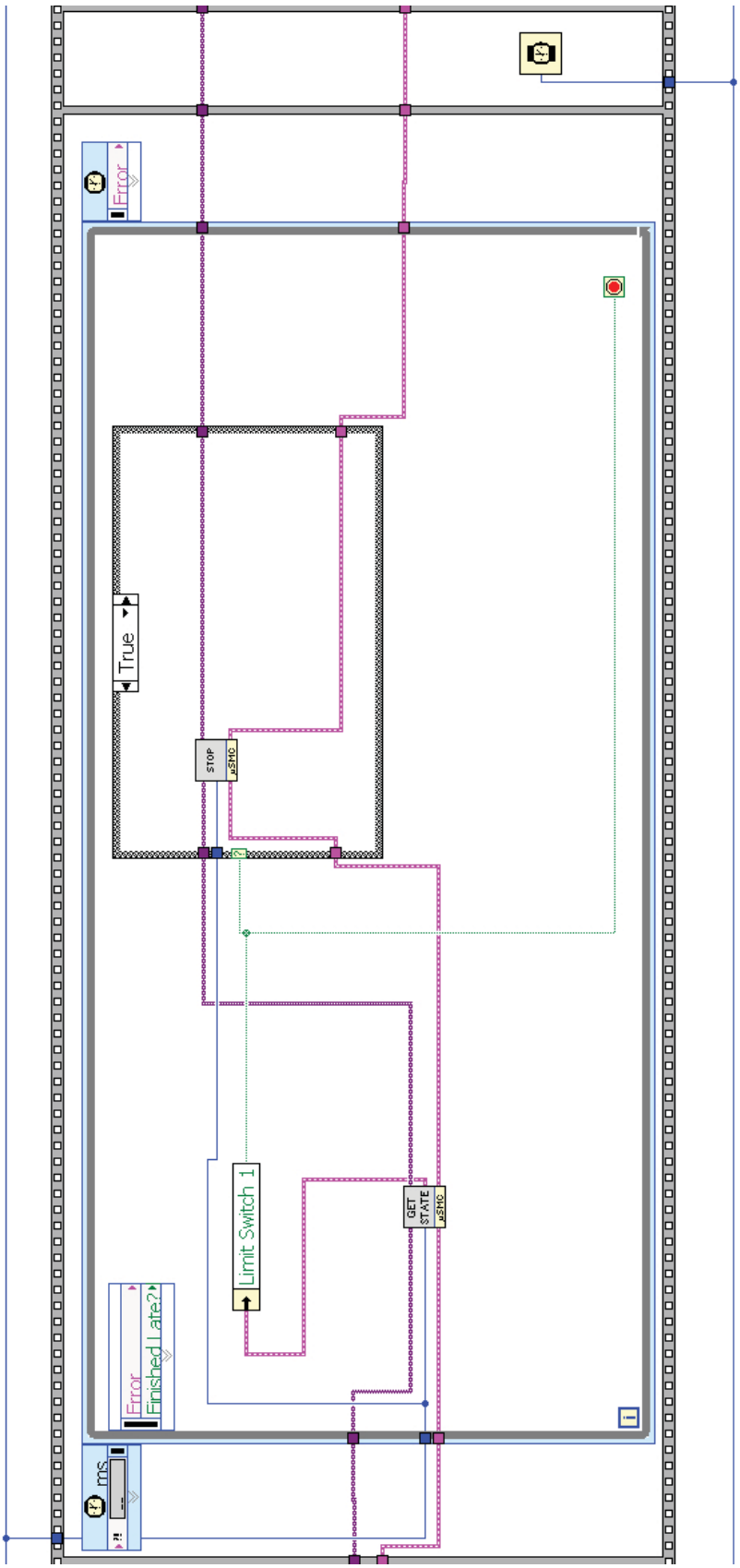

Figure A.16: The third sequence of the *reset2switch.vi*.

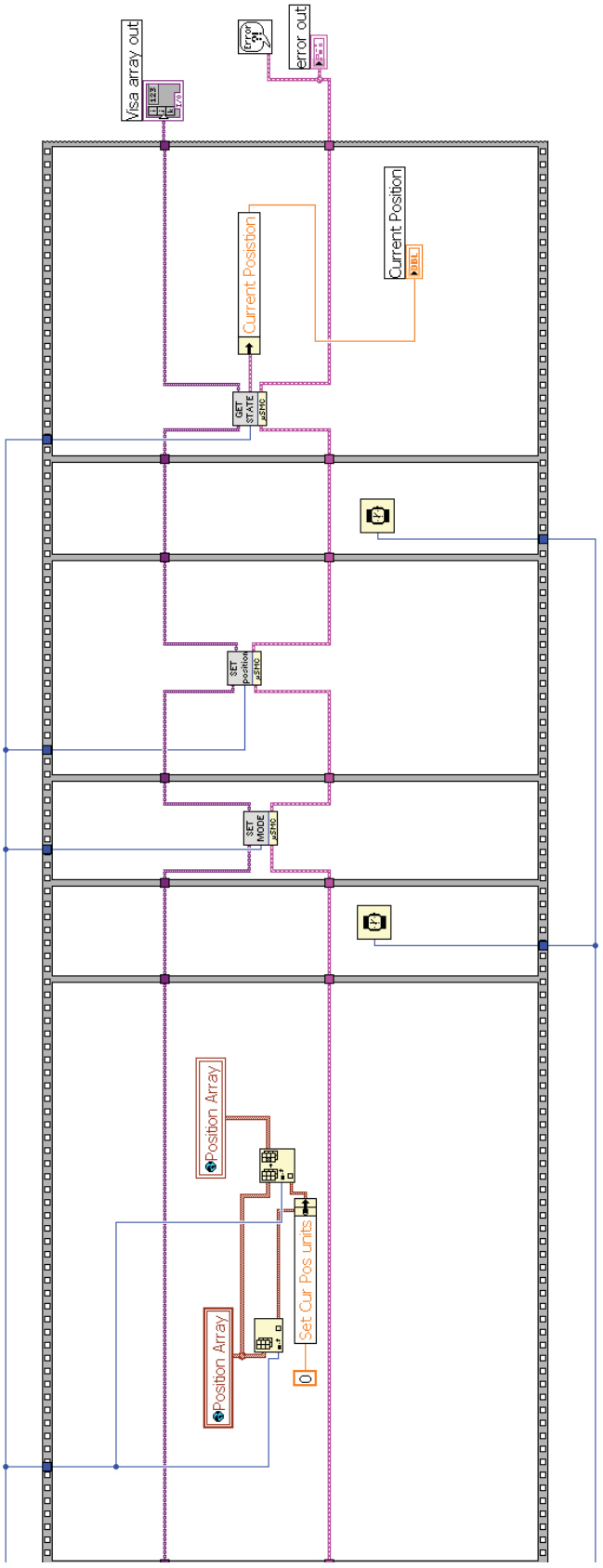

Figure A.17: The last sequence of the *reset2switch.vi*.

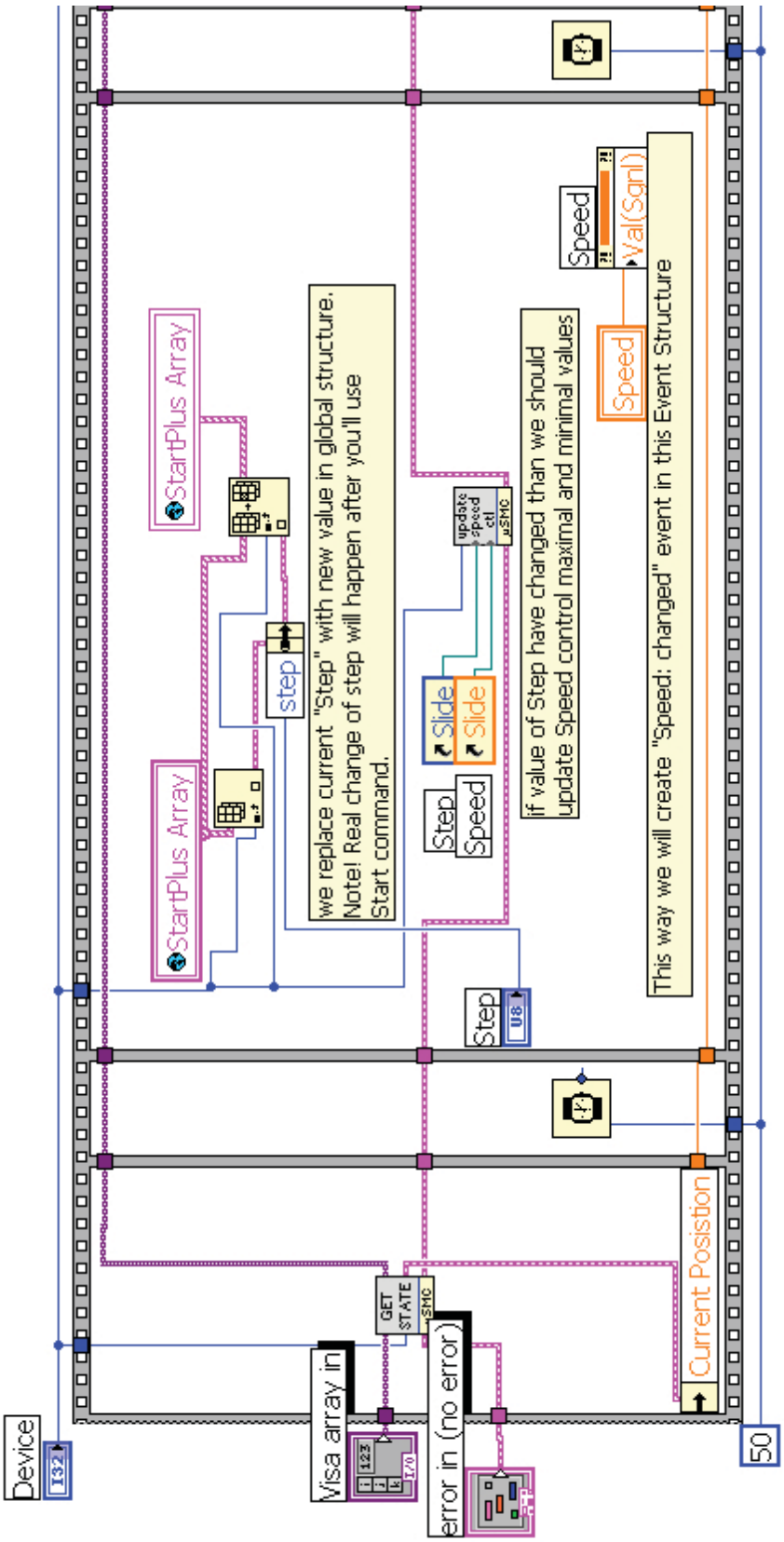

Figure A.18: The first sequence of the *motion.vi*.

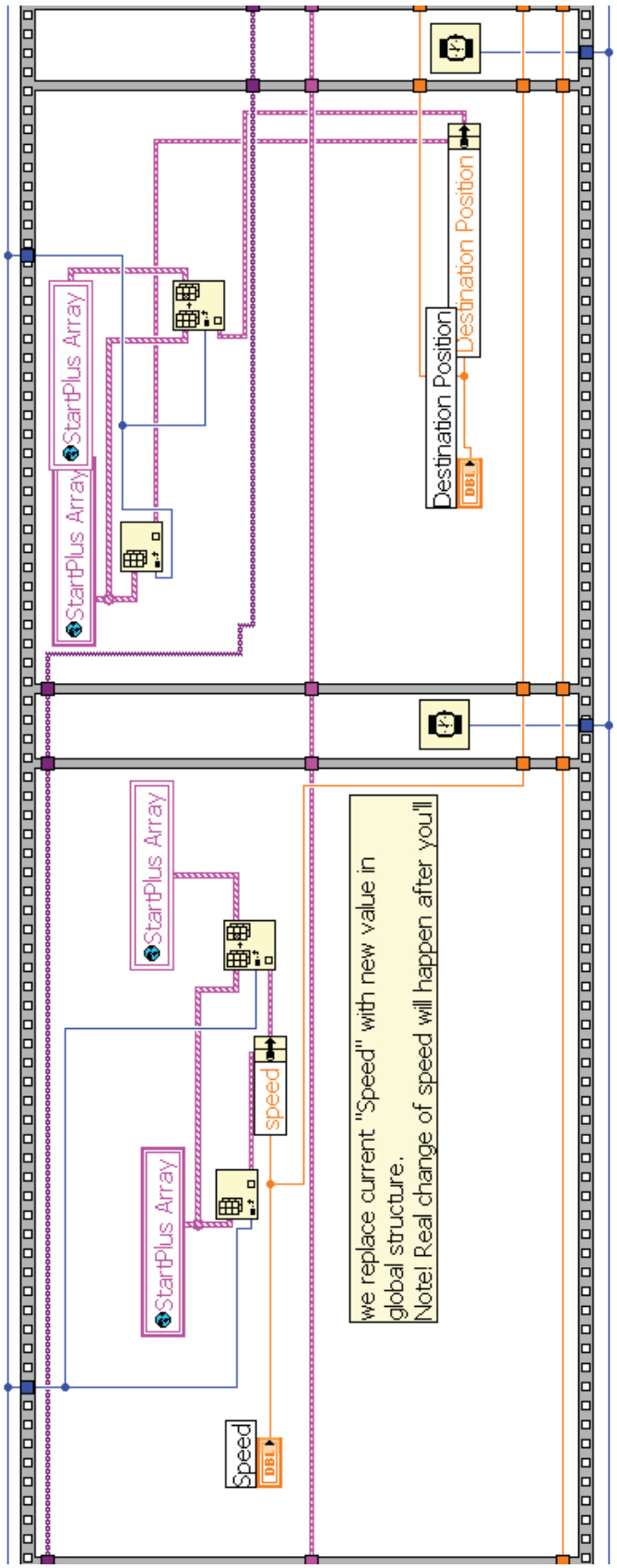

Figure A.19: The second sequence of the *motion.vi*.

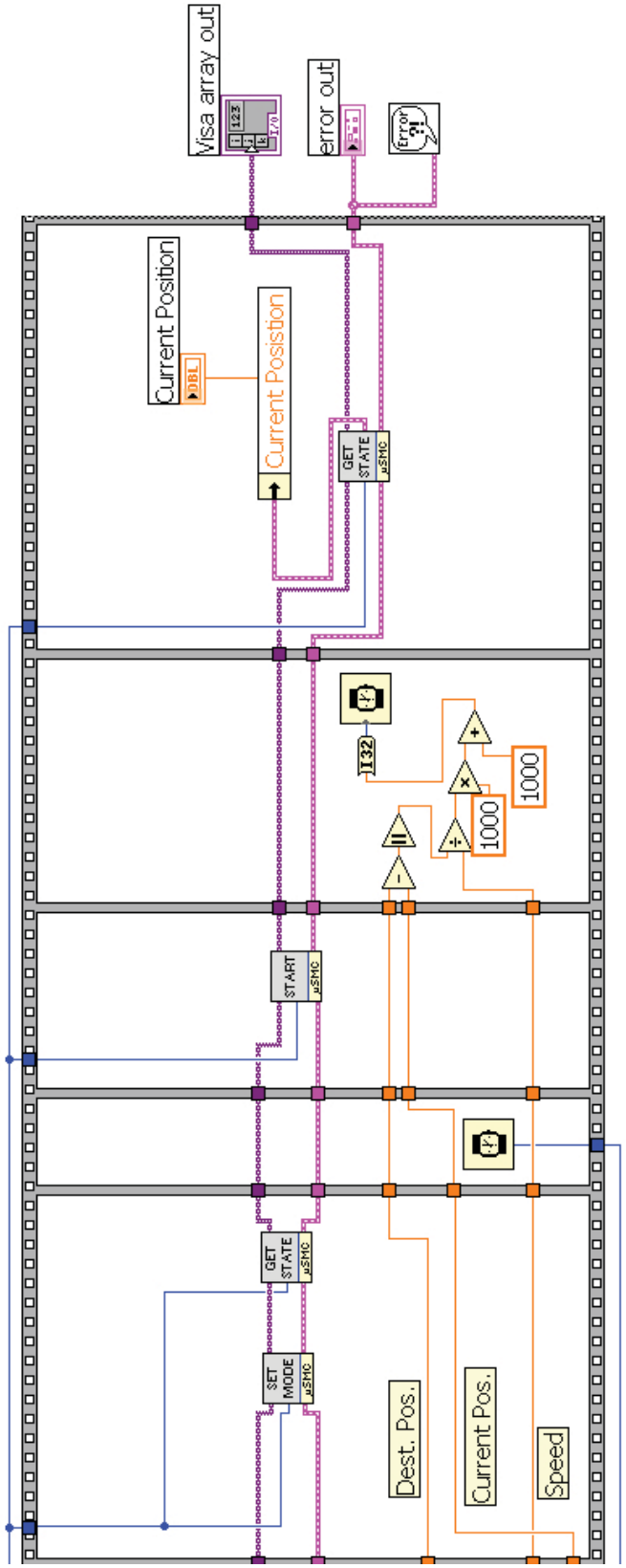

Figure A.20: The last sequence of the *motion.vi*.

B Acknowledgement

I wish to thank Prof. Anton Zeilinger for offering me the privilege to work in his group and providing us with a scientific ambience which supports the "stimulated emission" of brilliant ideas.

Furthermore I wish to thank all my colleagues of the IQOQI, the Institute for Experimental Physics and the Vienna University of Technology. Special thanks go to my coworkers Thomas Jennewein, Rupert Ursin, Alessandro Fedrizzi, Thomas Scheidl, Robert Prevedl and Matteo Nespoli who essentially contributed to the successful realization of the 144km long-distance free-space experiment.

I also wish to thank my friends who never got tired of bringing me back down on "classical earth" after a long day of quantum physics. Hopefully this didn't take too much effort!

Last but not least I wish to thank my parents for supporting me throughout my studies and my brother who encouraged me to study physics.

Bibliography

[1] D. Bouwmeester, A. K. Ekert, and A. Zeilinger. *The Physics of Quantum Information: Quantum Cryptography, Quantum Teleportation, Quantum Computation*. Springer, 2001.

[2] H. Hübel, M. R. Vanner, T. Lederer, B. Blauensteiner, T. Lorünser, A. Poppe, and A. Zeilinger. High-fidelity transmission of polarization encoded qubits from an entangled source over 100 km of fiber. *Optics Express*, 15(12):7853–7862, 2007.

[3] H. Takesue, S. W. Nam, Q. Zhang, R. H. Hadfield, T. Honjo, K. Tamaki, and Y. Yamamoto. Quantum key distribution over a 40-dB channel loss using superconducting single-photon detectors. *Nature*, 1(6):343–348, 2007.

[4] L. M. Duan, M. D. Lukin, J. I. Cirac, and P. Zoller. Long-distance quantum communication with atomic ensembles and linear optics. *Nature*, 414:413–418, 2001.

[5] M. Aspelmeyer, T. Jennewein, M. Pfennigbauer, W. R. Leeb, and A. Zeilinger. Long-distance quantum communication with entangled photons using satellites. *Selected Topics in Quantum Electronics, IEEE Journal of*, 9(6):1541–1551, 2003.

[6] H. Horvath, L. A. Arboledas, F. J. Olmo, O. Jovanovic, M. Gangl, W. Kaller, C. Sanchez, H. Sauerzopf, and S. Seidl. Optical characteristics of the aerosol in Spain and Austria and its effect on radiative forcing. *J. Geophys. Res*, 107:4386, 2002.

[7] R. Kaltenbaek, M. Aspelmeyer, T. Jennewein, C. Brukner, A. Zeilinger, M. Pfennigbauer, and W. R. Leeb. Proof-of-concept experiments for quantum physics in space. *Proceedings of SPIE*, 5161:252–268, 2003.

[8] A. Valencia, M. V. Chekhova, A. Trifonov, and Y. Shih. Entangled Two-Photon Wave Packet in a Dispersive Medium. *Physical Review Letters*, 88(18):183601, 2002.

[9] G. Naletto, C. Barbieri, T. Occhipinti, F. Tamburini, S. Billotta, S. Cocuzza, and D. Dravins. Very fast photon counting photometers for astronomical applications: from QuantEYE to AquEYE. *Proceedings of SPIE*, 6583:65830B, 2007.

[10] J. G. Rarity, P. R. Tapster, P. M. Gorman, and P. Knight. Ground to satellite secure key exchange using quantum cryptography. *New Journal of Physics*, 4(1):82, 2002.

[11] J. E. Nordholt, R. J. Hughes, G. L. Morgan, C. G. Peterson, and C. C. Wipf. Present and future free-space quantum key distribution. *Proceedings of SPIE*, 4635:116, 2003.

[12] M. Pfennigbauer, M. Aspelmeyer, W. Leeb, G. Baister, T. Dreischer, T. Jennewein, G. Neckamm, J. Perdigues, H. Weinfurter, and A. Zeilinger. Satellite-based quantum communication terminal employing state-of-the-art technology. *Journal of Optical Networking*, 4(9):549–560, 2005.

[13] T. Schmitt-Manderbach, H. Weier, M. Fürst, R. Ursin, F. Tiefenbacher, T. Scheidl, J. Perdigues, Z. Sodnik, C. Kurtsiefer, J. G. Rarity, A. Zeilinger, and H. Weinfurter. Experimental Demonstration of Free-Space Decoy-State Quantum Key Distribution over 144 km. *Physical Review Letters*, 98(1):10504, 2007.

[14] R. Ursin, F. Tiefenbacher, T. Schmitt-Manderbach, H. Weier, T. Scheidl, M. Lindenthal, B. Blauensteiner, T. Jennewein, J. Perdigues, P. Trojek, et al. Entanglement-based quantum communication over 144 km. *Nature Physics*, 3:481–486, 2007.

[15] E. Schrödinger. Die gegenwärtige Situation in der Quantenmechanik (The Present Situation in Quantum Mechanics). *Naturwiessenschaften*, 23:807–812; 823–828; 844–849, 1935.

[16] A. Einstein, B. Podolsky, and N. Rosen. Can Quantum-Mechanical Description of Physical Reality Be Considered Complete? *Physical Review*, 47(10):777–780, 1935.

[17] C. Bennett, G. Brassard, A. Ekert, et al. Quantum cryptography. *Scientific American*, 267(4):50–57, 1992.

[18] N. Gisin, G. Ribordy, W. Tittel, and H. Zbinden. Quantum cryptography. *Reviews of Modern Physics*, 74(1):145–195, 2002.

[19] C. H. Bennett, G. Brassard, et al. Quantum cryptography: Public key distribution and coin tossing. *Proceedings of IEEE International Conference on Computers, Systems, and Signal Processing*, 175, 1984.

[20] W. K. Wootters and W. H. Zurek. A single quantum can not be cloned. *Nature*, 299(5886):802–803, 1982.

[21] W. Y. Hwang. Quantum Key Distribution with High Loss: Toward Global Secure Communication. *Physical Review Letters*, 91(5):57901, 2003.

[22] A. Poppe, A. Fedrizzi, R. Ursin, H. Böhm, T. Lörunser, O. Maurhardt, M. Peev, M. Suda, C. Kurtsiefer, H. Weinfurter, et al. Practical quantum key distribution with polarization entangled photons. *Optics Express*, 12(16):3865–3871, 2004.

[23] A. K. Ekert. Quantum cryptography based on Bell's theorem. *Physical Review Letters*, 67(6):661–663, 1991.

[24] J. F. Clauser, M. A. Horne, A. Shimony, and R. A. Holt. Proposed Experiment to Test Local Hidden-Variable Theories. *Physical Review Letters*, 23(15):880–884, 1969.

[25] J. S. Bell. On the Einstein Podolsky Rosen Paradox. *Physics*, 1(3):195, 1964. Published in Long Island City (NY) by Physics Publishing Co.

[26] T. Jennewein, C. Simon, G. Weihs, H. Weinfurter, and A. Zeilinger. Quantum Cryptography with Entangled Photons. *Physical Review Letters*, 84(20):4729–4732, 2000.

[27] E. P. Wigner. On Hidden Variables and Quantum Mechanical Probabilities. *American Journal of Physics*, 38(8):1005–1009, 1970.

[28] C. H. Bennett and S. J. Wiesner. Communication via one-and two-particle operators on Einstein-Podolsky-Rosen states. *Physical Review Letters*, 69(20):2881–2884, 1992.

[29] K. Mattle, H. Weinfurter, P. G. Kwiat, and A. Zeilinger. Dense Coding in Experimental Quantum Communication. *Physical Review Letters*, 76(25):4656–4659, 1996.

[30] C. H. Bennett, G. Brassard, C. Crépeau, R. Jozsa, A. Peres, and W. K. Wootters. Teleporting an unknown quantum state via dual classical and Einstein-Podolsky-Rosen channels. *Physical Review Letters*, 70(13):1895–1899, 1993.

[31] D. Bouwmeester, J. W. Pan, K. Mattle, M. Eibl, H. Weinfurter, and A. Zeilinger. Experimental quantum teleportation. *Nature(London)*, 390(6660):575–579, 1997.

[32] R. Ursin, T. Jennewein, M. Aspelmeyer, R. Kaltenbaek, M. Lindenthal, P. Walther, and A. Zeilinger. Quantum teleportation across the Danube. *Nature*, 430(7002):849, 2004.

[33] J. W. Pan, D. Bouwmeester, H. Weinfurter, and A. Zeilinger. Experimental Entanglement Swapping: Entangling Photons That Never Interacted. *Physical Review Letters*, 80(18):3891–3894, 1998.

[34] W. T. Buttler, R. J. Hughes, P. G. Kwiat, S. K. Lamoreaux, G. G. Luther, G. L. Morgan, J. E. Nordholt, C. Peterson, and C. M. Simmons. Practical Free-Space Quantum Key Distribution over 1 km. *Physical Review Letters*, 81(15):3283–3286, 1998.

[35] W. T. Buttler, R. J. Hughes, S. K. Lamoreaux, G. L. Morgan, J. E. Nordholt, and C. G. Peterson. Daylight Quantum Key Distribution over 1.6 km. *Physical Review Letters*, 84(24):5652–5655, 2000.

[36] J. G. Rarity, P. M. Gorman, P. R. Tapster, and M. Dera. Secure key exchange over 1.9 km free-space range using quantumcryptography. *Electronics Letters*, 37(8):512–514, 2001.

[37] J. G. Rarity, P. R. Tapster, and P. M. Gorman. Secure Free-space Key Exchange to 1.9 km and Beyond. *Journal of Modern Optics*, 48(13):1887–1901, 2001.

[38] R. J. Hughes, J. E. Nordholt, D. Derkacs, and C. G. Peterson. Practical free-space quantum key distribution over 10 km in daylight and at night. *New Journal of Physics*, 4(1):43, 2002.

[39] C. Kurtsiefer, P. Zarda, M. Halder, H. Weinfurter, P. Gorman, P. R. Tapster, and J. G. Rarity. A Step Towards Global Quantum Key Distribution. *Nature*, 419:450, 2002.

[40] M. Aspelmeyer, H. R. Bohm, T. Gyatso, T. Jennewein, R. Kaltenbaek, M. Lindenthal, G. Molina-Terriza, A. Poppe, K. Resch, M. Taraba, et al. Long-Distance Free-Space Distribution of Quantum Entanglement. *Science*, 301(5633):621, 2003.

[41] I. Marcikic, A. Lamas-Linares, and C. Kurtsiefer. Free-space quantum key distribution with entangled photons. *Applied Physics Letters*, 89:101122, 2006.

[42] K. Resch, M. Lindenthal, B. Blauensteiner, H. Böhm, A. Fedrizzi, C. Kurtsiefer, A. Poppe, T. Schmitt-Manderbach, M. Taraba, R. Ursin, et al. Distributing entanglement and single photons through an intra-city, free-space quantum channel. *Optics Express*, 13(1):202–209, 2005.

[43] C. Z. Peng, T. Yang, X. H. Bao, J. Zhang, X. M. Jin, F. Y. Feng, B. Yang, J. Yang, J. Yin, Q. Zhang, et al. Experimental Free-Space Distribution of Entangled Photon Pairs Over 13 km: Towards Satellite-Based Global Quantum Communication. *Physical Review Letters*, 94(15):150501, 2005.

[44] Optical Ground Station. URL `http://www.iac.es/telescopes/ogs/OGSE.html`.

[45] Nordic Optical Telescope. URL `http://www.not.iac.es/`.

[46] ESA Science & Technology. URL `http://sci.sa.int/science-e/www/object/index.cfm?fobjectid=36520`.

[47] C. E. Kuklewicz, M. Fiorentino, G. Messin, F. N. C. Wong, and J. H. Shapiro. High-flux source of polarization-entangled photons from a periodically poled $KTiOPO_4$ parametric down-converter. *Physical Review A*, 69(1):13807, 2004.

[48] M. H. Rubin, D. N. Klyshko, Y. H. Shih, and A. V. Sergienko. Theory of two-photon entanglement in type-II optical parametric down-conversion. *Physical Review A*, 50(6):5122–5133, 1994.

[49] P. G. Kwiat, K. Mattle, H. Weinfurter, A. Zeilinger, A. V. Sergienko, and Y. Shih. New High-Intensity Source of Polarization-Entangled Photon Pairs. *Physical Review Letters*, 75(24):4337–4341, 1995.

[50] T. Kim, M. Fiorentino, and F. N. C. Wong. Phase-stable source of polarization-entangled photons using a polarization Sagnac interferometer. *Physical Review A*, 73(1):12316, 2006.

[51] F. N. C. Wong, J. H. Shapiro, and T. Kim. Efficient generation of polarization-entangled photons in a nonlinear crystal. *Laser Physics*, 16:1517–1524, 2006.

[52] R. G. W. Brown, R. Jones, J. G. Rarity, and K. D. Ridley. Characterization of silicon avalanche photodiodes for photon correlation measurements. 2: Active quenching. *Applied Optics*, 26(12):2383–2389, 1987.

[53] S. Cova, M. Ghioni, A. Lacaita, C. Samori, and F. Zappa. Avalanche photodiodes and quenching circuits for single-photon detection. *Applied Optics*, 35(12), 1996.

[54] D. MacSween, R. J. McIntyre, C. Trottier, and P. P. Webb. Photon counting techniques with silicon avalanche photodiodes. *Applied Optics*, 32(21/20), 1993.

[55] G. Weihs. *Ein Experiment zum Test der Bellschen Ungleichung unter Einsteinscher Lokalität*. Ph.D. thesis, 1999.

[56] J. M. P. Armengol, B. Furch, C. J. de Matos, O. Minster, L. Cacciapuoti, M. Pfennigbauer, M. Aspelmeyer, T. Jennewein, R. Ursin, T. Schmitt-Manderbach, G. Baister, J. G. Rarity, W. Leeb, C. Barbieri, H. Weinfurter, and A. Zeilinger. Quantum Communications at ESA: Towards a Space Experiment on the ISS. *58th International Astronautical Congress, Hyderabad, India*, September 2007.